

Copyright

by

Amir Reza Rahmani

2009

**NUMERICAL SIMULATION OF WATER- AND OIL-BASE MUD-
FILTRATE INVASION IN VERTICAL WELLS AND
CORRESPONDING IMPACT ON MONOPOLE AND DIPOLE
SONIC WAVEFORMS**

by

AMIR REZA RAHMANI, B.Sc.

REPORT

Presented to the Faculty of the Graduate School of
The University of Texas at Austin
in Partial Fulfillment
of the Requirements
for the Degree of

MASTER OF SCIENCE IN ENGINEERING

The University of Texas at Austin

August 2009

**NUMERICAL SIMULATION OF WATER- AND OIL-BASE MUD-
FILTRATE INVASION IN VERTICAL WELLS AND
CORRESPONDING IMPACT ON MONOPOLE AND DIPOLE
SONIC WAVEFORMS**

**Approved by
Supervising Committee:**

Carlos Torres-Verdín, Supervisor

Kamy Sepehrnoori, Reader

Acknowledgements

I would like to thank my supervisor, Dr. Carlos Torres-Verdín, for his guidance during my research and study at The University of Texas at Austin. Without his patience, perpetual energy and enthusiasm in research, this work would have never happened. I would also like to thank my friend and colleague, Robert Mallan, for helping me to get through the difficult times, and for all the emotional and technical support he provided. I am extremely grateful to Dr. Jun Ma for providing me with sonic codes and his patience and support during my research. I am also thankful to Dr. Renzo Angeles for his valuable advice and friendship. His extensive and interesting discussions regarding my work have been very helpful for this study.

Finally, I would like to express my special thanks to The University of Texas at Austin's Research Consortium on Formation Evaluation, jointly sponsored by Aramco, Anadarko Petroleum Corporation, Baker-Hughes, BG, BHP Billiton, BP, Chevron, ConocoPhillips, ENI, ExxonMobil, Halliburton, Hess, Marathon, Mexican Institute for Petroleum, Nexen, Petrobras, RWE, Schlumberger, StatoilHydro, TOTAL, and Weatherford.

August 2009

Abstract

NUMERICAL SIMULATION OF WATER- AND OIL-BASE MUD-FILTRATE INVASION IN VERTICAL WELLS AND CORRESPONDING IMPACT ON MONOPOLE AND DIPOLE SONIC WAVEFORMS

Amir Reza Rahmani, M.S.E

The University of Texas at Austin, 2009

Supervisor: Carlos Torres-Verdín

The effect of mud-filtrate invasion on borehole sonic measurements plays an important role in the interpretation of acoustic logs. In this work, I quantify the effects of both water- and oil-base mud-filtrate invasion on monopole and dipole sonic waveforms. Past efforts have been made to study these effects, but the actual spatial distribution of fluid saturation due to mud-filtrate invasion has not been considered. Studying these effects will improve the interpretation of sonic logs.

First, I simulate both water- and oil-base mud-filtrate invasion using a commercial multi-phase fluid-flow simulator. I assume that the formation is initially saturated with water and gas, and exhibits a capillary transition zone. Simulation of mud-filtrate invasion

yields two-dimensional spatial distributions of fluid saturation. Fluid-saturation distributions are then transformed into spatial distributions of acoustic properties, namely rock density as well as compressional- and shear-wave velocities. Subsequently, I simulate the corresponding monopole and dipole sonic waveforms assuming axially symmetric variations of acoustic properties. The studies consider four rock types with different petrophysical properties, including porosity, permeability, capillary pressure and relative permeability. Measurements are simulated in a vertical well at two different measurement locations: at the first measurement location, the receiver array is located at the top of the capillary transition zone; at the second measurement location, half of the receivers are inside the water zone and half are outside the water zone at the bottom of the capillary transition zone. I assess acoustic propagation modes and their velocities with frequency dispersion analysis.

Simulations show that mud-filtrate invasion causes a decrease in the high-frequency asymptote of flexural-mode slowness in frequency dispersion results. Furthermore, the deeper invasion associated with water-base mud can cause an increase in the low-frequency asymptote of flexural-mode slowness in frequency dispersion results. Such an increase depends on the specific petrophysical properties of the rock under consideration. I also show that variations of rock petrophysical properties impact frequency dispersion results; different frequency components are affected in different manners. For instance, sonic measurements acquired in a tight-gas sand are almost insensitive to invasion for both water- and oil-base mud even though mud filtrate penetrates deeply into the formation.

Table of Contents

| | |
|---|-------------|
| Acknowledgments | iv |
| Abstract | v |
| Table of Contents | vii |
| List of Tables | viii |
| List of Figures | x |
| Chapter 1: Introduction..... | 1 |
| Chapter 2: Numerical Simulation of Mud-Filtrate Invasion | 4 |
| 2.1 Assumed Formation Model | 4 |
| 2.2 Simulation of Mud-Filtrate Invasion | 9 |
| Chapter 3: Modeling of Acoustic Properties | 19 |
| Chapter 4: Simulation Results..... | 33 |
| 4.1 Water-Base Mud-Filtrate Invasion | 36 |
| 4.2 Oil-Base Mud-Filtrate Invasion | 53 |
| Chapter 5: Conclusions | 72 |
| 5.1 Effect of Mud-Filtrate Invasion | 72 |
| 5.2 Effect of Petrophysical Properties | 74 |
| 5.3 Effect of Measurement Location | 75 |
| Nomenclature | 77 |
| Acronyms | 79 |
| References | 80 |
| Vita..... | 83 |

List of Tables

| | |
|---|----|
| Table 2.1: Summary of rock and fluid properties used to simulate the process of mud-filtrate invasion. | 6 |
| Table 2.2: Summary of assumed petrophysical properties for the cases of study. | 6 |
| Table 2.3: Summary of relative permeability and capillary pressure parameters used in Brooks-Corey equations for water-oil system. | 7 |
| Table 2.4: Summary of relative permeability and capillary pressure parameters used in Brooks-Corey equations for gas-liquid system. | 7 |
| Table 2.5: Summary of geometrical and numerical properties used for all cases of study. | 12 |
| Table 2.6: Summary of parameters assumed in the simulation of the process of mud-filtrate invasion. | 14 |
| Table 2.7: Summary of PVT properties of the assumed in-situ hydrocarbon and mud-filtrate components. | 15 |
| Table 2.8: Summary of mudcake parameters. | 15 |
| Table 2.9: Average mud-filtrate invasion rates for different rock types. | 16 |
| Table 3.1: Assumed values of bulk and shear moduli water, oil, gas and sandstone. | 23 |
| Table 3.2: Dry bulk and shear moduli of different rock types. | 24 |
| Table 5.1: Effect of WBM invasion on the flexural wave at two different frequencies. . | 72 |
| Table 5.2: Effect of OBM invasion on the flexural wave at two different frequencies. . | 72 |
| Table 5.3: Effect of WBM and OBM invasion on the Stoneley-wave dispersion for different rock types. | 73 |
| Table 5.4: Frequency range of the compressional-wave before invasion for different rock types. | 74 |

Table 5.5: Shifts of flexural-wave low-frequency asymptote for different rock types;
the effect of measurement location on the flexural wave..... 75

List of Figures

| | |
|--|----|
| Figure 2.1: Capillary pressure for the four rock types..... | 8 |
| Figure 2.2: Water-oil relative permeability curves for the four rock types. | 8 |
| Figure 2.3: Gas-liquid relative permeability curves for the four rock types..... | 9 |
| Figure 2.4: Vertical variation of water saturation assumed in the formation for different rock types..... | 10 |
| Figure 2.5: Front view of the finite-difference grids used to discretize the formation. The blue region identifies the water zone. | 11 |
| Figure 2.6: Top view of the finite-difference grids used to discretize the formation. | 12 |
| Figure 2.7: Water-base mud-filtrate invasion rates for different rock types vs. time. | 16 |
| Figure 2.8: Radial distribution of water saturation describing radii of water-base mud-filtrate invasion for different rock types. The rock with the lowest permeability and porosity has the largest radius of invasion and the smoothest transition from invaded to uninvaded zones. The rock with the highest permeability and porosity exhibits the smallest radius of invasion and the sharpest transition from invaded to uninvaded zones. | 17 |
| Figure 2.9: Radial profile of oil saturation describing radii of oil-base mud-filtrate invasion for different rock types. The rock with the lowest permeability and porosity has the largest radius of invasion and the smoothest transition from invaded to uninvaded zones. The rock with the highest permeability and porosity exhibits the smallest radius of invasion and the sharpest transition from invaded to uninvaded zones. | 18 |

| | |
|---|----|
| Figure 3.1: Fluid substitution sensitivity analysis for the assumed rock types. Solid lines identify compressional-wave velocities and dashed lines identify shear-wave velocities..... | 23 |
| Figure 3.2: Spatial distribution of acoustic properties for the first rock type after water-base mud-filtrate (WBM) invasion. Left panel: spatial distribution of density. Central panel: spatial distribution of P-wave slowness. Right panel: spatial distribution of S-wave slowness. | 25 |
| Figure 3.3: Spatial distribution of acoustic properties for the second rock type after water-base mud-filtrate (WBM) invasion. Left panel: spatial distribution of density. Central panel: spatial distribution of P-wave slowness. Right panel: spatial distribution of S-wave slowness. | 26 |
| Figure 3.4: Spatial distribution of acoustic properties for the third rock type after water-base mud-filtrate (WBM) invasion. Left panel: spatial distribution of density. Central panel: spatial distribution of P-wave slowness. Right panel: spatial distribution of S-wave slowness. | 27 |
| Figure 3.5: Spatial distribution of acoustic properties for the fourth rock type after water-base mud-filtrate (WBM) invasion. Left panel: spatial distribution of density. Central panel: spatial distribution of P-wave slowness. Right panel: spatial distribution of S-wave slowness. | 28 |
| Figure 3.6: Spatial distribution of acoustic properties for the first rock type after oil-base mud-filtrate (OBM) invasion. Left panel: spatial distribution of density. Central panel: spatial distribution of P-wave velocity. Right panel: spatial distribution of S-wave velocity..... | 29 |

| | |
|---|----|
| Figure 3.7: Spatial distribution of acoustic properties for the second rock type after oil-base mud-filtrate (OBM) invasion. Left panel: spatial distribution of density. Central panel: spatial distribution of P-wave velocity. Right panel: spatial distribution of S-wave velocity..... | 30 |
| Figure 3.8: Spatial distribution of acoustic properties for the third rock type after oil-base mud-filtrate (OBM) invasion. Left panel: spatial distribution of density. Central panel: spatial distribution of P-wave velocity. Right panel: spatial distribution of S-wave velocity..... | 31 |
| Figure 3.9: Spatial distribution of acoustic properties for the fourth rock type after oil-base mud-filtrate (OBM) invasion. Left panel: spatial distribution of density. Central panel: spatial distribution of P-wave velocity. Right panel: spatial distribution of S-wave velocity..... | 32 |
| Figure 4.1: Schematic of the wireline sonic tool assumed in the numerical simulations. | 34 |
| Figure 4.2: Location of the receiver array for each measurement point. | 35 |
| Figure 4.3: Frequency dispersion results for the first rock type with a dipole source at the first measurement location. Red and black curves identify results for after and before WBM invasion, respectively. Black and red lines identify the formation shear slowness before and after invasion, respectively. | 37 |
| Figure 4.4: Frequency dispersion results for the first rock type with a monopole source at the first measurement location. Red and black curves identify results for after and before WBM invasion, respectively. Stoneley and pseudo-Rayleigh modes are circled separately. Solid black and red lines identify the formation shear slowness before and after invasion, respectively. Dashed black and red lines identify the formation compressional slowness before and after invasion, respectively. | 38 |

- Figure 4.5:** Frequency dispersion results for the first rock type with a dipole source at the second measurement location. Red and black curves identify results for after and before WBM invasion, respectively. Black and red lines identify the formation shear slowness before and after invasion, respectively. 39
- Figure 4.6:** Frequency dispersion results for the first rock type with a monopole source at the second measurement location. Red and black curves identify results for after and before WBM invasion, respectively. Stoneley and pseudo-Rayleigh modes are circled separately. The solid line identifies the formation shear slowness at the top receiver. Dashed black and red lines identify the formation compressional slowness before and after invasion at the top receiver, respectively. 40
- Figure 4.7:** Frequency dispersion results for the second rock type with a dipole source at the first measurement location. Red and black curves identify results for after and before WBM invasion, respectively. Black and red lines identify the formation shear slowness before and after invasion, respectively. 41
- Figure 4.8:** Frequency dispersion results for the second rock type with a monopole source at the first measurement location. Red and black curves identify results for after and before WBM invasion, respectively. Stoneley, compressional and pseudo-Rayleigh modes are circled separately. The dashed black line represents uninvaded formation shear-wave slowness. Solid black and red lines identify the formation compressional-wave slowness before and after invasion, respectively. 42

- Figure 4.9:** Frequency dispersion results for the second rock type with a dipole source at the second measurement location. Red and black curves identify results for after and before WBM invasion, respectively. Solid black and red lines identify the formation shear-wave slowness before and after invasion, respectively. 43
- Figure 4.10:** Frequency dispersion results for the second rock type with a monopole source at the second measurement location. Red and black curves identify results for after and before WBM invasion, respectively. Black and red lines identify the formation compressional-wave slowness before and after invasion at the location of the top receiver, respectively. The blue line identifies the water-filled rock compressional slowness. 44
- Figure 4.11:** Frequency dispersion results for the third rock type with a dipole source at the first measurement location. Red and black curves identify results for after and before WBM invasion, respectively. Black and red lines identify the formation shear slowness before and after invasion, respectively. 45
- Figure 4.12:** Frequency dispersion results for the third rock type with a monopole source at the first measurement location. Red and black curves identify results for after and before WBM invasion, respectively. Stoneley and compressional modes are circled separately. Black and red lines identify the formation compressional-wave slowness before and after invasion, respectively. ... 46
- Figure 4.13:** Frequency dispersion results for the third rock type with a dipole source at the second measurement location. Red and black curves identify results for after and before WBM invasion, respectively. Black and red lines identify the formation shear slowness at the top receiver before and after invasion, respectively. 47

- Figure 4.14:** Frequency dispersion results for the third rock type with a monopole source at the second measurement location. Red and black curves identify results for after and before WBM invasion, respectively. Stoneley and compressional modes are circled separately. Black and red lines identify the formation compressional-wave slowness before and after invasion at the location of the top receiver, respectively. The blue line identifies the water-filled rock compressional slowness. 48
- Figure 4.15:** Frequency dispersion results for the fourth rock type with a dipole source at the first measurement location. Red and black curves identify results for after and before WBM invasion, respectively. Black and red lines identify formation shear slowness before and after invasion, respectively. 49
- Figure 4.16:** Frequency dispersion results for the fourth rock type with a monopole source at the first measurement location. Red and black curves identify results for after and before WBM invasion, respectively. Black and red lines identify the formation compressional-wave slowness before and after invasion, respectively. 50
- Figure 4.17:** Frequency dispersion results for the fourth rock type with a dipole source at the second measurement location. Red and black curves identify results for after and before WBM invasion, respectively. Compressional-wave after WBM invasion is circled in black. The blue line identifies the water-filled rock compressional slowness. Black and red lines identify the formation shear slowness at the top receiver before and after invasion, respectively. 52

- Figure 4.18:** Frequency dispersion results for the fourth rock type with a monopole source at the second measurement location. Red and black curves identify results for after and before WBM invasion, respectively. Stoneley and compressional modes are circled separately. Black and red lines identify the formation compressional-wave slowness before and after invasion at the location of the top receiver, respectively. The blue line identifies the water-filled rock compressional slowness. 53
- Figure 4.19:** Frequency dispersion results for the first rock type with a dipole source at the first measurement location. Black, red, and green curves identify results for before invasion, after WBM invasion, and after OBM invasion, respectively. Black, red, and green lines identify the formation shear slowness before invasion, after WBM invasion, and after OBM invasion, respectively. 54
- Figure 4.20:** Frequency dispersion results for the second rock type with a dipole source at the first measurement location. Black, red, and green curves identify results for before invasion, after WBM invasion, and after OBM invasion, respectively. Black, red, and green lines identify the formation shear slowness before invasion, after WBM invasion, and after OBM invasion, respectively. 55
- Figure 4.21:** Frequency dispersion results for the third rock type with a dipole source at the first measurement location. Black, red, and green curves identify results for before invasion, after WBM invasion, and after OBM invasion, respectively. Black, red, and green lines identify the formation shear slowness before invasion, after WBM invasion, and after OBM invasion, respectively. 56

- Figure 4.22:** Frequency dispersion results for the fourth rock type with a dipole source at the first measurement location. Black, red, and green curves identify results for before invasion, after WBM invasion, and after OBM invasion, respectively. Black, red, and green lines identify the formation shear slowness before invasion, after WBM invasion, and after OBM invasion, respectively. 57
- Figure 4.23:** Frequency dispersion results for the first rock type with a monopole source at the first measurement location. Green, red, and black curves identify results for after OBM invasion, after WBM invasion, and before invasion, respectively. Stoneley, compressional, and pseudo-Rayleigh modes are circled separately. The green, red, and black dashed lines represent compressional-wave slowness after OBM invasion, after WBM invasion, and before invasion, respectively. Solid green, red, and black lines identify the formation shear-wave slowness after OBM invasion, after WBM invasion, and before invasion, respectively. 59
- Figure 4.24:** Frequency dispersion results for the second rock type with a monopole source at the first measurement location. Green, red, and black curves identify results for after OBM invasion, after WBM invasion, and before invasion, respectively. Stoneley, compressional, and pseudo-Rayleigh modes are circled separately. The green, red, and black dashed lines represent compressional-wave slowness after OBM invasion, after WBM invasion, and before invasion, respectively. Solid green and black lines identify the formation shear-wave slowness after OBM invasion and before invasion, respectively. 60

- Figure 4.25:** Frequency dispersion results for the third rock type with a monopole source at the first measurement location. Green, red, and black curves identify results for after OBM invasion, after WBM invasion, and before invasion, respectively. Stoneley and compressional modes are circled separately. Solid green, red, and black lines identify the formation compressional-wave slowness after OBM invasion, after WBM invasion, and before invasion, respectively. 61
- Figure 4.26:** Frequency dispersion results for the fourth rock type with a monopole source at the first measurement location. Green, red, and black curves identify results for after OBM invasion, after WBM invasion, and before invasion, respectively. Stoneley and compressional modes are circled separately. Solid green, red, and black lines identify the formation compressional-wave slowness after OBM invasion, after WBM invasion, and before invasion, respectively. 62
- Figure 4.27:** Frequency dispersion results for the first rock type with a dipole source at the second measurement location. Black, red, and green curves identify results for before invasion, after WBM invasion, and after OBM invasion, respectively. Black, red, and green lines identify the formation shear slowness at the location of the top receiver before invasion, after WBM invasion, and after OBM invasion, respectively. 63

- Figure 4.28:** Frequency dispersion results for the second rock type with a dipole source at the second measurement location. Black, red, and green curves identify results for before invasion, after WBM invasion, and after OBM invasion, respectively. Black, red, and green lines identify the formation shear slowness at the location of the top receiver before invasion, after WBM invasion, and after OBM invasion, respectively. 64
- Figure 4.29:** Frequency dispersion results for the third rock type with a dipole source at the second measurement location. Black, red, and green curves identify results for before invasion, after WBM invasion, and after OBM invasion, respectively. Black, red, and green lines identify the formation shear slowness at the location of the top receiver before invasion, after WBM, invasion and after OBM invasion, respectively. 65
- Figure 4.30:** Frequency dispersion results for the fourth rock type with a dipole source at the second measurement location. Black, red, and green curves identify results for before invasion, after WBM invasion, and after OBM invasion, respectively. Flexural, leaky-P, and compressional modes are circled separately. Dashed green, red, and black lines represent formation shear slowness at the location of the top receiver after OBM invasion, after OBM invasion and before invasion, respectively. Solid red and green lines identify the formation compressional slowness at the location of the top receiver after WBM invasion and after OBM invasion, respectively. 66

Figure 4.31: Frequency dispersion results for the first rock type with a monopole source at the second measurement location. Green, red, and black curves identify results for after OBM invasion, after WBM invasion, and before invasion, respectively. Stoneley and pseudo-Rayleigh modes are circled separately. Solid green, red, and black lines identify the formation shear-wave slowness after OBM invasion, after WBM invasion, and before invasion, respectively. 68

Figure 4.32: Frequency dispersion results for the second rock type with a monopole source at the second measurement location. Green, red, and black curves identify results for after OBM invasion, after WBM invasion, and before invasion, respectively. Stoneley and compressional modes are circled separately. Solid green, red, and black lines identify the formation compressional-wave slowness after OBM invasion, after WBM invasion, and before invasion, respectively. The blue line identifies the compressional slowness of the water zone. 69

Figure 4.33: Frequency dispersion results for the third rock type with a monopole source at the second measurement location. Green, red, and black curves identify results for after OBM invasion, after WBM invasion, and before invasion, respectively. Stoneley and compressional modes are circled separately. Solid green, red, and black lines identify the formation compressional-wave slowness after OBM invasion, after WBM invasion, and before invasion, respectively. The blue line identifies the compressional slowness of the water zone. 70

Figure 4.34: Frequency dispersion results for the fourth rock type with a monopole source at the second measurement location. Green, red, and black curves identify results for after OBM invasion, after WBM invasion, and before invasion, respectively. Stoneley and compressional modes are circled separately. Solid green, red, and black lines identify the formation compressional-wave slowness after OBM invasion, after WBM invasion, and before invasion, respectively. The blue line identifies the compressional slowness of the water zone. 71

CHAPTER 1

INTRODUCTION

The objective of this work is to study the effects of mud-filtrate invasion, of variations of petrophysical properties of rock formations, and of measurement location on acoustic measurements acquired with borehole sonic tools. Petrophysical properties include porosity, permeability, capillary pressure, and relative permeability. Measurement locations include acquisition at the top and bottom of a capillary transition zone, where half of the receivers are inside and half are outside the water zone. By comparing the two measurement locations, I study the effect of vertical variation of fluid saturation on acoustic measurements. In addition, both water-base mud (WBM) and oil-base mud (OBM) invasion are considered and compared in this study.

Sonic measurements are an important part of well-log interpretation. Over the years, sonic measurements have evolved from their originally simple design to current multi-purpose applications. Initially, acoustic measurements were used to match seismic signals to rock layers. Nowadays, one can infer several reservoir and elastic properties with sonic measurements. Some of these properties include primary and secondary porosity, permeability, lithology, mineralogy, pore pressure, invasion, anisotropy, fluid type, stress magnitude and direction, presence and alignment of fractures, and quality of casing-cement bonds.

Chi and Torres-Verdín (2004) studied the effects of mud-filtrate invasion on borehole acoustic logs. They simulated realistic profiles of fluid saturation due to

invasion. However, they assumed a one-dimensional radial model and did not consider vertical variations of fluid saturation. Furthermore, they used an industry standard STC (slowness-time-coherence) method (Kimball and Mazetta 1984) to determine compressional- and shear-wave velocities of array sonic measurements.

Peyret and Torres-Verdín (2006) investigated the effect of water-base mud invading oil-bearing formations on borehole sonic measurements. They assessed their results via slowness-time-coherence processing of the simulated waveforms. They also assumed piston-like displacement of formation fluids and did not consider the actual distribution of fluids due to invasion.

The distance between the transmitter and the first receiver limits the radial resolution of the sonic tool. Measurements respond to average properties of the formation. Therefore, all sonic measurements are affected by mud-filtrate invasion. Accurate velocity distribution at well locations is necessary if one intends to use seismic amplitude data for reservoir characterization. Therefore, inaccuracy in velocity distribution brings about inaccuracy in reservoir elastic and petrophysical properties. In addition, the length of the receiver array restricts the vertical resolution. Consequently, measurement location can affect acoustic logs.

In acoustic logging, some of the waves are dispersive; meaning that their velocity (or slowness) varies with frequency. For these waves, the shape of the pulse does not remain constant across the receiver array. Hence, I do not use standard methods for estimating slowness, such as STC processing, that rely on wave-shape similarity. Instead, I use frequency dispersion analysis to study the modes of propagation in the frequency domain for the simulations reported in this report.

The report is organized as follows: I first describe how I generate synthetic models and different rock types. Rock types exhibit different porosities, permeabilities, capillary pressures, and relative permeabilities. Subsequently, I explain how I model mud-filtrate invasion into the formation. After these descriptions, I use fluid-substitution equations to transform fluid-saturation distributions to acoustic properties distributions. I input the calculated acoustic properties into the sonic simulator, from which I obtain sonic waveforms. Finally, after assessing the sonic measurements using frequency dispersion analysis, I discuss and analyze simulation results in terms of their implications to the interpretation of field measurements.

CHAPTER 2

NUMERICAL SIMULATION OF MUD-FILTRATE INVASION

2.1 ASSUMED FORMATION MODEL

I assume a formation that exhibits a capillary transition zone and is initially saturated with water and gas, namely CH_4 . The formation is 50 ft thick (from the depth of 9150 ft to the depth of 9200 ft) and does not contain shale. The gas-water contact is at the depth of 9195 ft. I assume four different rock types to investigate the effects of variations of petrophysical properties on the sonic response, namely porosity, permeability, capillary pressure and relative permeability. Capillary pressure and relative permeability curves are obtained using Brooks-Corey equations (1964),

$$P_c = P_c^o \sqrt{\frac{\phi}{K}} (1 - S_N)^{e_p}, \quad (2.1)$$

where P_c is capillary pressure (in psi), P_c^o is the coefficient for capillary pressure (in psi.darcy^{1/2}), e_p is the pore-size distribution exponent, ϕ is porosity (in fraction), K is permeability (in darcy), and S_N is normalized wetting phase saturation, given by

$$S_N = \frac{S_w - S_{wr}}{1 - S_{wr} - S_{nwr}}, \quad (2.2)$$

where S_{wr} and S_{nwr} are residual wetting and non-wetting phase saturations, respectively.

Water-oil and gas-liquid relative permeabilities are estimated using Brooks-Corey equations,

$$k_{rw} = k_{rw}^o S_N^{e_w}, \quad (2.3)$$

and

$$k_{mww} = k_{mww}^o (1 - S_N)^{e_{mw}}, \quad (2.4)$$

where k_{rw} and k_{mww} are wetting and non-wetting phase relative permeabilities, k_{rw}^o and k_{mww}^o are relative permeability end points, and e_w and e_{mw} are empirical exponents for each fluid phase. The same correlations hold true for a gas-liquid system.

Furthermore, irreducible water saturation for each rock type is calculated using Coates correlation (1981):

$$K^{1/2} = 100 \times \phi^2 \frac{1 - S_{w,irr}}{S_{w,irr}}. \quad (2.5)$$

Solving for $S_{w,irr}$, we obtain

$$S_{w,irr} = \frac{1}{1 + \frac{K^{1/2}}{100 \times \phi^2}}, \quad (2.6)$$

where K is permeability (in md), ϕ is porosity (in fraction), and $S_{w,irr}$ is the irreducible water saturation (in fraction).

Table 2.1 is a summary of rock and fluid properties. Table 2.2 is a summary of assumed petrophysical properties for the cases of study. Tables 2.3 and 2.4 list parameters used in Brooks-Corey equations for each rock type for water-oil and gas-liquid systems, respectively. These parameters, together with residual hydrocarbon

saturations, are chosen based on the fact that low-porosity formations are often associated with variable pore-size distributions, thereby resulting in smooth variations of capillary pressure with water saturation. The poor sorting of grains in low-porosity rocks tends to decrease the relative permeability and increase the residual fluid saturations. By contrast, high-porosity formations tend to exhibit uniform pore-size distributions with large individual pore sizes and throats, in which case the capillary pressure curve will exhibit an “L” shape behavior, as depicted by Figures 2.1 through 2.3. These figures show capillary pressure, and water-oil and oil-gas relative permeability curves for the various rock types considered in this report.

Table 2.1: Summary of assumed rock and fluid properties used to simulate the process of mud-filtrate invasion.

| Variable | Value (kg/m³) |
|-----------------|---------------------------------|
| Matrix density | 2650 |
| Water density | 1000 |
| Oil density | 650 |
| Gas density | 16.83 |

Table 2.2: Summary of assumed petrophysical properties for the cases of study.

| | Rock 1 | Rock 2 | Rock 3 | Rock 4 |
|--|---------------|---------------|---------------|---------------|
| Effective porosity (fraction) | 0.1 | 0.15 | 0.2 | 0.25 |
| Permeability (md) | 1.5 | 15 | 100 | 500 |
| Residual hydrocarbon (oil and gas) saturation (fraction) | 0.3 | 0.25 | 0.2 | 0.15 |
| Irreducible water saturation (fraction) | 0.45 | 0.36 | 0.28 | 0.21 |

It should be noted that the last row in Table 2.2 is calculated using Coates correlation (Equation 2.5) based on the assumed porosities and permeabilities.

Table 2.3: Summary of relative permeability and capillary pressure parameters used in Brooks-Corey equations for the water-oil system.

| | Rock 1 | Rock 2 | Rock 3 | Rock 4 |
|-------------|---------------|---------------|---------------|---------------|
| P_c^o | 110 | 220 | 400 | 650 |
| e_p | 1.75 | 7 | 15 | 80 |
| k_{rw}^o | 0.15 | 0.25 | 0.45 | 0.65 |
| e_w | 3 | 2.5 | 3 | 3 |
| k_{mwo}^o | 0.2 | 0.4 | 0.7 | 0.87 |
| e_{nw} | 3 | 2 | 2.2 | 1.8 |

Table 2.4: Summary of relative permeability and capillary pressure parameters used in Brooks-Corey equations for the gas-liquid system.

| | Rock 1 | Rock 2 | Rock 3 | Rock 4 |
|-------------|---------------|---------------|---------------|---------------|
| k_{rw}^o | 0.2 | 0.4 | 0.7 | 0.85 |
| e_w | 6 | 3 | 3 | 1.7 |
| k_{mwo}^o | 0.32 | 0.6 | 0.8 | 0.95 |
| e_{nw} | 4.5 | 2 | 1.5 | 1.2 |

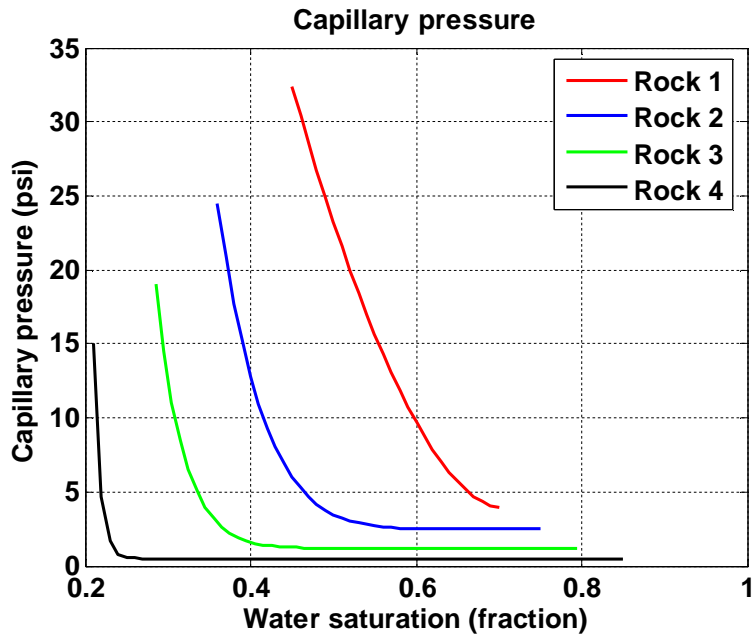


Figure 2.1: Capillary pressure for the four assumed rock types.

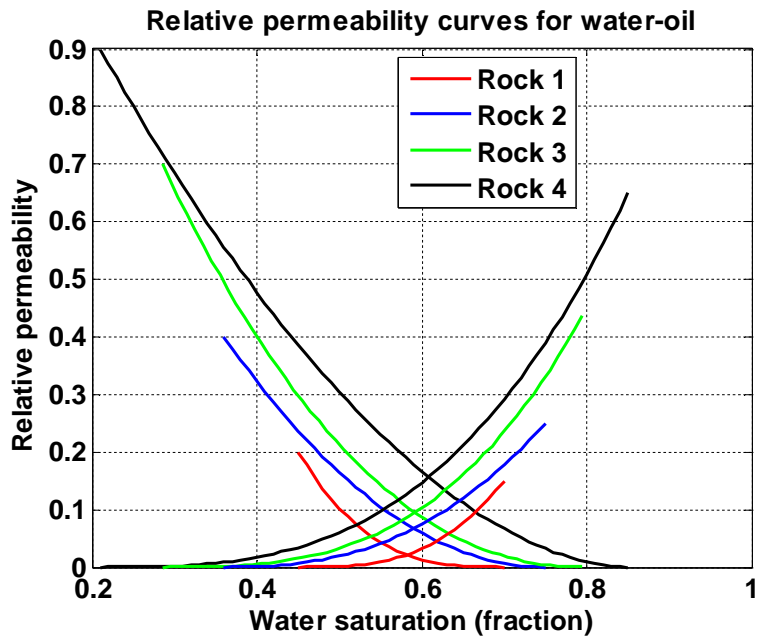


Figure 2.2: Water-oil relative permeability curves for the four assumed rock types.

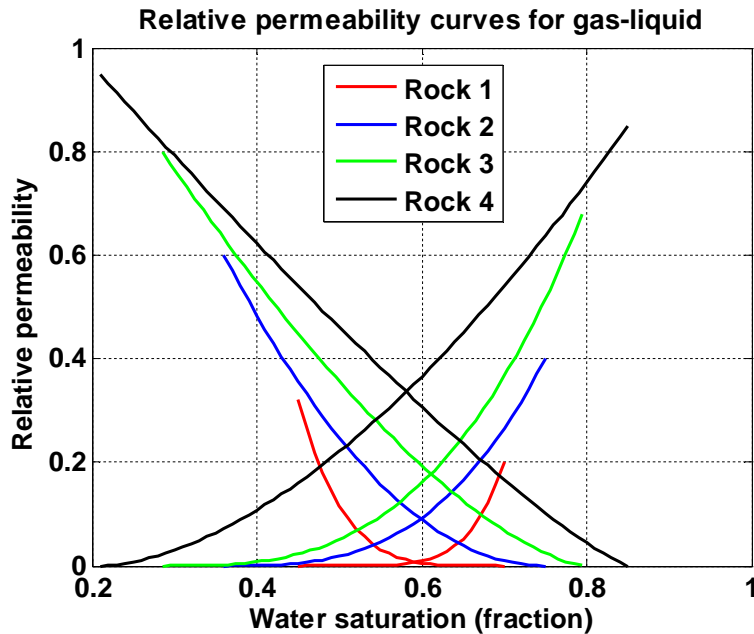


Figure 2.3: Gas-liquid relative permeability curves for the four assumed rock types.

2.2 SIMULATION OF MUD-FILTRATE INVASION

Mud-filtrate invasion modeling has been discussed extensively in past studies for vertical, deviated, and horizontal wells. Some researchers have used a commercial black-oil multi-phase fluid-flow simulator (ECLIPSE) for modeling invasion (Alpak et al., 2003). Others have adopted a numerical approach with an existing 3D multi-phase fluid-flow simulator (UTCHEM) to model mud-filtrate invasion (Wu et al., 2004). All of them use Cartesian grids and consequently, the proposed models assume a rough borehole. In this study, I use the Computer Modeling Group (CMG) simulator to model mud-filtrate invasion using cylindrical grids.

Figure 2.4 shows vertical variations of water saturation in the formation for the four assumed rock types. According to this figure, capillary pressure changes smoothly

for the first rock type (which exhibits the lowest porosity and permeability), whereas rock type 4, with the highest porosity and permeability, exhibits a sharp change in capillary pressure in the transition from the partially gas-saturated zone to the water zone. Figure 2.5 shows the finite-difference grids used to simulate mud-filtrate invasion for all assumed rock types. Figure 2.6 shows the top view of the wellbore in the formation. The finite-difference grid design is the same in all cases of study. Table 2.5 is a summary of geometrical and numerical properties used in the simulation of mud-filtrate invasion.

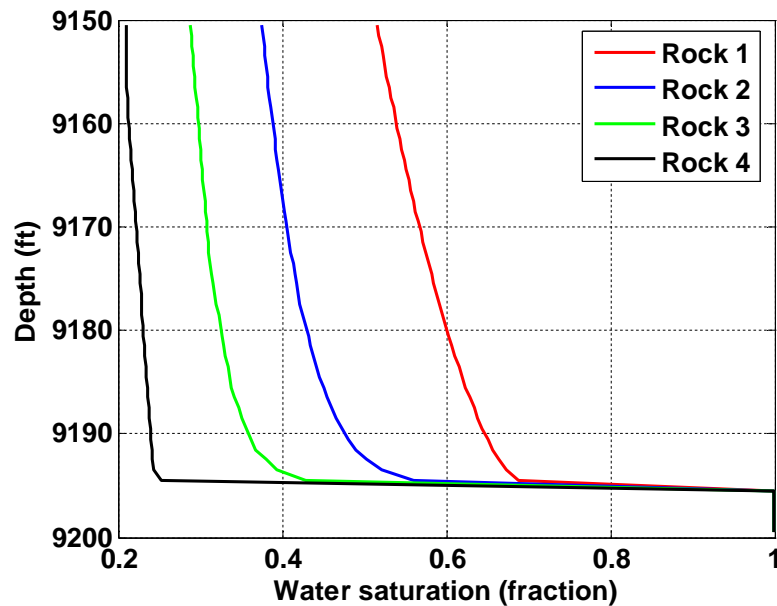


Figure 2.4: Vertical variation of water saturation assumed in the formation for the four assumed rock types.

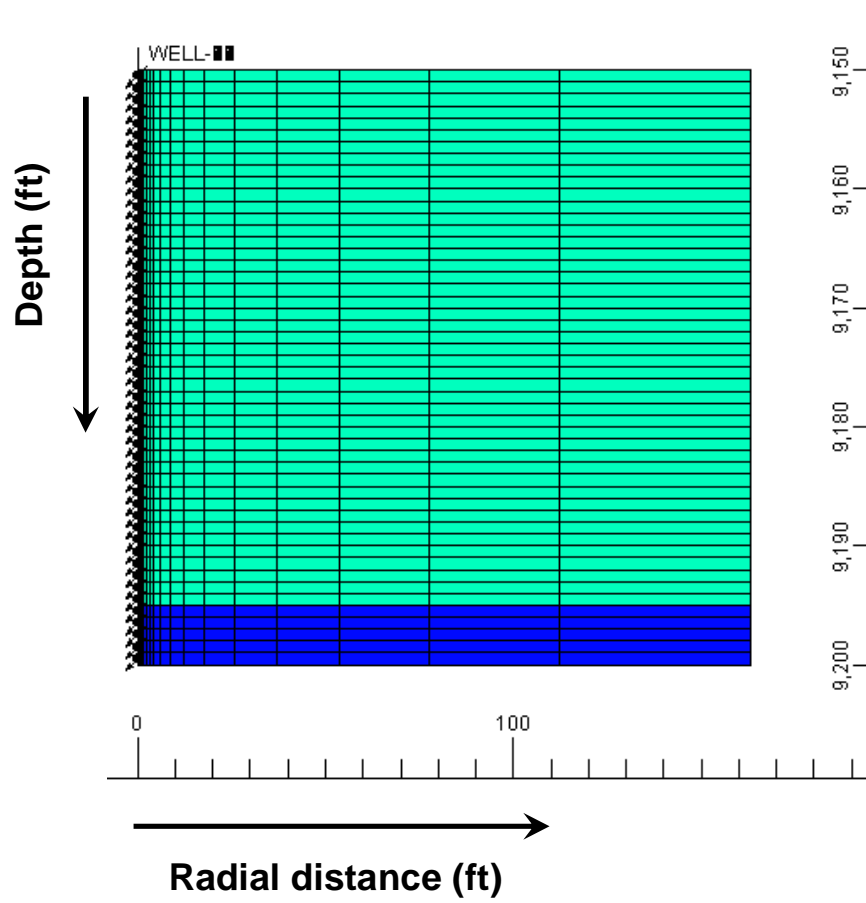


Figure 2.5: Front view of the finite-difference grids used to discretize the formation. The blue region identifies the water zone.

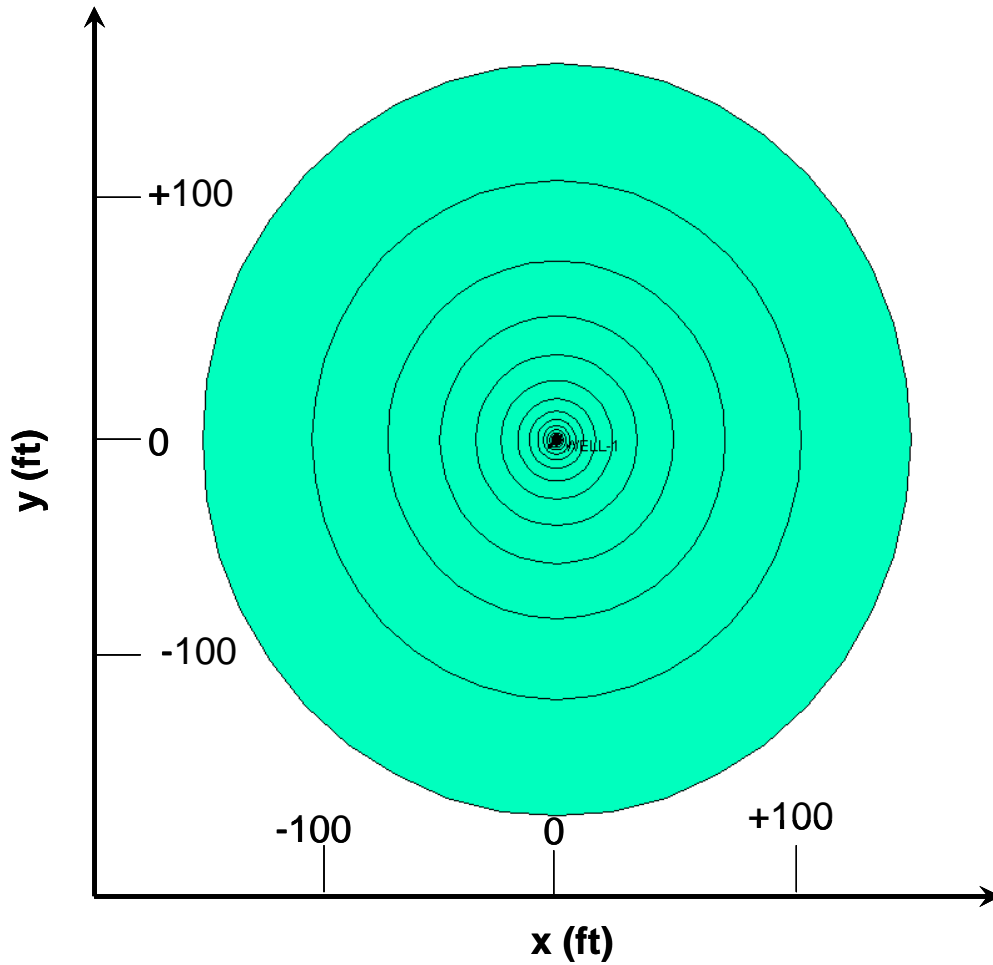


Figure 2.6: Top view of the finite-difference grids used to discretize the formation.

Table 2.5: Summary of geometrical and numerical properties assumed for all cases of study.

| Variable | Unit | Value |
|-----------------------------------|------|----------|
| Wellbore radius | ft | 0.354 |
| External radius | ft | 160 |
| Reservoir thickness | ft | 50 |
| Number of nodes (r -direction) | -- | 32 |
| Number of nodes (z -direction) | -- | 50 |
| Grid cell size (r -direction) | ft | variable |
| Grid cell size (z -direction) | ft | 1 |

In order to calculate the rate of mud-filtrate invasion, I use a 1D radial, isothermal, equation-of-state (EOS) compositional simulator developed by the Formation Evaluation Group of The University of Texas at Austin (Abdollah Pour, 2008). It simulates simultaneous flow of three fluid phases (water, oil, and gas) and is based on Peng-Robinson's equation of state. Simulations are based on the implicit pressure-explicit-concentration (IMPEC) method to solve the partial differential equations arising from the discretization of fluid-flow equations. This simulator implements a mudcake model that allows one to thicken the mudcake and to change the permeability and porosity of the mudcake with time. The mudcake model is coupled with the assumed formation model. Equations 2.7, 2.8 and 2.9 govern the process of mud-filtrate invasion. Chenevert et al. (2001) performed laboratory experiments to investigate water-base mud-filtrate invasion and mudcake buildup. They suggested that the relationship between mudcake permeability and mudcake pressure differential be related by the following equation:

$$k_{mc}(t) = \frac{k_{mc0}}{P_{mc}^v(t)}, \quad (2.7)$$

where k_{mc0} is mudcake reference permeability, P_{mc} is mudcake pressure differential, and v is a compressibility exponent varying between 0.4 and 0.9.

Similarly, Chenevert et al. (2001) suggested that the relationship between mudcake porosity and mudcake pressure differential be given by:

$$\phi_{mc}(t) = \frac{\phi_{mc0}}{P_{mc}^{v.\delta}(t)}, \quad (2.8)$$

where ϕ_{mc0} is mudcake reference porosity and δ is a multiplier for the compressibility exponent varying between 0.1 and 0.2.

The equation for the time evolution of mudcake thickness was proposed by Chin (1995):

$$r_{mc} \cdot dr_{mc} = \frac{f_s}{(1-f_s)[1-\phi_{mc}(t)]} \times \frac{k_{mc} P_{mc} dt}{\mu_f}, \quad (2.9)$$

where f_s is mud solid fraction, r_{mc} is mudcake thickness, dr_{mc} is differential mudcake thickness, dt is differential time, and μ_f is mud-filtrate viscosity. This equation assumes that solid particles do not enter the formation.

Table 2.6 summarizes the parameters assumed in the simulation of mud-filtrate invasion. Table 2.7 lists PVT properties of the assumed in-situ and mud-filtrate components. Table 2.8 summarizes the assumed mudcake parameters. It should be mentioned that oil-base mud is assumed to consist of MC₁₆ entirely.

Table 2.6: Summary of parameters assumed in the simulation of mud-filtrate invasion.

| Variable | Unit | Value |
|--------------------------------------|------|-------|
| Initial formation pressure @ 9150 ft | psi | 4000 |
| Maximum invasion time | day | 1 |
| Temperature @ 9150 ft | °F | 188 |

Figure 2.7 shows the time-varying rates of water-base mud-filtrate invasion into the formation for the assumed rock types. The time-averaged values of these rates are input into the fluid-flow simulator (CMG) and are listed in Table 2.9.

Table 2.7: Summary of PVT properties of the assumed in-situ hydrocarbon and mud-filtrate components.

| Property | Units | CH ₄ | MC ₁₆ |
|----------------------|-------------------|-----------------|------------------|
| Critical temperature | °F | -125.7 | 822.5 |
| Critical pressure | psi | 653.3 | 240.2 |
| Mass density | kg/m ³ | 16.83 | 732.4 |
| Molar weight | kg/kg.mol | 16.6 | 222 |
| Viscosity | cp | 0.025 | 1.5 |
| Acentric factor | none | 0.008 | 0.71 |

Table 2.8: Summary of assumed mudcake parameters.

| Variable | Units | Value |
|----------------------------------|----------|-------|
| Mudcake reference permeability | md | 0.03 |
| Mudcake reference porosity | fraction | 0.3 |
| Mud solid fraction | fraction | 0.06 |
| Mudcake maximum thickness | in | 0.4 |
| Mudcake compressibility exponent | fraction | 0.3 |
| Mudcake exponent multiplier | fraction | 0.1 |
| Mud hydrostatic pressure | psi | 4400 |

Figure 2.8 shows radii of water-base mud-filtrate invasion for the assumed rock types. According to this figure, the radius of invasion for the first rock type is longer than the other rock types. As porosity and permeability increase and pore-size distribution becomes more uniform, the radius of invasion decreases and the radial distribution of water saturation exhibits a more piston-like (shock front) behavior. Figure 2.9 shows the radius of oil-base mud-filtrate invasion for different rock types, and I observe the same trend as in Figure 2.8. With porosity and permeability increasing and the quality of rock improving, the radius of invasion decreases and the saturation front becomes similar to that of a shock front.

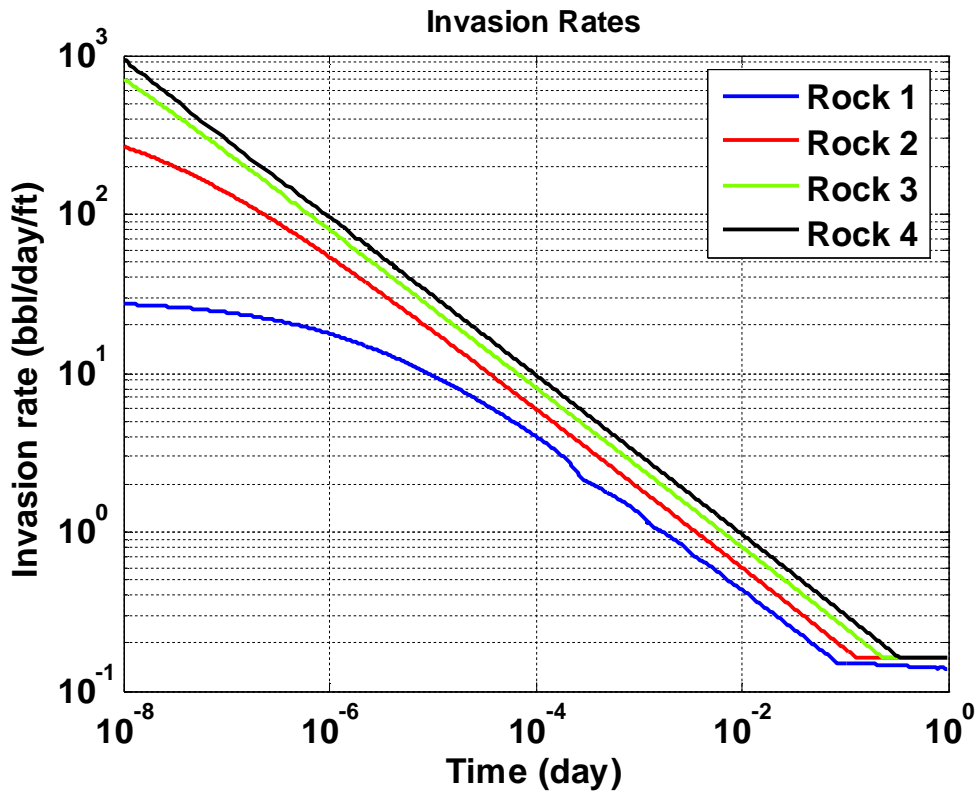


Figure 2.7: Water-base mud-filtrate invasion rates for different rock types vs. time.

Table 2.9: Average mud-filtrate invasion rates for different rock types.

| Invasion rate (bbl/day/ft) | Rock 1 | Rock 2 | Rock 3 | Rock 4 |
|----------------------------|--------|--------|--------|--------|
| WBM | 0.1557 | 0.1835 | 0.2019 | 0.2209 |
| OBM | 0.0596 | 0.0700 | 0.1000 | 0.1138 |

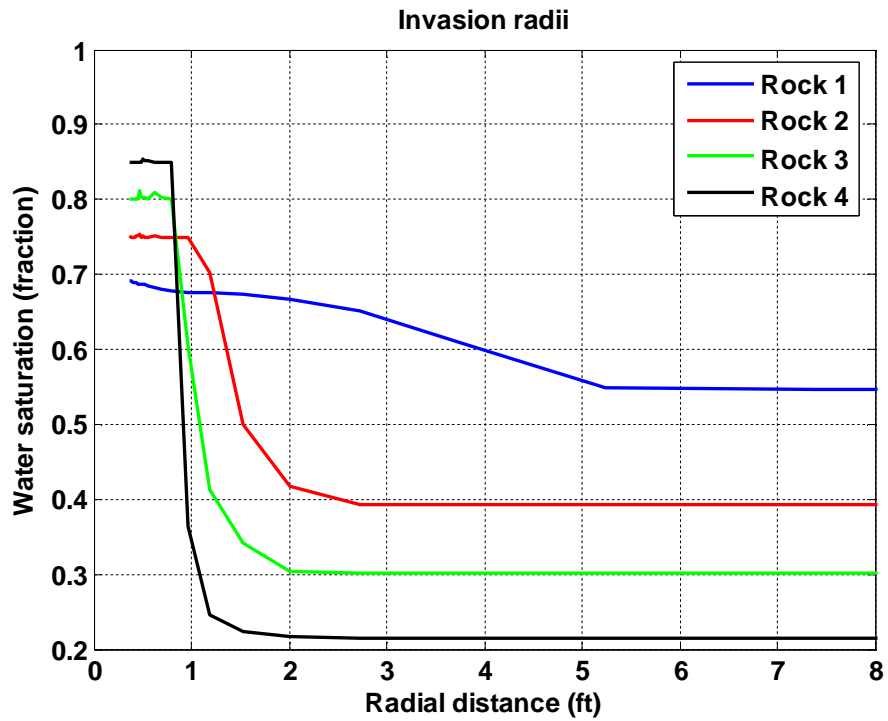


Figure 2.8: Radial distribution of water saturation describing radii of water-base mud-filtrate invasion for different rock types. The rock with the lowest permeability and porosity has the longest radius of invasion and the smoothest transition from invaded to uninvaded zones. The rock with the highest permeability and porosity exhibits the shortest radius of invasion and the sharpest transition from invaded to uninvaded zones.

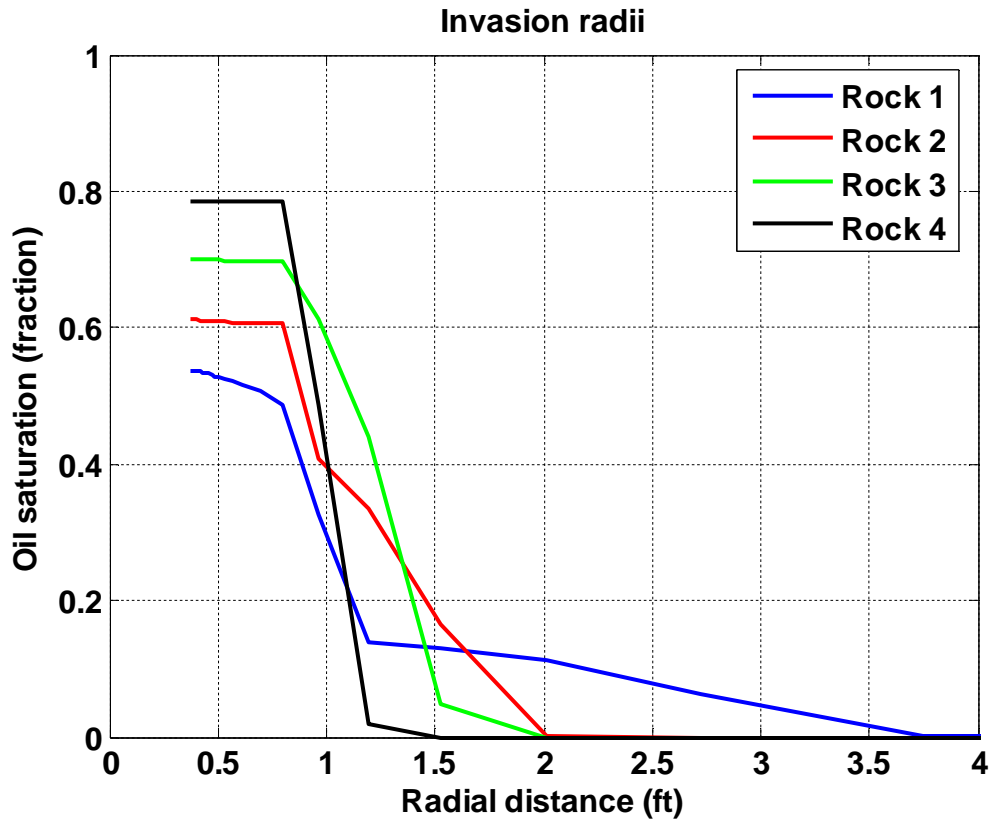


Figure 2.9: Radial distribution of oil saturation describing radii of oil-base mud-filtrate invasion for different rock types. The rock with the lowest permeability and porosity has the longest radius of invasion and the smoothest transition from invaded to uninvaded zones. The rock with the highest permeability and porosity exhibits the shortest radius of invasion and the sharpest transition from invaded to uninvaded zones.

CHAPTER 3

MODELING OF ACOUSTIC PROPERTIES

Fluid substitution is used in a broad range of applications in present-day reservoir characterization and for constructing reservoir flow models. Fluid-substitution equations are used to predict sonic velocities for a given value of fluid saturation.

Generally, there are two saturation patterns typically considered in partially saturated rocks. The first saturation pattern is the homogeneous pattern, wherein fluid saturation is assumed to be the same at the pore scale throughout the rock. The second saturation pattern is the patchy saturation pattern in which a large, fully saturated patch is surrounded by a dry region. In this report, I assume the patchy saturation model rather than the homogeneous saturation model. As emphasized by Smith et al. (2003) and Knight et al. (1998), the reasons for using this pattern are as follows: (a) disturbance of equilibrium due to drilling, production or water flooding, (b) smaller pores in water-wet rocks being dominantly filled with water due to capillary pressure, and (c) the heterogeneous nature of porous rocks and soils (often resulting in the heterogeneity of fluid distribution at scales larger than the pore or grain size). In the two saturation patterns, the shear modulus is the same for both dry and saturated regions. If we assume that the volumetric fraction of the saturated patch is S and the volumetric fraction of the dry patch is $1-S$, then following Packwood and Mavko (1995), we can use Hill's equation (1963) to calculate the effective bulk modulus, K_{satP} , of the volume of the rock independent of shape of the patches:

$$(K_{sat} + \frac{4}{3}\mu)^{-1} = S(K_0 + \frac{4}{3}\mu)^{-1} + (1-S)(K_1 + \frac{4}{3}\mu)^{-1}, \quad (3.1)$$

where μ is the dry shear modulus of the rock (in Pa). In the above expression, K_0 and K_1 are the bulk moduli of the liquid- and gas-saturated rock (in Pa), respectively, given by

$$K_0 = K_s \frac{\phi K_{dry} - (1+\phi)K_l K_{dry} / K_s + K_l}{(1-\phi)K_l + \phi K_s - K_l K_{dry} / K_s}, \quad (3.2)$$

and

$$K_1 = K_s \frac{\phi K_{dry} - (1+\phi)K_g K_{dry} / K_s + K_g}{(1-\phi)K_g + \phi K_s - K_g K_{dry} / K_s}, \quad (3.3)$$

where K_s is matrix bulk modulus (in Pa), ϕ is porosity (in fraction), K_l is liquid bulk modulus, K_{dry} is dry bulk modulus of the rock, and K_g is bulk modulus of gas (all in Pa).

Hill (1963) and Berryman and Milton (1991) advanced a formula for more than two phases to calculate the effective bulk modulus of the rock assuming a patchy saturation distribution:

$$K_{eff} = [\sum_{i=1}^n \frac{x_i}{(K_i + \frac{4}{3}\mu)}]^{-1} - \frac{4}{3}\mu, \quad (3.4)$$

where n is the number of phases, x_i is the saturation of the i -th phase (in fraction), μ is the shear modulus of the rock completely filled with the i -th fluid, and K_{eff} is the effective bulk modulus of the rock (both in Pa). The shear modulus of the rock is assumed to be the same regardless of the type of fluid occupying the pores. Therefore,

$$\mu_{sat} = \mu_{dry} = \mu. \quad (3.5)$$

The dry bulk and shear moduli of the rock are calculated using the correlations proposed by Geerstma (1961):

$$\frac{1}{K_{dry}} = \frac{1}{K_s}(1 + 50\phi), \quad (3.6)$$

and

$$\frac{1}{\mu_{dry}} = \frac{1}{\mu_s}(1 + 50\phi), \quad (3.7)$$

where ϕ is porosity (in fraction), K_s and μ_s are bulk and shear moduli of the matrix, respectively, and K_{dry} and μ_{dry} are dry bulk and shear moduli of the rock (all in Pa), respectively.

Compressional- and shear-wave velocities are calculated using the equations

$$V_p = \sqrt{\frac{K_{eff} + \frac{4}{3}\mu_{sat}}{\rho}}, \quad (3.8)$$

and

$$V_s = \sqrt{\frac{\mu_{sat}}{\rho}}, \quad (3.9)$$

where K_{eff} is the effective bulk modulus of the rock, and μ_{sat} is the saturated rock shear modulus (both in Pa) which is equal to the dry bulk modulus of the rock and ρ is the bulk density of the rock (in kg/m^3), given by

$$\rho = (1 - \phi)\rho_s + \phi(S_w\rho_w + S_g\rho_g + S_{oil}\rho_{oil}), \quad (3.10)$$

where ϕ is porosity (in fraction), ρ_s is the density of the matrix (in kg/m^3), S_w , S_g , and S_{oil} are saturations of water, gas, and oil respectively; and ρ_w , ρ_g , and ρ_{oil} are densities of water, gas, and oil (all in kg/m^3), respectively.

Figure 3.1 illustrates the fluid-substitution sensitivity analysis for water and gas mixtures using Equations 3.8 and 3.9 and the patchy saturation model equations (Equations 3.2 to 3.7). The dashed lines identify shear-wave velocities while solid lines identify compressional-wave velocities. The figure clearly indicates that compressional-wave velocity is much more sensitive to changes in water saturation than shear-wave velocity. Quantitatively, compressional-wave velocity varies from 27% to 32% for different rock types, while shear-wave velocity varies less than 5% as water saturation changes from 0 to 1. The figure also implies that as porosity decreases, the formation becomes harder. A formation is referred to as hard if the shear-wave velocity is greater than the speed of sound in the mud (otherwise, it is called soft). Most importantly, the relative change of compressional- and shear-wave velocities with water saturation increases with increasing porosity.

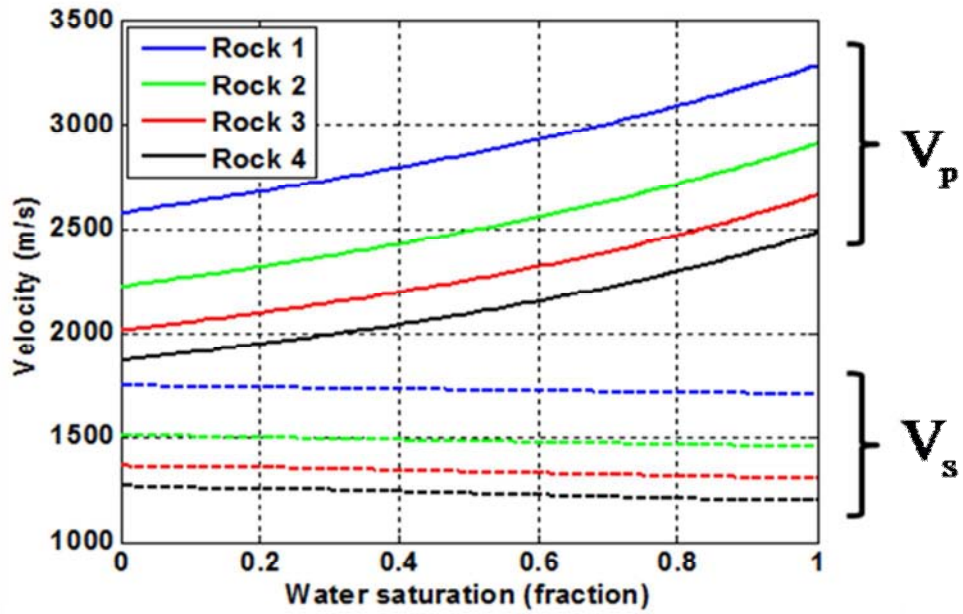


Figure 3.1: Fluid-substitution sensitivity analysis for the assumed rock types. Solid lines identify compressional-wave velocities and dashed lines identify shear-wave velocities.

Table 3.1 summarizes the assumed values for bulk and shear moduli of sandstone, water, oil, and gas. These values are taken from Wang et al. (2007). The values for sandstone are assumed to be the same as those of quartz.

Table 3.1: Assumed values of bulk and shear moduli for water, oil, gas, and quartz.

| | Water | Oil | Gas | Quartz |
|-------------|-------|------|--------|--------|
| K (GPa) | 2.38 | 0.67 | 0.0208 | 37 |
| μ (GPa) | 0 | 0 | 0 | 44 |

Table 3.2 lists the dry bulk and shear moduli of the four assumed rock types using Equations 3.8 and 3.9, respectively.

Table 3.2: Dry bulk and shear moduli for the four assumed rock types.

| | Rock 1 | Rock 2 | Rock 3 | Rock 4 |
|--------------------------|---------------|---------------|---------------|---------------|
| K_{dry} (GPa) | 6.17 | 4.35 | 3.36 | 2.74 |
| μ_{dry} (GPa) | 7.33 | 5.18 | 4.00 | 3.26 |

Using the calculated dry bulk and shear moduli and Equations 3.1 to 3.5, I transform the spatial distributions of fluid saturation to spatial distributions of density, and compressional- and shear-wave velocities for each rock type both before and after invasion. Figures 3.2 through 3.9 show the spatial distributions of density, and P-wave and S-wave slownesses for rock types 1 to 4 after mud-filtrate invasion has taken place (slowness is the inverse of velocity expressed in $\mu\text{s}/\text{ft}$). According to the figures, the effect of gravity segregation on fluid distribution after invasion is maximum for the fourth rock type (maximum porosity and permeability) and minimum for the first rock type (minimum porosity and permeability). Moreover, the fourth rock type exhibits the shortest radius of invasion and the sharpest transition from the invaded to the uninvaded zones, whereas the first rock type exhibits the longest radius of invasion and the smoothest transition from the invaded to the uninvaded zones. The figures also suggest that oil-base mud (OBM) invades shallower into the formation than water-base mud (WBM).

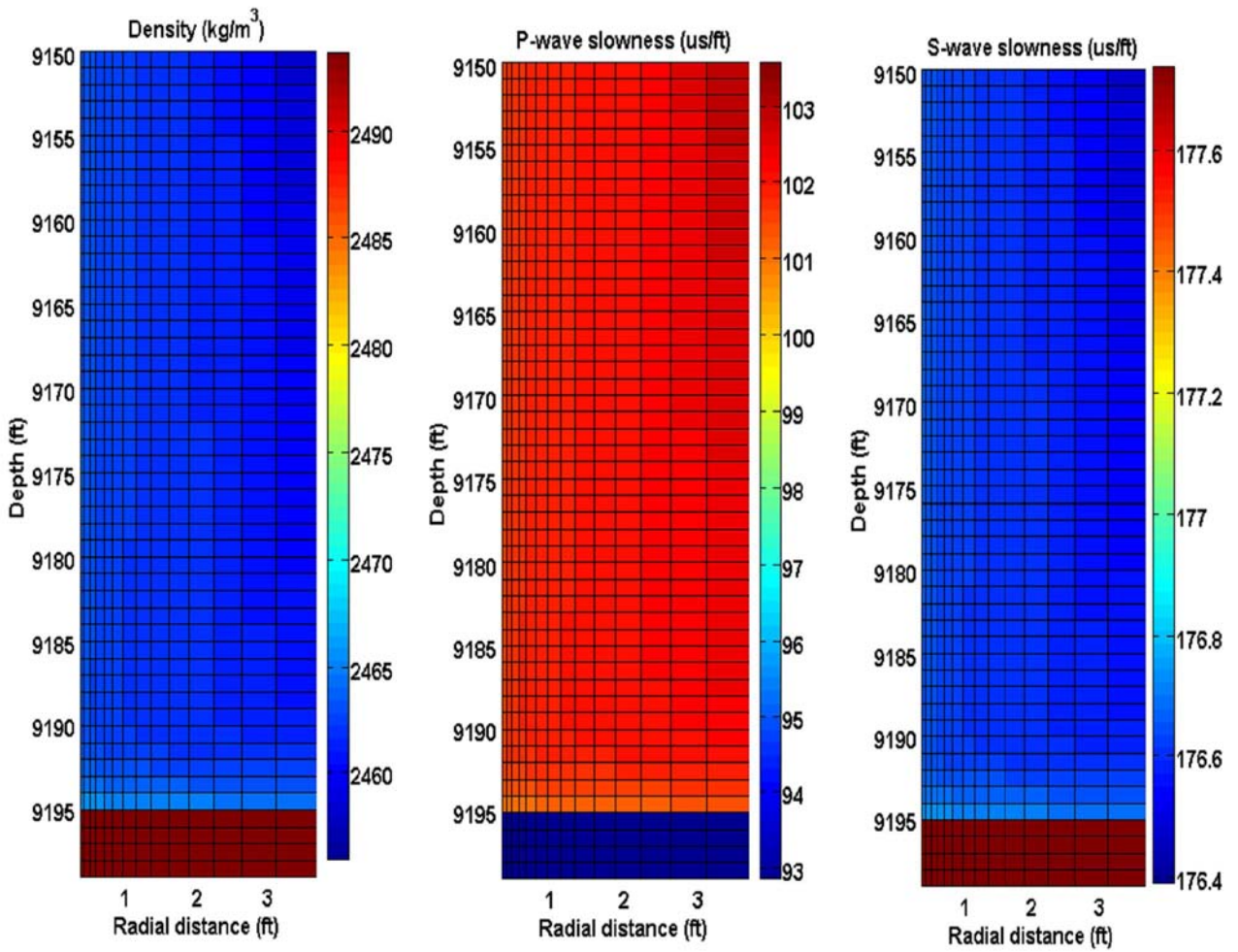


Figure 3.2: Spatial distribution of acoustic properties for the first rock type after water-base mud-filtrate (WBM) invasion. Left panel: spatial distribution of density. Central panel: spatial distribution of P-wave slowness. Right panel: spatial distribution of S-wave slowness.

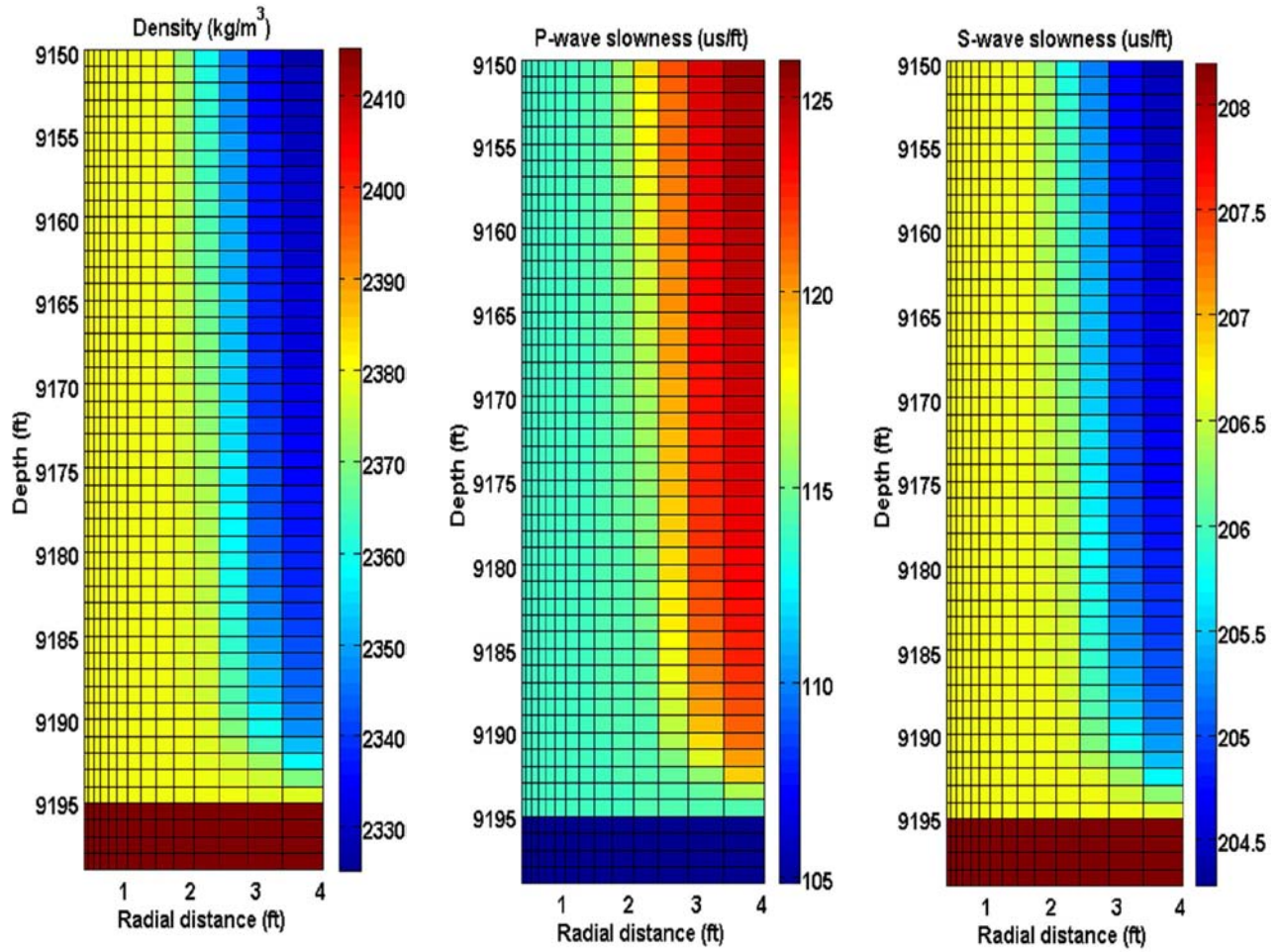


Figure 3.3: Spatial distribution of acoustic properties for the second rock type after water-base mud-filtrate (WBM) invasion. Left panel: spatial distribution of density. Central panel: spatial distribution of P-wave slowness. Right panel: spatial distribution of S-wave slowness.

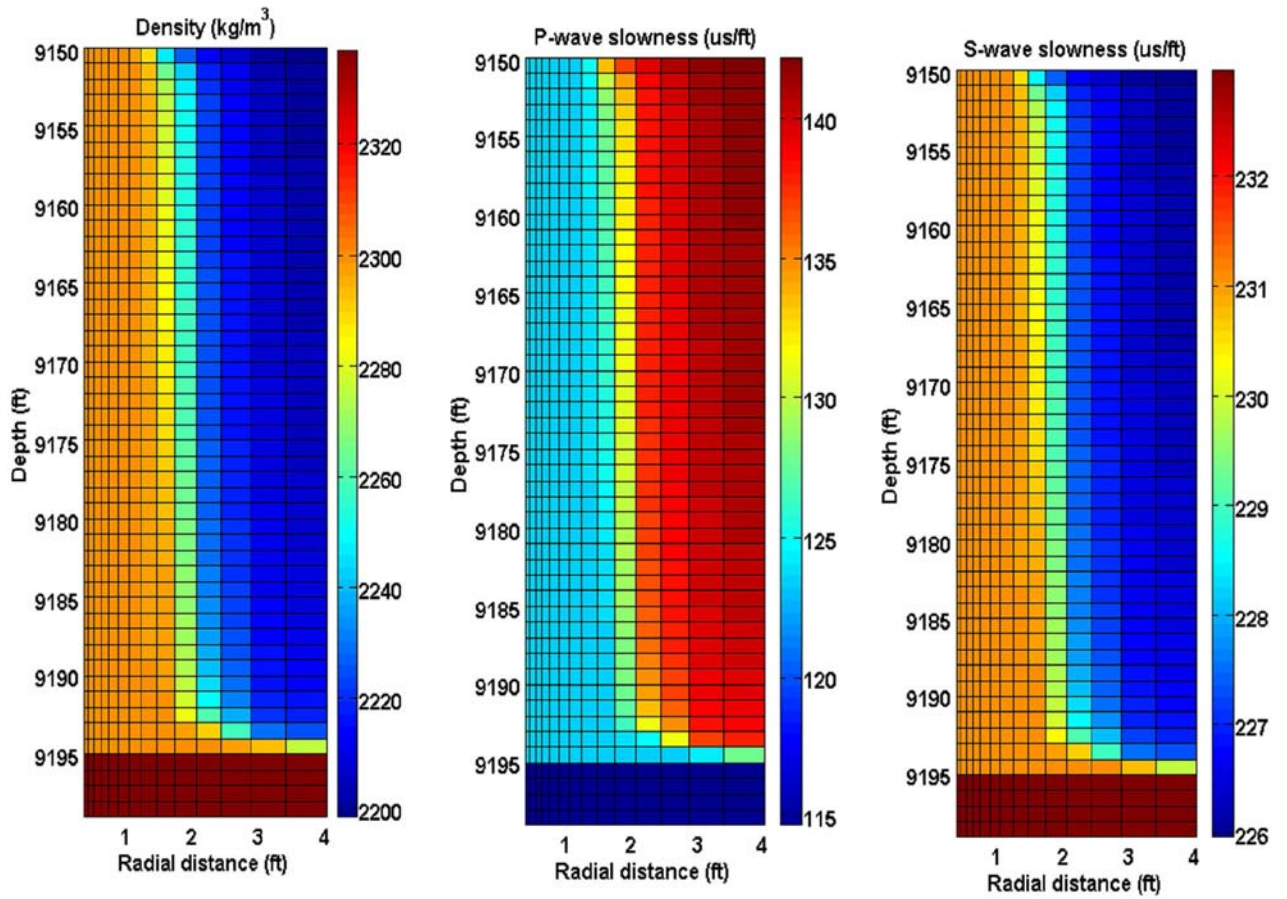


Figure 3.4: Spatial distribution of acoustic properties for the third rock type after water-base mud-filtrate (WBM) invasion. Left panel: spatial distribution of density. Central panel: spatial distribution of P-wave slowness. Right panel: spatial distribution of S-wave slowness.

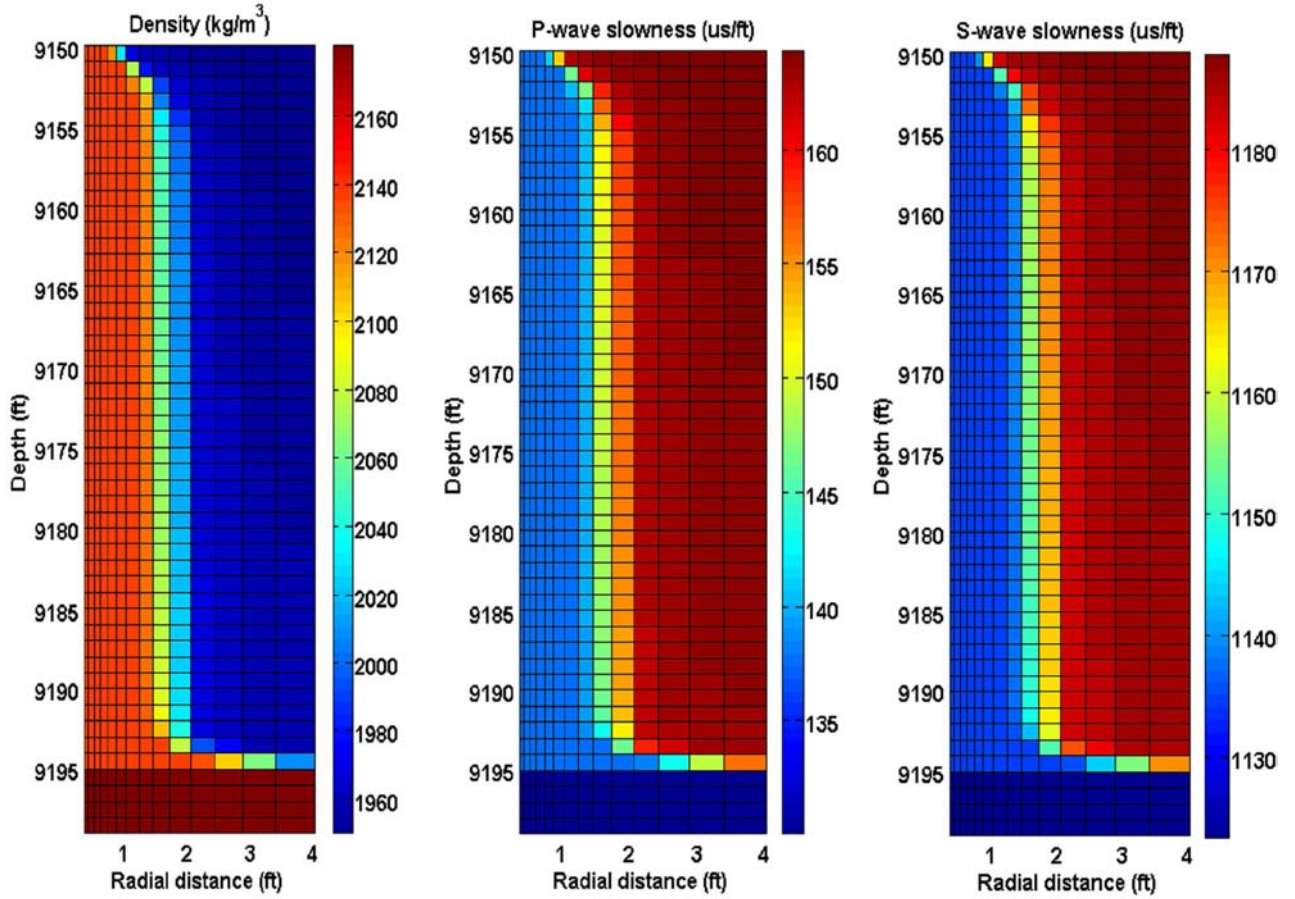


Figure 3.5: Spatial distribution of acoustic properties for the fourth rock type after water-base mud-filtrate (WBM) invasion. Left panel: spatial distribution of density. Central panel: spatial distribution of P-wave slowness. Right panel: spatial distribution of S-wave slowness.

Figures 3.6 through 3.9 show the spatial distribution of density as well as P-wave and S-wave slownesses for the four assumed rock types after oil-base mud-filtrate invasion.

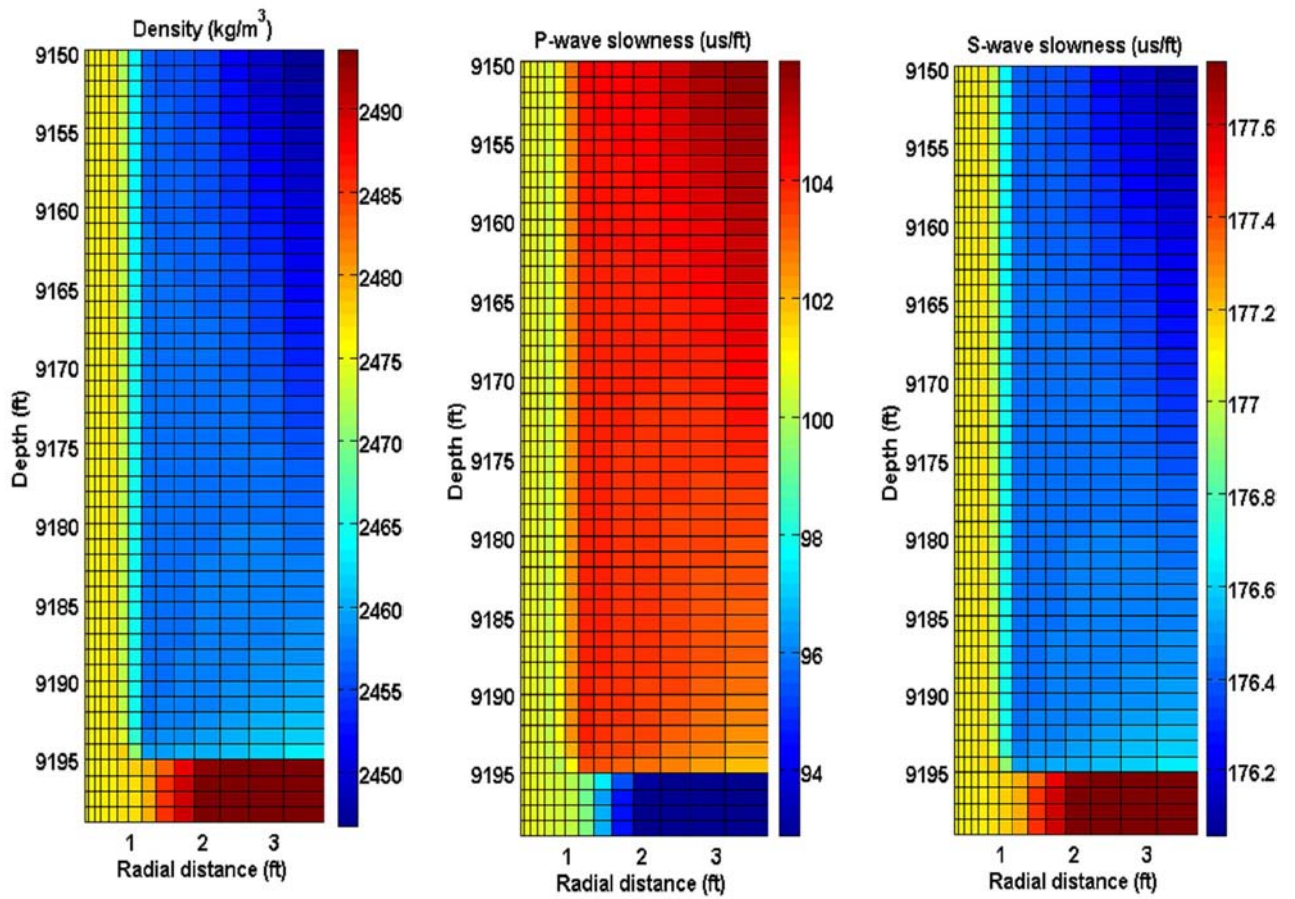


Figure 3.6: Spatial distribution of acoustic properties for the first rock type after oil-base mud-filtrate (OBM) invasion. Left panel: spatial distribution of density. Central panel: spatial distribution of P-wave velocity. Right panel: spatial distribution of S-wave velocity.

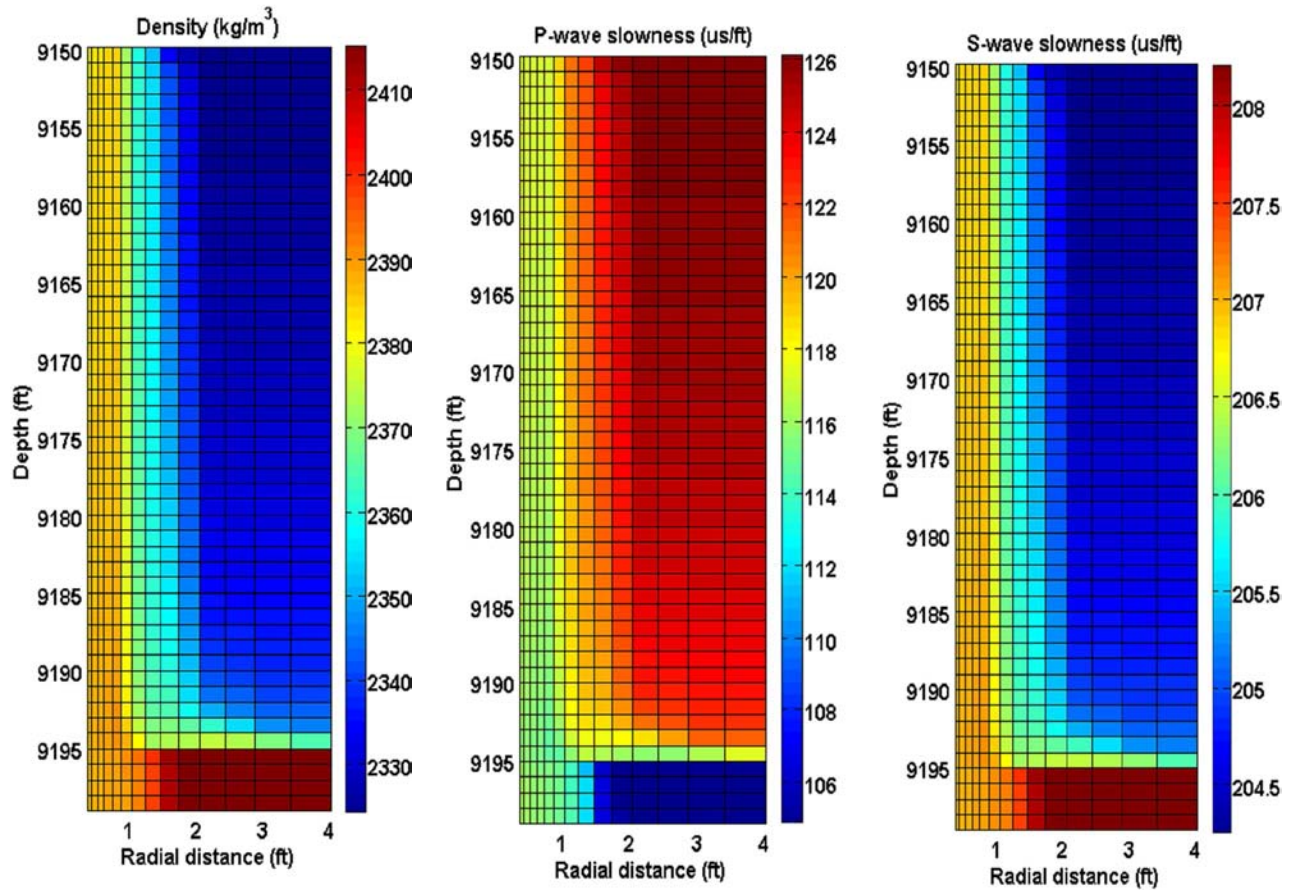


Figure 3.7: Spatial distribution of acoustic properties for the second rock type after oil-base mud-filtrate (OBM) invasion. Left panel: spatial distribution of density. Central panel: spatial distribution of P-wave velocity. Right panel: spatial distribution of S-wave velocity.

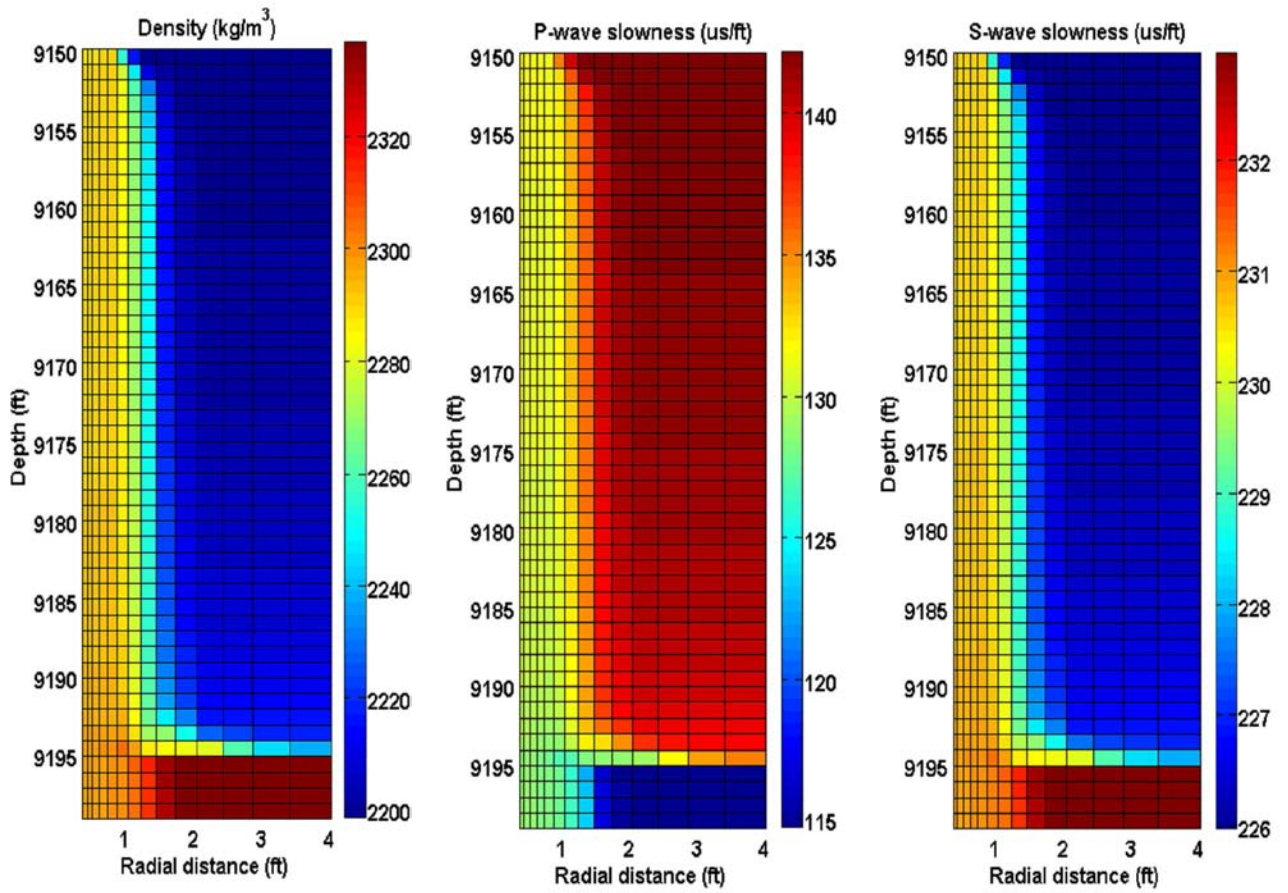


Figure 3.8: Spatial distribution of acoustic properties for the third rock type after oil-base mud-filtrate (OBM) invasion. Left panel: spatial distribution of density. Central panel: spatial distribution of P-wave velocity. Right panel: spatial distribution of S-wave velocity.

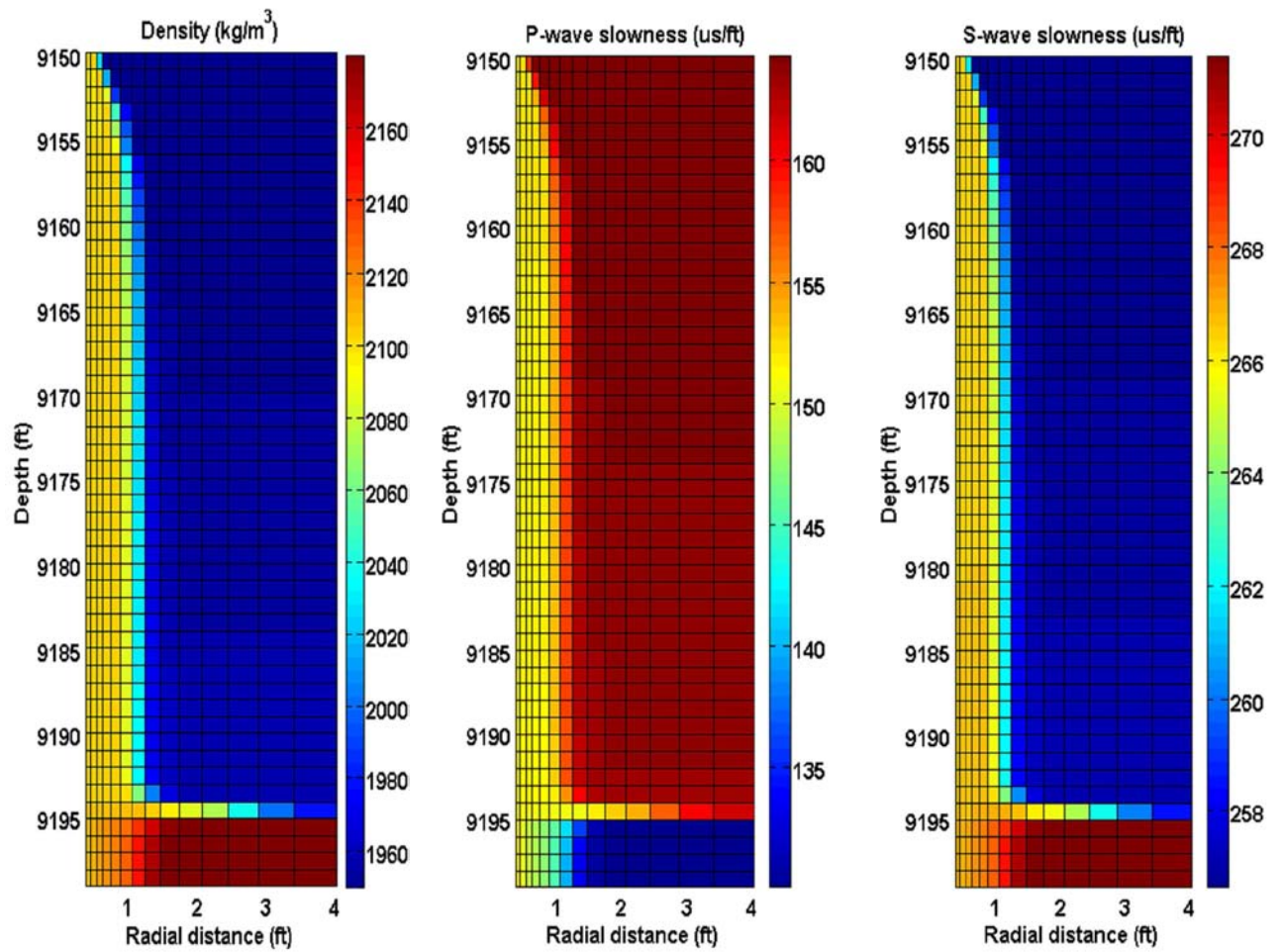


Figure 3.9: Spatial distribution of acoustic properties for the fourth rock type after oil-base mud-filtrate (OBM) invasion. Left panel: spatial distribution of density. Central panel: spatial distribution of P-wave velocity. Right panel: spatial distribution of S-wave velocity.

CHAPTER 4

SIMULATION RESULTS

The spatial distributions of compressional-wave velocity, shear-wave velocity, and density are input into the two-dimensional (2D) sonic simulator developed by the Formation Evaluation Group of The University of Texas at Austin (Ma, 2007). Outputs from the 2D sonic simulator are time-domain waveforms. Time-domain waveforms are subsequently analyzed with frequency dispersion analysis. This analysis is performed using an algorithm based on the “weighted spectral semblance method” (Tang and Cheng, 2004).

The source-receiver configuration assumed in the following simulations is adapted from Schlumberger’s new array sonic tool, Sonic Scanner (Pistre et al., 2005). Figure 4.1 shows the schematic of the tool. For each rock type, I compare frequency dispersion analysis results, both before and after invasion, at two measurement locations for monopole and dipole sources. At the first measurement location, the receiver array is located at the top of the capillary transition zone; at the remaining location, half of the receivers are inside the water zone and half are outside the water zone at the bottom of the capillary transition zone. Figure 4.2 shows the two measurement locations considered in this report. The dipole source is simulated with the central frequency of 3 KHz, whereas the monopole source is simulated with the central frequency of 8 KHz. I assume a Ricker wavelet in all the numerical simulations.

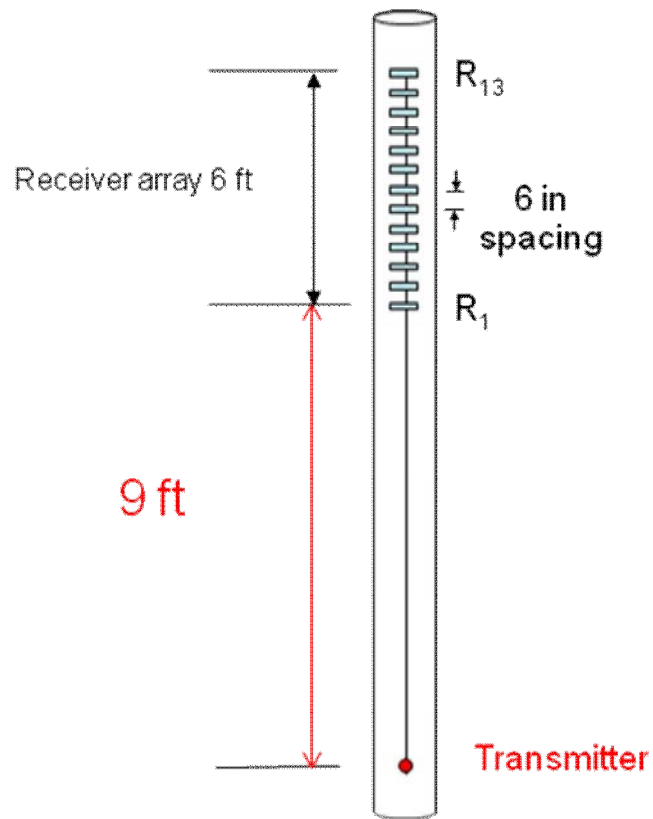


Figure 4.1: Schematic of the wireline sonic tool assumed in the numerical simulations.

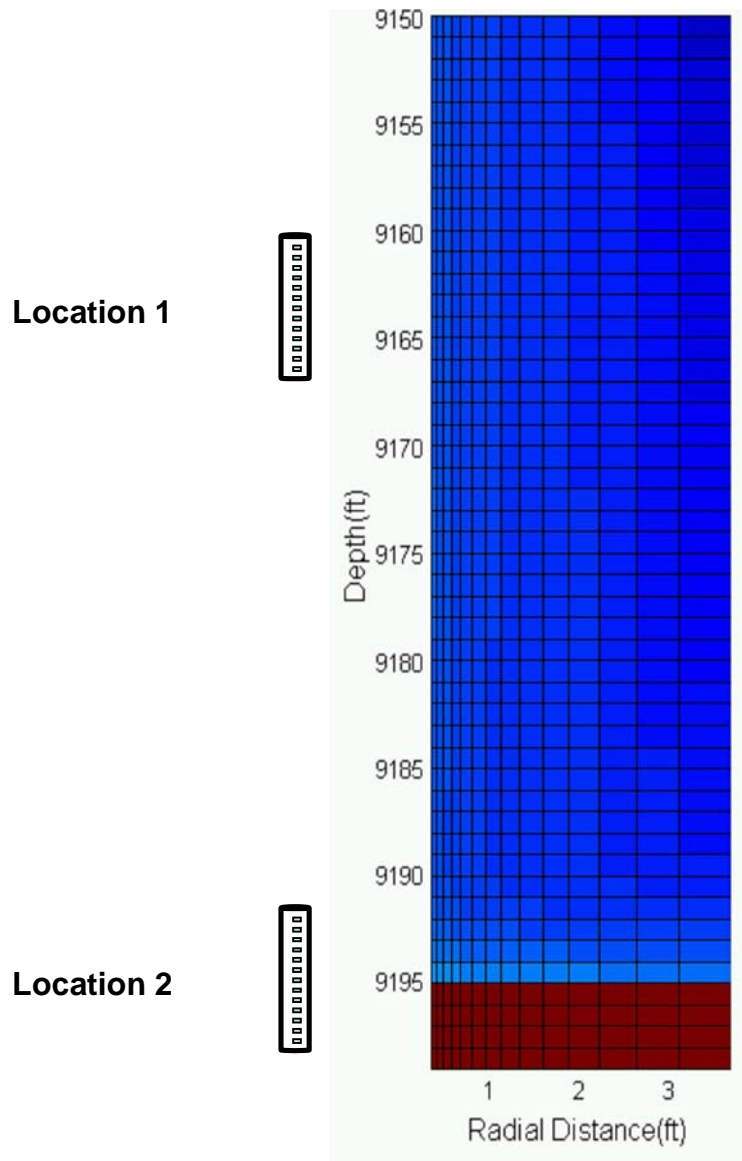


Figure 4.2: Location of the receiver array for each measurement point.

4.1 WATER-BASE MUD-FILTRATE (WBM) INVASION

a) First rock type ($\Phi=10\%$ and $K=1.5$ md)

First measurement location

Figure 4.3 shows dipole frequency dispersion results for the first rock type, both before and after invasion, corresponding to the first measurement location in which the receivers are at the top of the capillary transition zone. The plot indicates that there is negligible difference between flexural-wave frequency dispersion before and after water-base mud-filtrate invasion at both low and high frequencies for a low-porosity rock. The reason for this effect is the small range of water saturation available in this rock. As shown earlier in Table 2.2, irreducible water saturation is 0.45 and residual gas saturation is 0.30 in this type of rock, causing the water saturation to range between 0.45 and 0.7. Therefore, small variations of water saturation together with low porosity result in small changes in compressional- and shear-wave velocities. Black and red horizontal lines in Figure 4.3 identify formation shear-wave slowness at the wellbore interface before and after invasion, respectively.

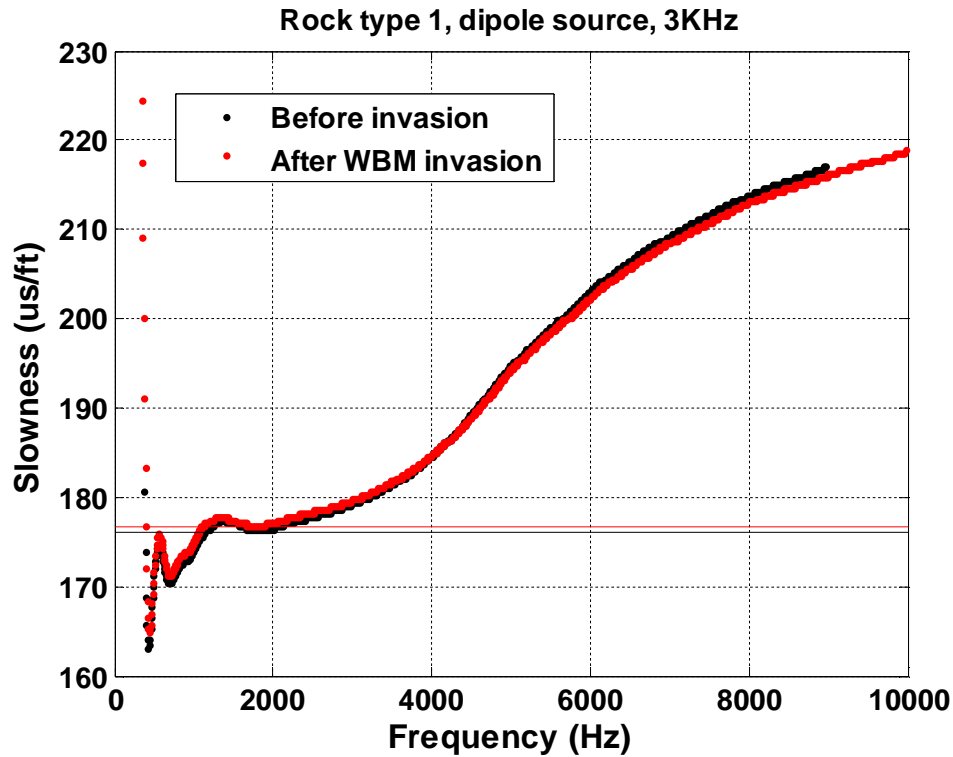


Figure 4.3: Frequency dispersion results for the first rock type with a dipole source at the first measurement location. Red and black curves identify results for after and before WBM invasion, respectively. Black and red lines identify the formation shear slowness before and after invasion, respectively.

Figure 4.4 compares simulation results before and after WBM invasion at the same measurement location with a monopole source. Two modes of propagation are visible in the figure: Stoneley and pseudo-Rayleigh waves. As expected, the Stoneley wave is less dispersive (different frequency components propagate at different speeds) than pseudo-Rayleigh waves. The pseudo-Rayleigh mode asymptotes to the shear slowness of the formation. Since this is a hard (fast) formation, the compressional wave is not detected in the frequency dispersion analysis. The plot suggests that both Stoneley and pseudo-Rayleigh waves are almost insensitive to WBM invasion.

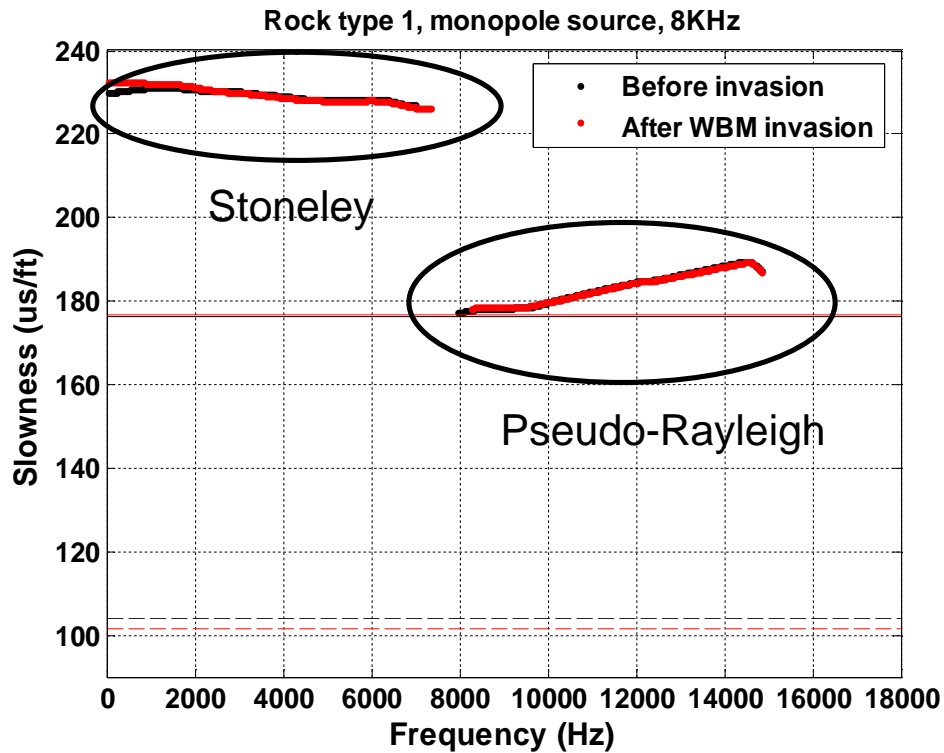


Figure 4.4: Frequency dispersion results for the first rock type with a monopole source at the first measurement location. Red and black curves identify results for after and before WBM invasion, respectively. Stoneley and pseudo-Rayleigh modes are circled separately. Solid black and red lines identify the formation shear slowness before and after invasion, respectively. Dashed black and red lines identify the formation compressional slowness before and after invasion, respectively.

Second measurement location

Figure 4.5 shows dipole frequency dispersion results for the first rock type, both before and after invasion corresponding to the second measurement location in which half of the receivers are inside the water zone and half of them are outside the water zone. Again, because of the narrow range of water saturation and the low porosity of the

formation, there is no appreciable difference in the simulation results before and after invasion.

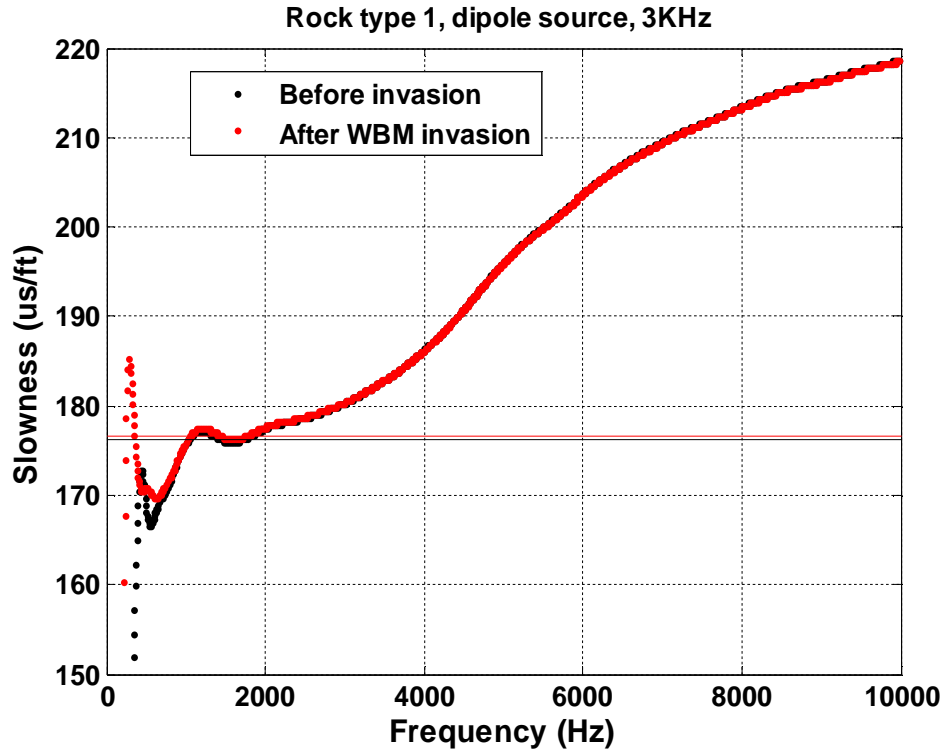


Figure 4.5: Frequency dispersion results for the first rock type with a dipole source at the second measurement location. Red and black curves identify results for after and before WBM invasion, respectively. Black and red lines identify the formation shear slowness before and after invasion, respectively.

Figure 4.6 shows the monopole frequency dispersion results for both before- and after-invasion stages at the second measurement location. Again, there is no discrepancy between the two curves. Stoneley and pseudo-Rayleigh modes are visible on the plot.

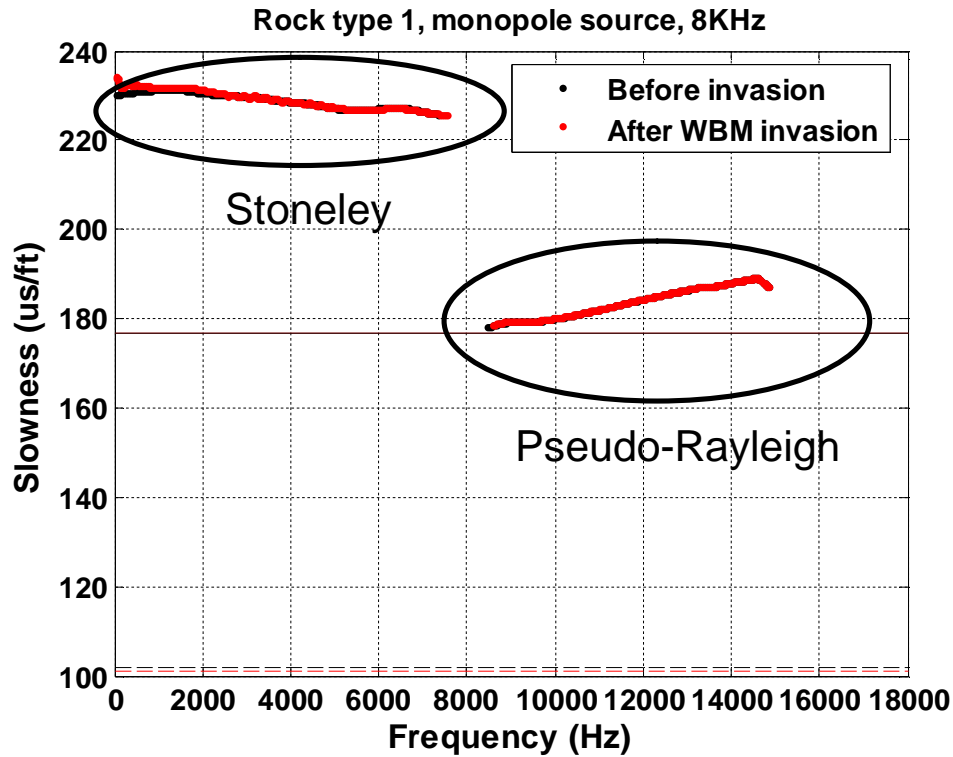


Figure 4.6: Frequency dispersion results for the first rock type with a monopole source at the second measurement location. Red and black curves identify results for after and before WBM invasion, respectively. Stoneley and pseudo-Rayleigh modes are circled separately. The solid line identifies the formation shear slowness at the top receiver. Dashed black and red lines identify the formation compressional slowness before and after invasion at the top receiver, respectively.

b) Second rock type ($\Phi=15\%$ and $K=15$ md)

First measurement location

Figure 4.7 shows frequency dispersion results for the second rock type, both before and after invasion corresponding to the first measurement location. Porosity and range of water saturation have increased in this case, and I observe measureable differences between simulation results for before- and after-invasion stages. The

discrepancy is lower at lower frequencies and increases as frequency increases. The reason for this behavior is that high-frequency components sense shallower into the formation than low-frequency components. It is evident that invasion mostly affects the near-wellbore region.

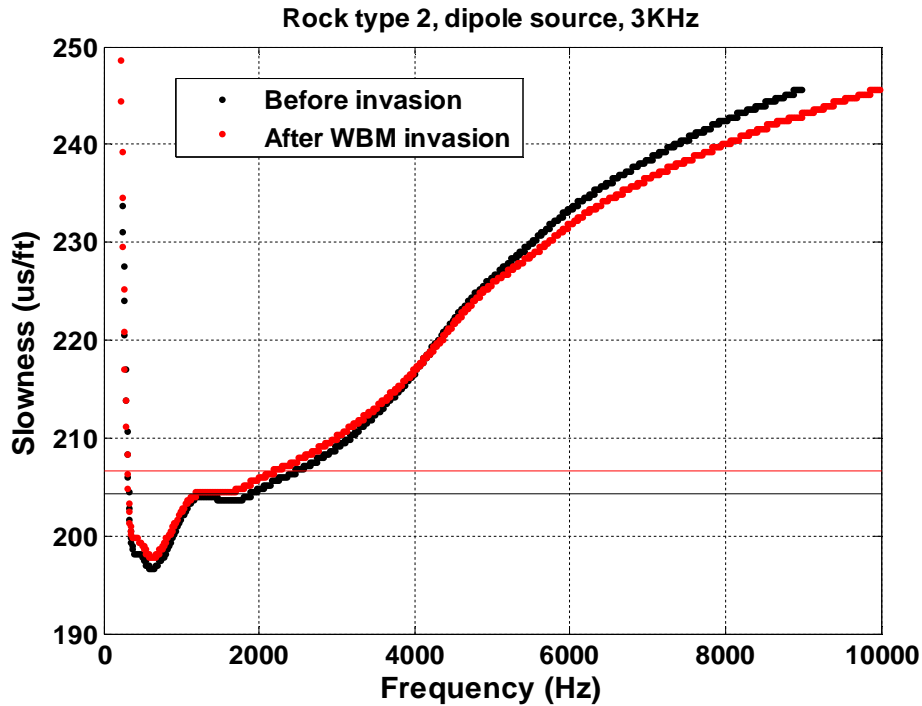


Figure 4.7: Frequency dispersion results for the second rock type with a dipole source at the first measurement location. Red and black curves identify results for after and before WBM invasion, respectively. Black and red lines identify the formation shear slowness before and after invasion, respectively.

Figure 4.8 shows the effect of invasion on monopole frequency dispersion results at the first measurement location. Frequency dispersion results before invasion indicate the presence of a pseudo-Rayleigh wave, which is not present after WBM invasion. The figure suggests that the Stoneley wave becomes less dispersive after WBM invasion.

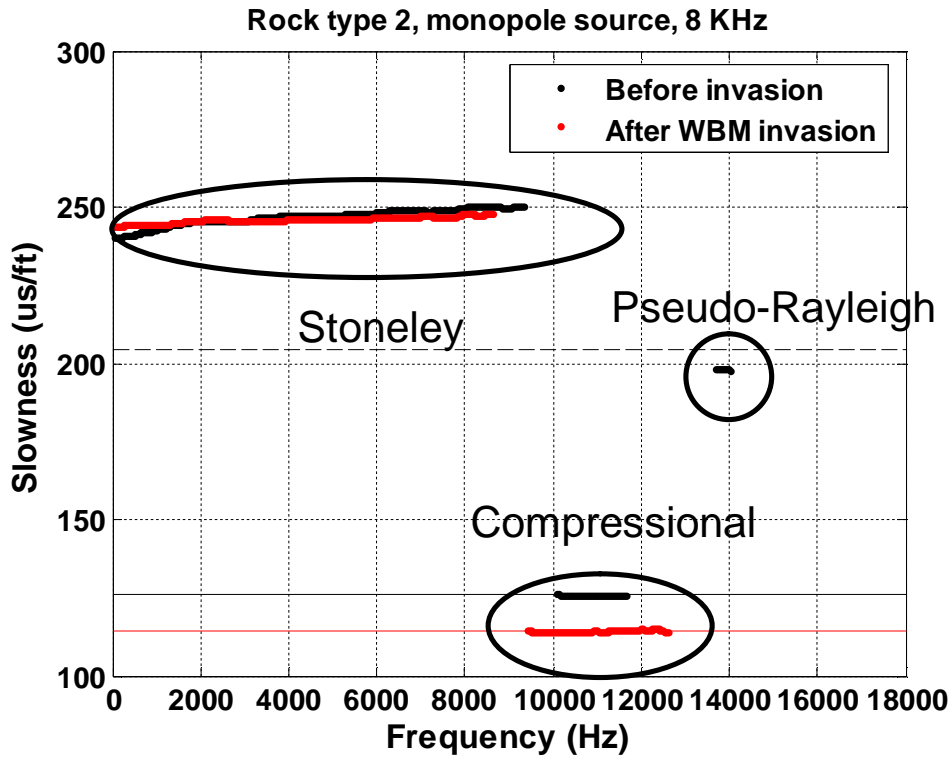


Figure 4.8: Frequency dispersion results for the second rock type with a monopole source at the first measurement location. Red and black curves identify results for after and before WBM invasion, respectively. Stoneley, compressional and pseudo-Rayleigh modes are circled separately. The dashed black line represents uninvaded formation shear-wave slowness. Solid black and red lines identify the formation compressional-wave slowness before and after invasion, respectively.

Second measurement location

Figure 4.9 shows the flexural-wave frequency dispersion results before and after WBM invasion at the second measurement location. The figure indicates that low-frequency components before and after WBM invasion tend to separate. Gravity segregation causes this effect; as the porosity and permeability of the rock increase, water has a higher tendency to segregate due to gravity. However, high-frequency components

exhibit less variation in the presence of WBM invasion than low-frequency components in this case.

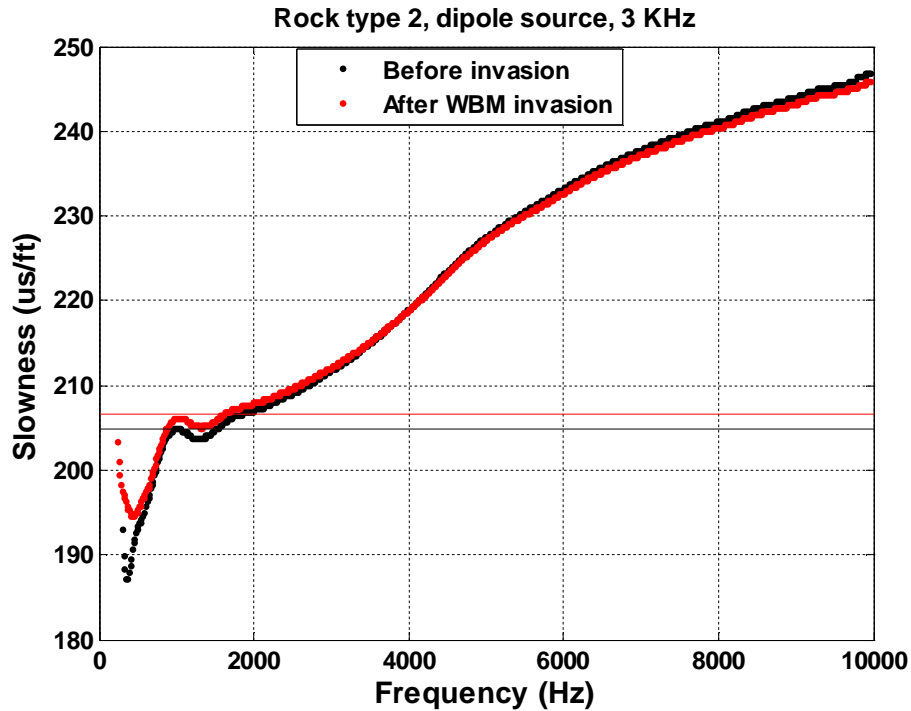


Figure 4.9: Frequency dispersion results for the second rock type with a dipole source at the second measurement location. Red and black curves identify results for after and before WBM invasion, respectively. Solid black and red lines identify the formation shear-wave slowness before and after invasion, respectively.

Figure 4.10 shows monopole frequency dispersion results at the second measurement location. At low frequencies, the Stoneley wave exhibits higher sensitivity to WBM invasion than at high frequencies. On the other hand, the compressional wave shows less sensitivity to WBM invasion due to the small perturbation of water saturation at the bottom of the capillary transition zone in comparison to Figure 4.8 (top segment of the capillary transition zone).

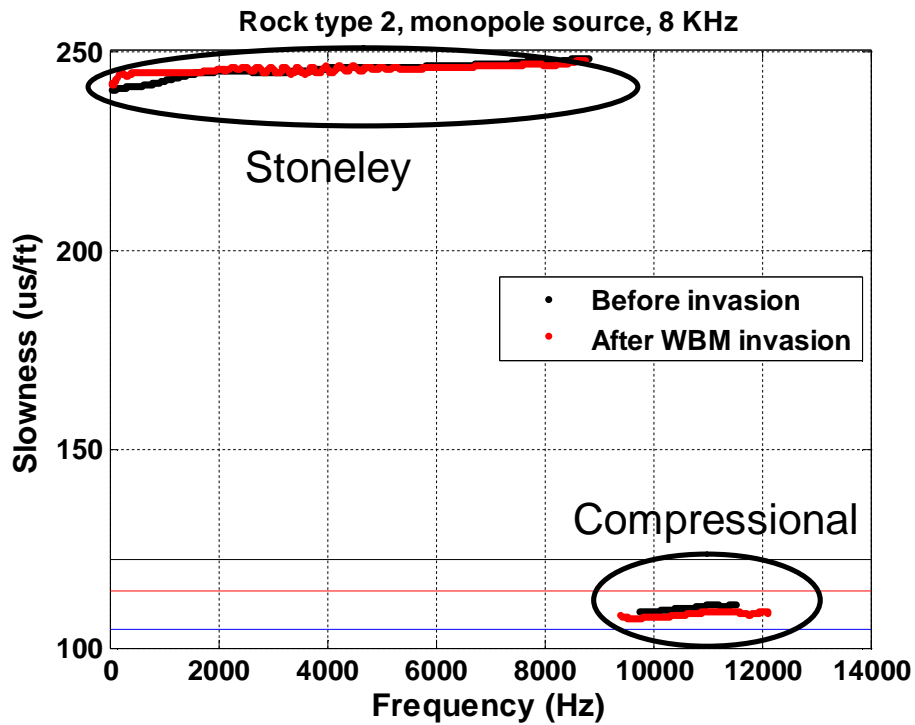


Figure 4.10: Frequency dispersion results for the second rock type with a monopole source at the second measurement location. Red and black curves identify results for after and before WBM invasion, respectively. Black and red lines identify the formation compressional-wave slowness before and after invasion at the location of the top receiver, respectively. The blue line identifies the water-filled rock compressional slowness.

c) Third rock type ($\Phi=20\%$ and $K=100$ md)

First measurement location

Figure 4.11 shows dipole frequency dispersion results for the third rock type at the first measurement location both before and after WBM invasion. As the plot indicates, the low-frequency components are still close together, while high-frequency components tend to separate due to relatively large water saturation perturbation originating from WBM invasion.

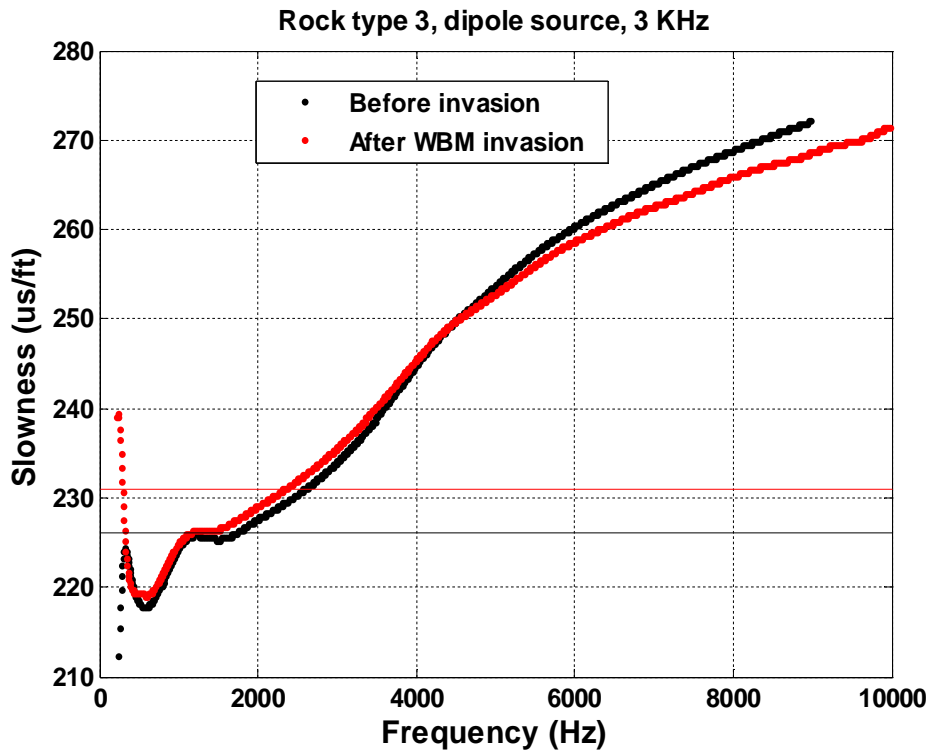


Figure 4.11: Frequency dispersion results for the third rock type with a dipole source at the first measurement location. Red and black curves identify results for after and before WBM invasion, respectively. Black and red lines identify the formation shear slowness before and after invasion, respectively.

Figure 4.12 shows the effect of WBM invasion on monopole frequency dispersion results for the third rock type at the first measurement location. The compressional mode appears in a broader range of frequencies compared to the previous rock types. In addition, the Stoneley mode becomes more dispersive and exhibits greater discrepancy between before- and after-invasion stages at low frequencies than at high frequencies. The compressional wave becomes slightly dispersive after invasion.

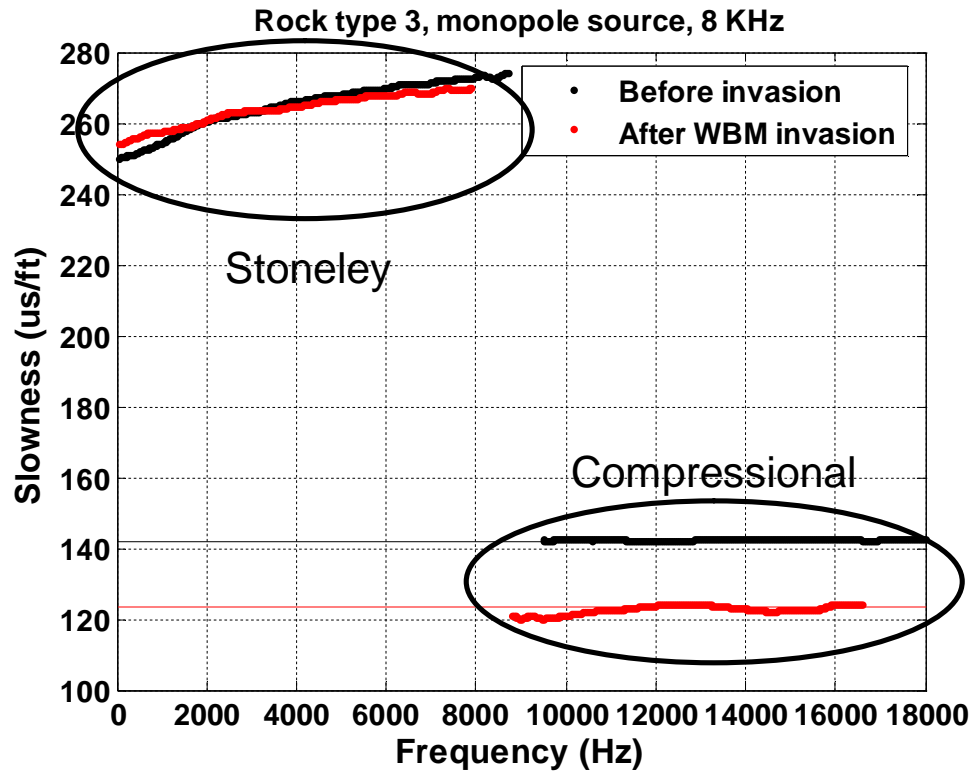


Figure 4.12: Frequency dispersion results for the third rock type with a monopole source at the first measurement location. Red and black curves identify results for after and before WBM invasion, respectively. Stoneley and compressional modes are circled separately. Black and red lines identify the formation compressional-wave slowness before and after invasion, respectively.

Second measurement location

Figure 4.13 shows flexural-wave frequency dispersion results both before and after WBM invasion at the second measurement location, where half of the receivers are in the water zone and the rest are outside the water zone, at the bottom of the capillary transition zone. Due to the increase of permeability and porosity, gravity segregation has a more drastic effect on frequency dispersion results. As Figure 4.13 suggests, the low-

frequency asymptotes further separate between results for before- and after-invasion stages.

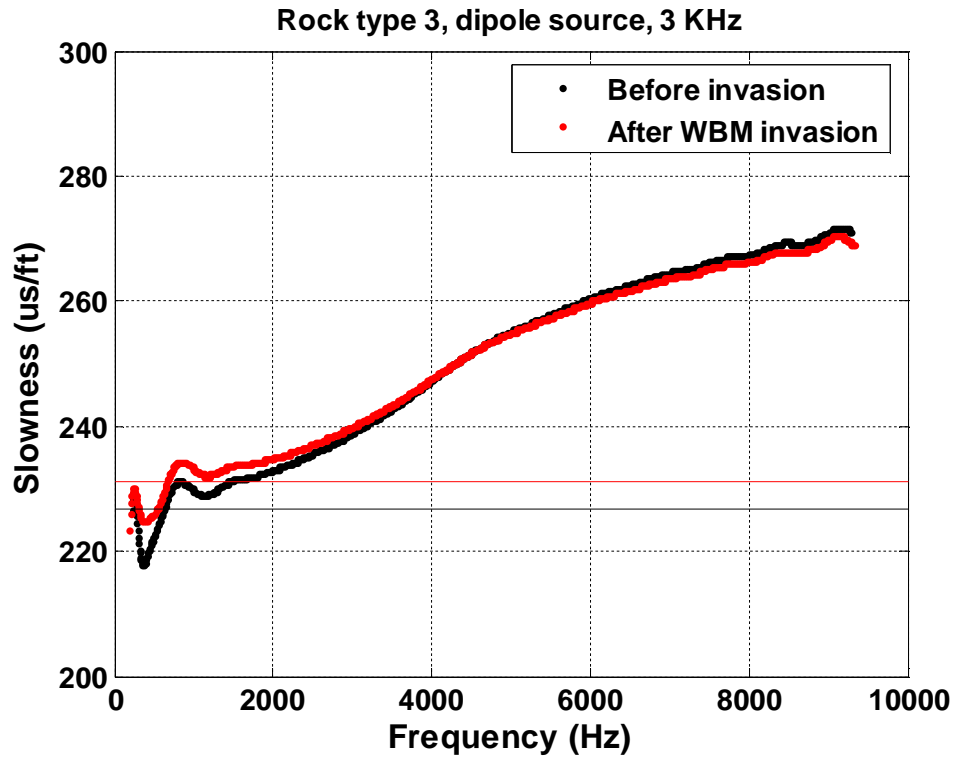


Figure 4.13: Frequency dispersion results for the third rock type with a dipole source at the second measurement location. Red and black curves identify results for after and before WBM invasion, respectively. Black and red lines identify the formation shear slowness at the top receiver before and after invasion, respectively.

Figure 4.14 shows modes of propagation before and after WBM invasion for a monopole source. The Stoneley wave after WBM invasion is less dispersive than before invasion, whereas the compressional wave before invasion splits into two separate parts. The first part, located at a lower frequency range, exhibits higher slownesses and is therefore closer to the formation compressional slowness at the location of the top receiver. The second part, which occurs at a higher frequency range, exhibits a slowness

close to the formation compressional slowness in the water zone and is slightly dispersive. Results clearly depict the mode separation originating from a sharp change in compressional-wave velocity (or slowness) of the formation. However, after WBM invasion, no mode separation is observed because invasion distorts the capillary transition zone.

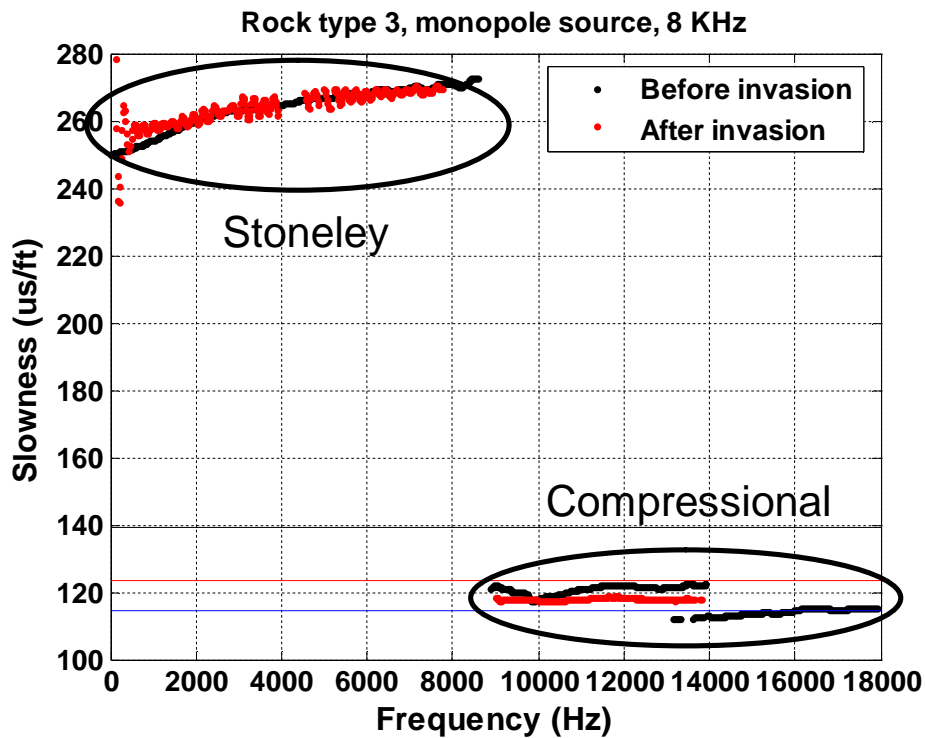


Figure 4.14: Frequency dispersion results for the third rock type with a monopole source at the second measurement location. Red and black curves identify results for after and before WBM invasion, respectively. Stoneley and compressional modes are circled separately. Black and red lines identify the formation compressional-wave slowness before and after invasion at the location of the top receiver, respectively. The blue line identifies the water-filled rock compressional slowness.

d) Fourth rock type ($\Phi=25\%$ and $K=500$ md)

First measurement location

Figure 4.15 shows flexural-wave dispersion before and after WBM invasion. The figure suggests that both curves exhibit the same zero-frequency asymptote; yet they develop differences as frequency increases. These differences are maximum at the central frequency range (2500 Hz to 4000 Hz).

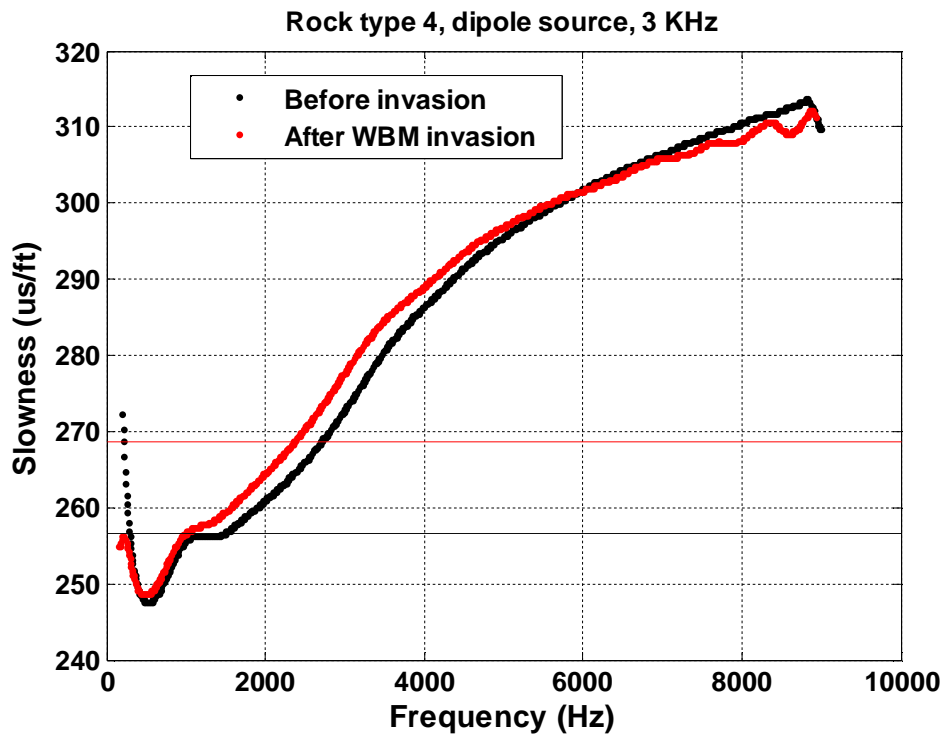


Figure 4.15: Frequency dispersion results for the fourth rock type with a dipole source at the first measurement location. Red and black curves identify results for after and before WBM invasion, respectively. Black and red lines identify formation shear slowness before and after invasion, respectively.

Figure 4.16 suggests different modes of propagation before and after WBM invasion with a monopole source at the first measurement location. Similar to the third

rock type, the Stoneley wave after WBM invasion becomes less dispersive than before invasion. Moreover, the Stoneley mode in this rock type becomes more dispersive than in the previous rock types because the formation has become slower. The compressional wave after WBM invasion becomes slightly dispersive. Furthermore, the compressional wave spans over a larger frequency range than before.

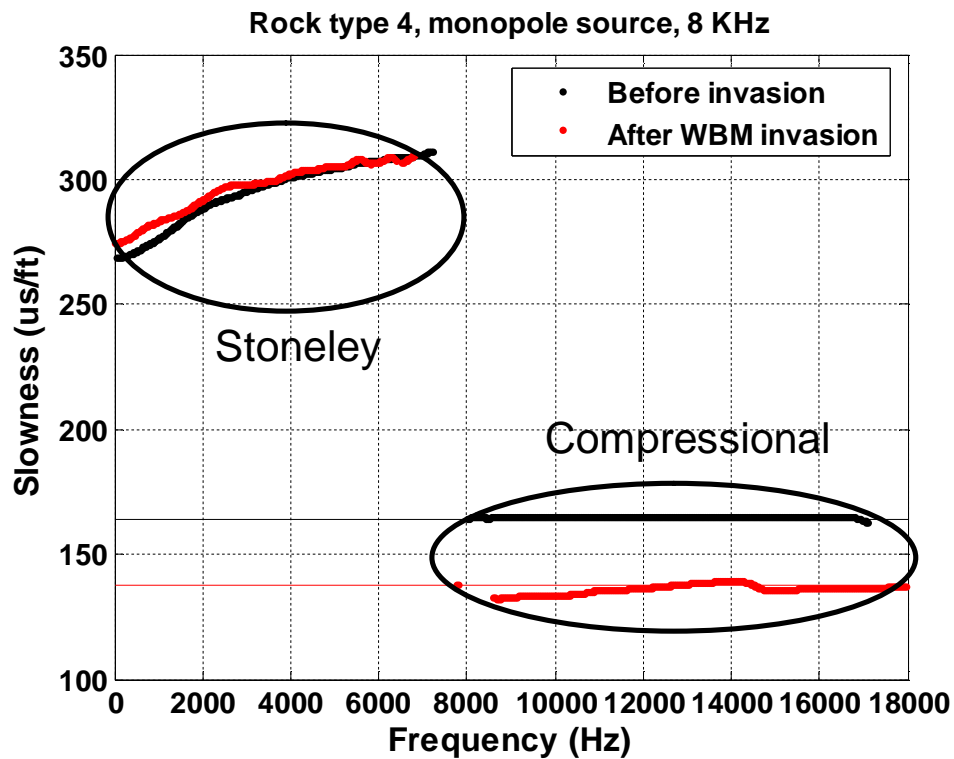


Figure 4.16: Frequency dispersion results for the fourth rock type with a monopole source at the first measurement location. Red and black curves identify results for after and before WBM invasion, respectively. Black and red lines identify the formation compressional-wave slowness before and after invasion, respectively.

Second measurement location

Figure 4.17 shows flexural-wave frequency dispersion results before and after WBM invasion at the second measurement location. Similar to the previous rock types, the zero-

frequency asymptote shifts to higher values after invasion due to gravity segregation and water accumulation at the bottom of the capillary transition zone, resulting from the increase of permeability and porosity. Moreover, the compressional mode is excited after WBM invasion and exhibits a slowness equal to the compressional slowness of the water zone.

Figure 4.18 shows different propagation modes at the second measurement location with a monopole source. Similar to the third rock type, I observe mode splitting in this rock type. The compressional wave before invasion consists of two parts: the first part, which occurs at a lower frequency range, exhibits slowness values between those of the compressional slowness of the water-filled zone (blue line) and the compressional slowness of the formation at the location of the top receiver (black line). This behavior is expected because the receiver array straddles over the formation inside and outside the water zone. The second part, however, exhibits exactly the same slowness as the compressional slowness of the water zone. The compressional slowness of the formation after WBM invasion exhibits values between those of the compressional slowness of the water zone and the compressional slowness of the formation at the location of the top receiver (red line). At higher frequencies, the red curve approaches the compressional slowness of the water zone.

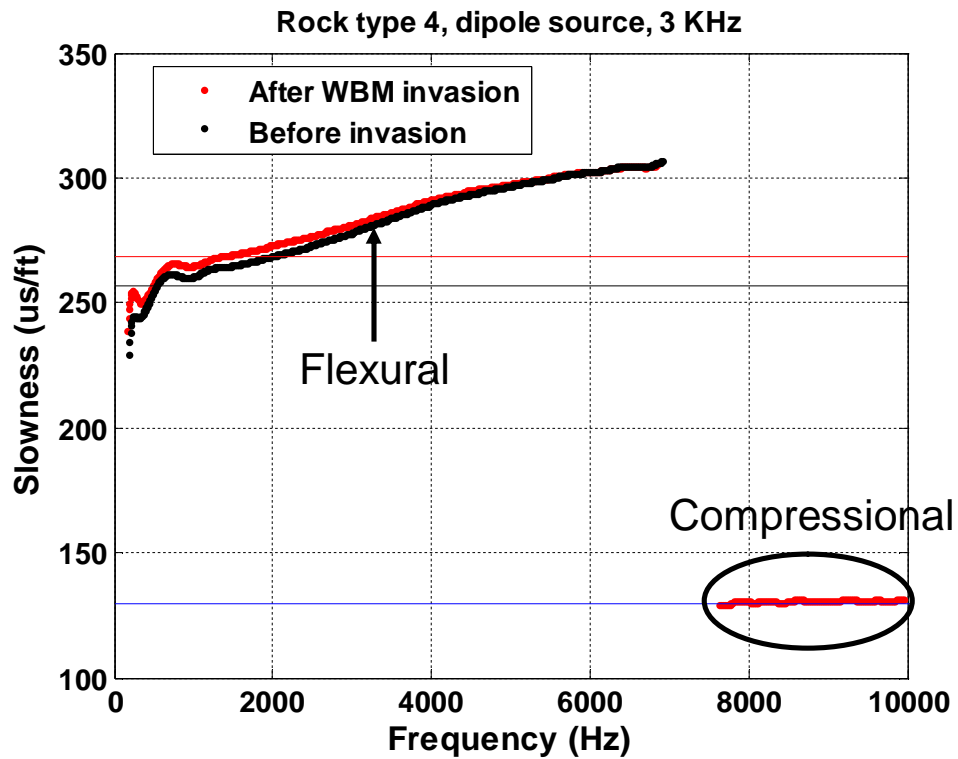


Figure 4.17: Frequency dispersion results for the fourth rock type with a dipole source at the second measurement location. Red and black curves identify results for after and before WBM invasion, respectively. Compressional wave after WBM invasion is circled in black. The blue line identifies the water-filled rock compressional slowness. Black and red lines identify the formation shear slowness at the top receiver before and after invasion, respectively.

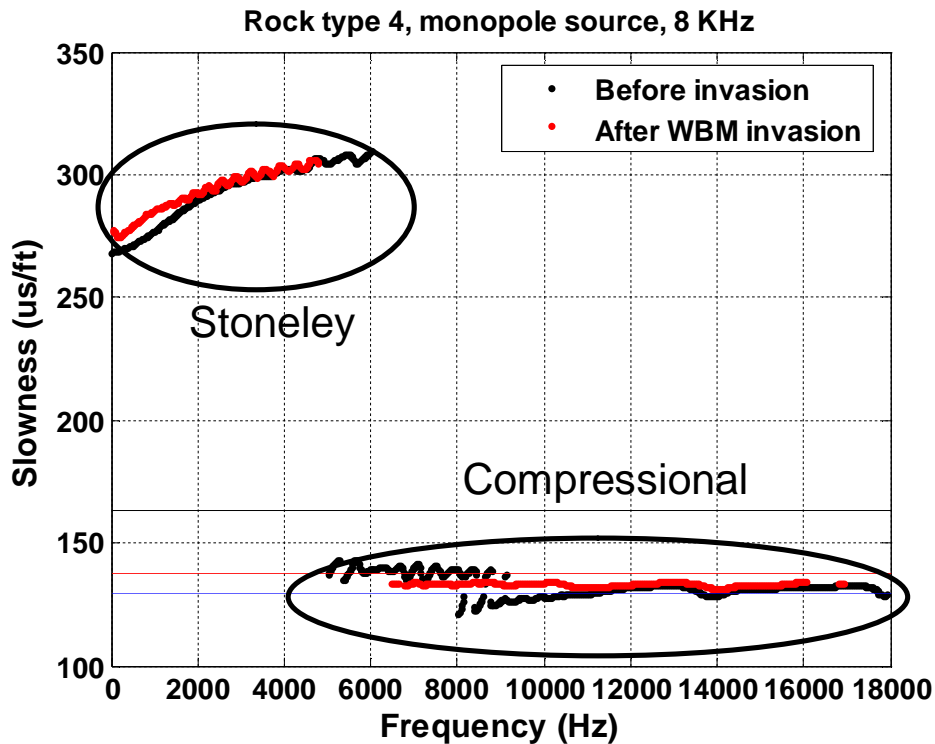


Figure 4.18: Frequency dispersion results for the fourth rock type with a monopole source at the second measurement location. Red and black curves identify results for after and before WBM invasion, respectively. Stoneley and compressional modes are circled separately. Black and red lines identify the formation compressional-wave slowness before and after invasion at the location of the top receiver, respectively. The blue line identifies the water-filled rock compressional slowness.

4.2 OIL-BASE MUD-FILTRATE (OBM) INVASION

In this section, I compare simulation results for both before and after WBM and OBM invasion at different measurement locations with monopole and dipole sources.

First measurement location

Figures 4.19 through 4.22 show flexural-wave dispersion before and after WBM and OBM invasion at the first measurement location. The curves corresponding to post-

OBM invasion stage tend to remain closer to before-invasion curves, especially at low frequencies. At higher frequencies, they tend to separate from those of before invasion, especially at central frequencies where energy is at the highest value. The reason for this behavior is the smaller radius of OBM invasion in comparison to WBM invasion.

However, Figure 4.19 suggests that there are negligible differences between the before-invasion dispersion curve and post-invasion dispersion curves for the first rock type.

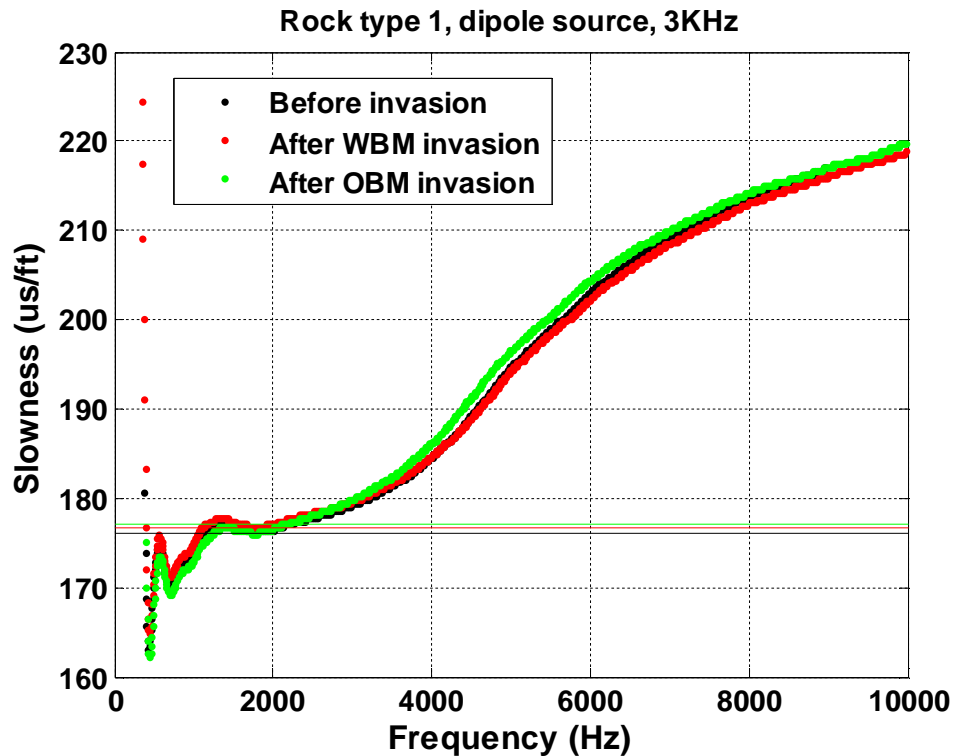


Figure 4.19: Frequency dispersion results for the first rock type with a dipole source at the first measurement location. Black, red, and green curves identify results for before invasion, after WBM invasion, and after OBM invasion, respectively. Black, red, and green lines identify the formation shear slowness before invasion, after WBM invasion, and after OBM invasion, respectively.

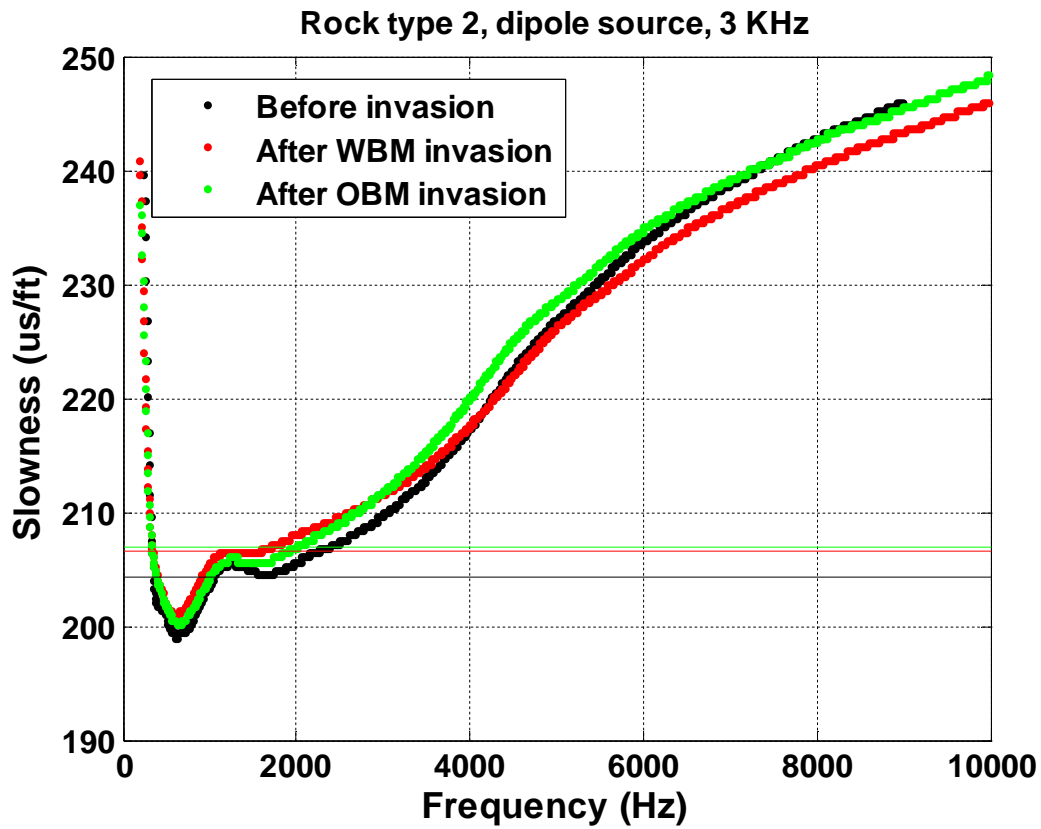


Figure 4.20: Frequency dispersion results for the second rock type with a dipole source at the first measurement location. Black, red, and green curves identify results for before invasion, after WBM invasion, and after OBM invasion, respectively. Black, red, and green lines identify the formation shear slowness before invasion, after WBM invasion, and after OBM invasion, respectively.

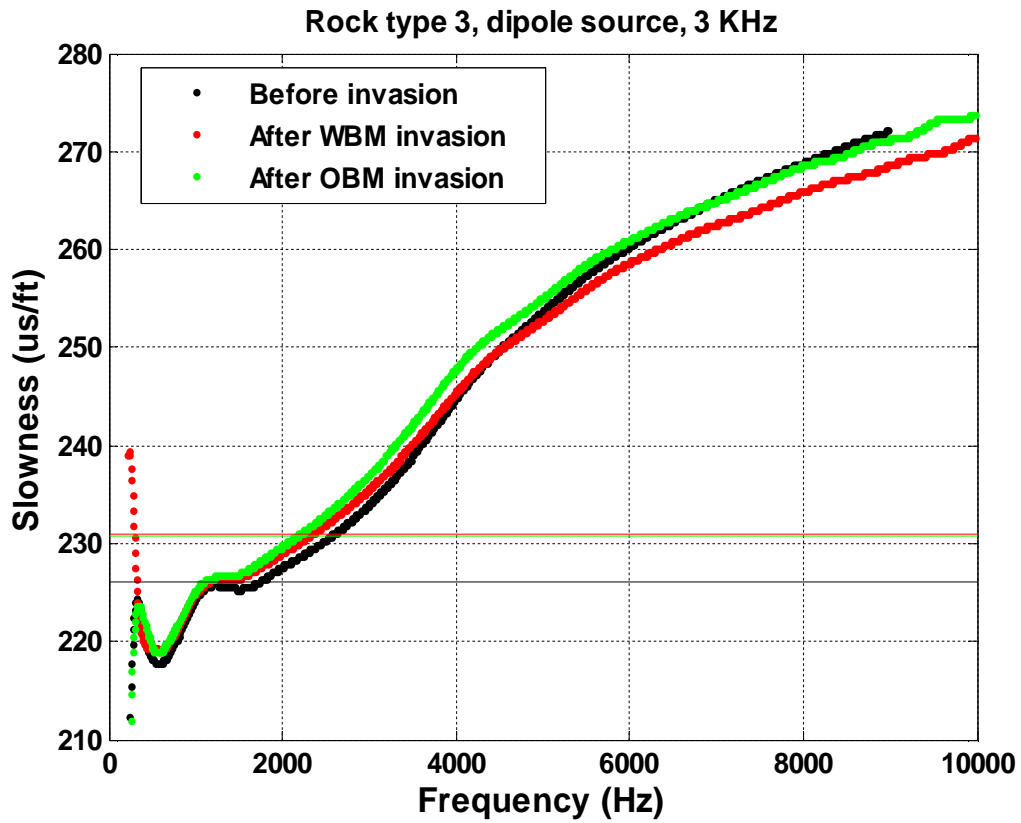


Figure 4.21: Frequency dispersion results for the third rock type with a dipole source at the first measurement location. Black, red, and green curves identify results for before invasion, after WBM invasion, and after OBM invasion, respectively. Black, red, and green lines identify the formation shear slowness before invasion, after WBM invasion, and after OBM invasion, respectively.

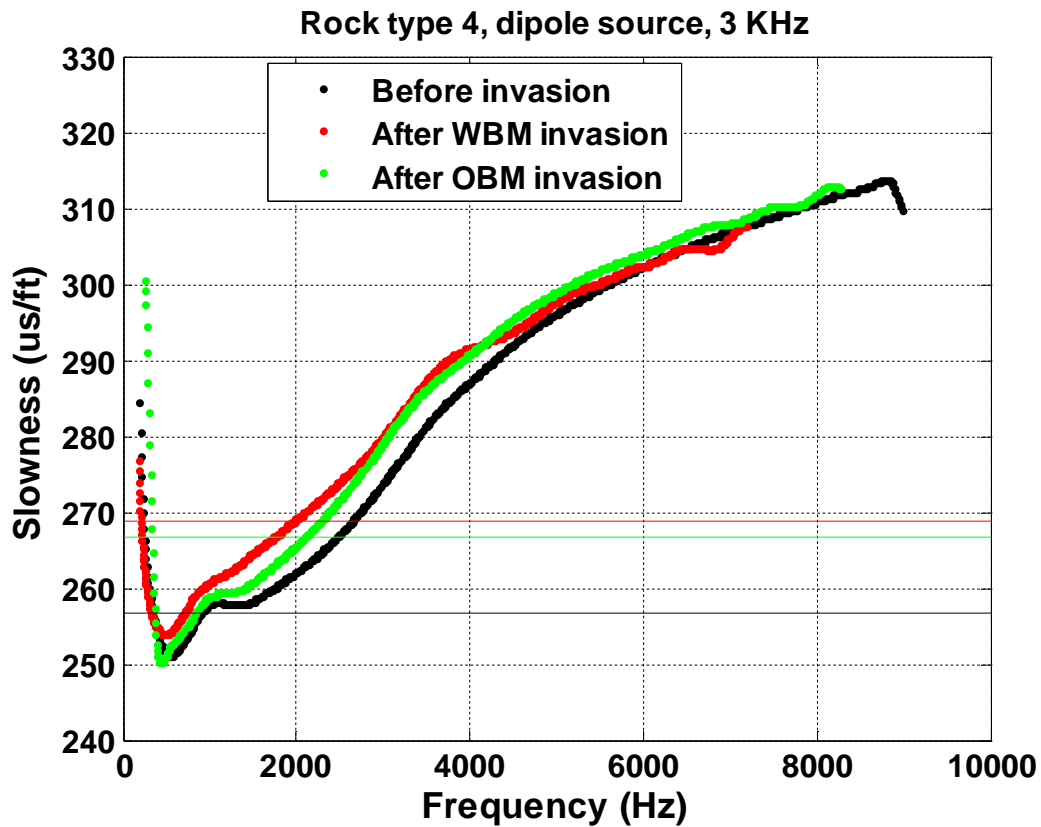


Figure 4.22: Frequency dispersion results for the fourth rock type with a dipole source at the first measurement location. Black, red, and green curves identify results for before invasion, after WBM invasion, and after OBM invasion, respectively. Black, red, and green lines identify the formation shear slowness before invasion, after WBM invasion, and after OBM invasion, respectively.

Figures 4.23 through 4.26 illustrate the monopole frequency dispersion results at the first measurement location for the four assumed rock types. As stated earlier, there are negligible differences between dispersions calculated before invasion and after both WBM and OBM invasion in the first rock type due to the small range of variation of fluid saturation. Figure 4.24 shows the effect of invasion on different modes of propagation for the second rock type. The figure suggests that pseudo-Rayleigh waves arise both before invasion and after OBM invasion, while they do not arise after WBM invasion. Moreover, WBM invasion impacts the compressional wave more than OBM invasion. The compressional wave after WBM invasion spans over a larger range of frequencies than after OBM invasion. Figures 4.24, 4.25, and 4.26 indicate that the Stoneley waves after invasion become less dispersive than before invasion in rock types 2, 3, and 4. However, Figure 4.23 indicates that the Stoneley wave becomes slightly more dispersive after invasion in the first rock type. In all rock types, the Stoneley wave after WBM invasion becomes less dispersive than after OBM invasion. I therefore conclude that the Stoneley wave becomes more dispersive as porosity and permeability increase.

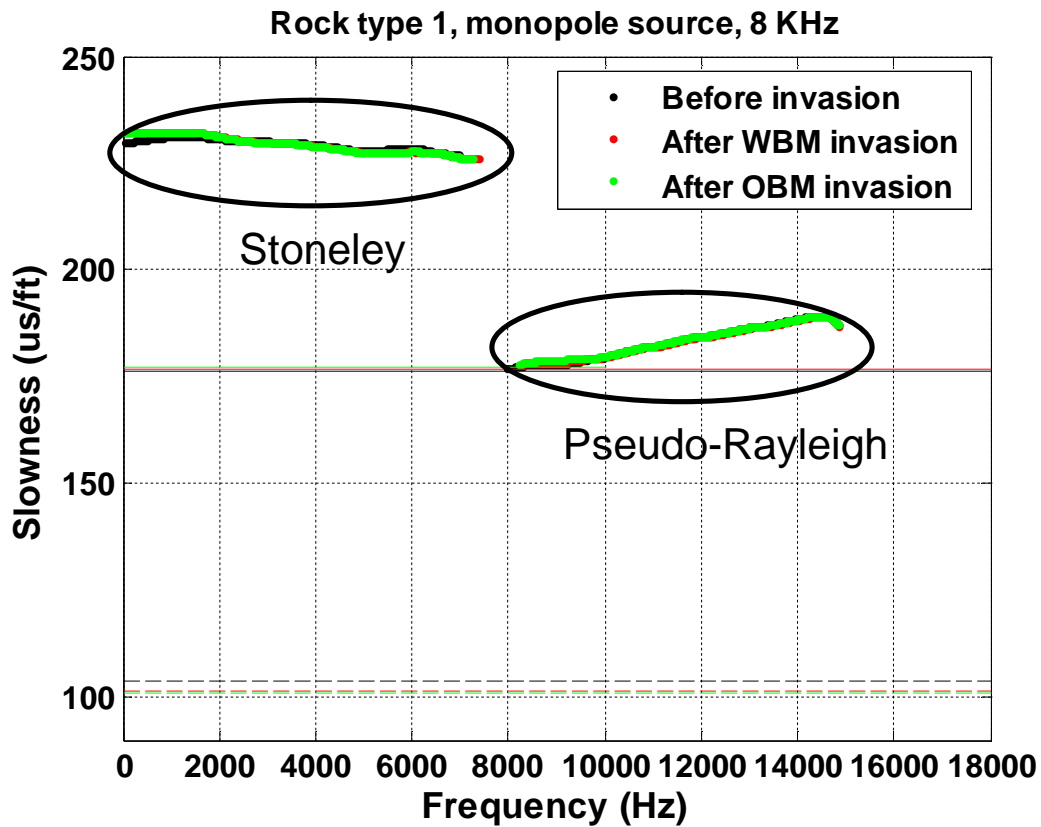


Figure 4.23: Frequency dispersion results for the first rock type with a monopole source at the first measurement location. Green, red, and black curves identify results for after OBM invasion, after WBM invasion, and before invasion, respectively. Stoneley and pseudo-Rayleigh modes are circled separately. The green, red, and black dashed lines represent compressional-wave slowness after OBM invasion, after WBM invasion, and before invasion, respectively. Solid green, red, and black lines identify the formation shear-wave slowness after OBM invasion, after WBM invasion, and before invasion, respectively.

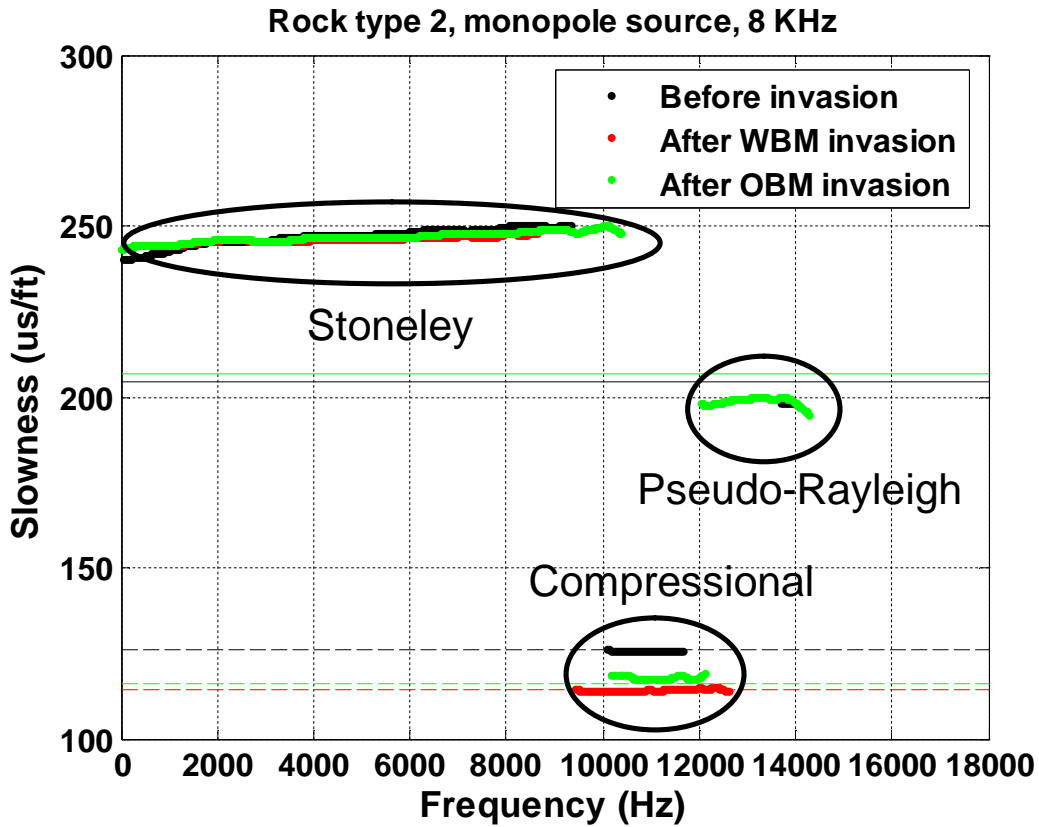


Figure 4.24: Frequency dispersion results for the second rock type with a monopole source at the first measurement location. Green, red, and black curves identify results for after OBM invasion, after WBM invasion, and before invasion, respectively. Stoneley, compressional, and pseudo-Rayleigh modes are circled separately. The green, red, and black dashed lines represent compressional-wave slowness after OBM invasion, after WBM invasion, and before invasion, respectively. Solid green and black lines identify the formation shear-wave slowness after OBM invasion and before invasion, respectively.

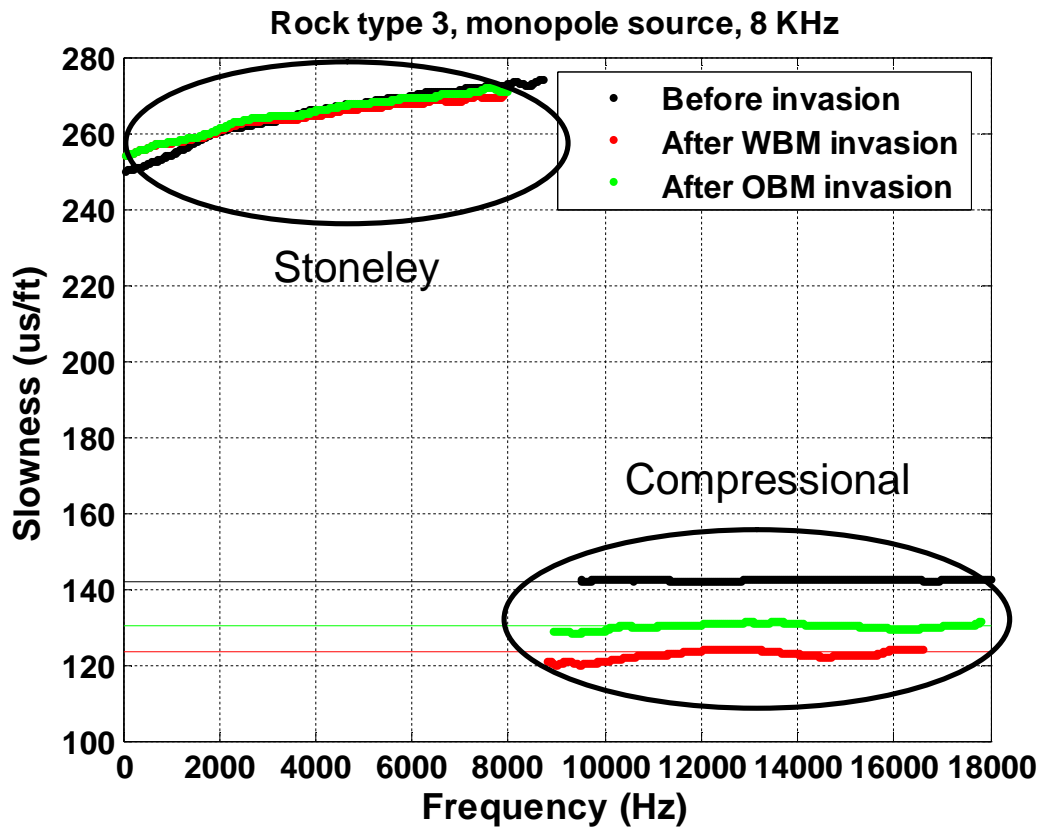


Figure 4.25: Frequency dispersion results for the third rock type with a monopole source at the first measurement location. Green, red, and black curves identify results for after OBM invasion, after WBM invasion, and before invasion, respectively. Stoneley and compressional modes are circled separately. Solid green, red, and black lines identify the formation compressional-wave slowness after OBM invasion, after WBM invasion, and before invasion, respectively.

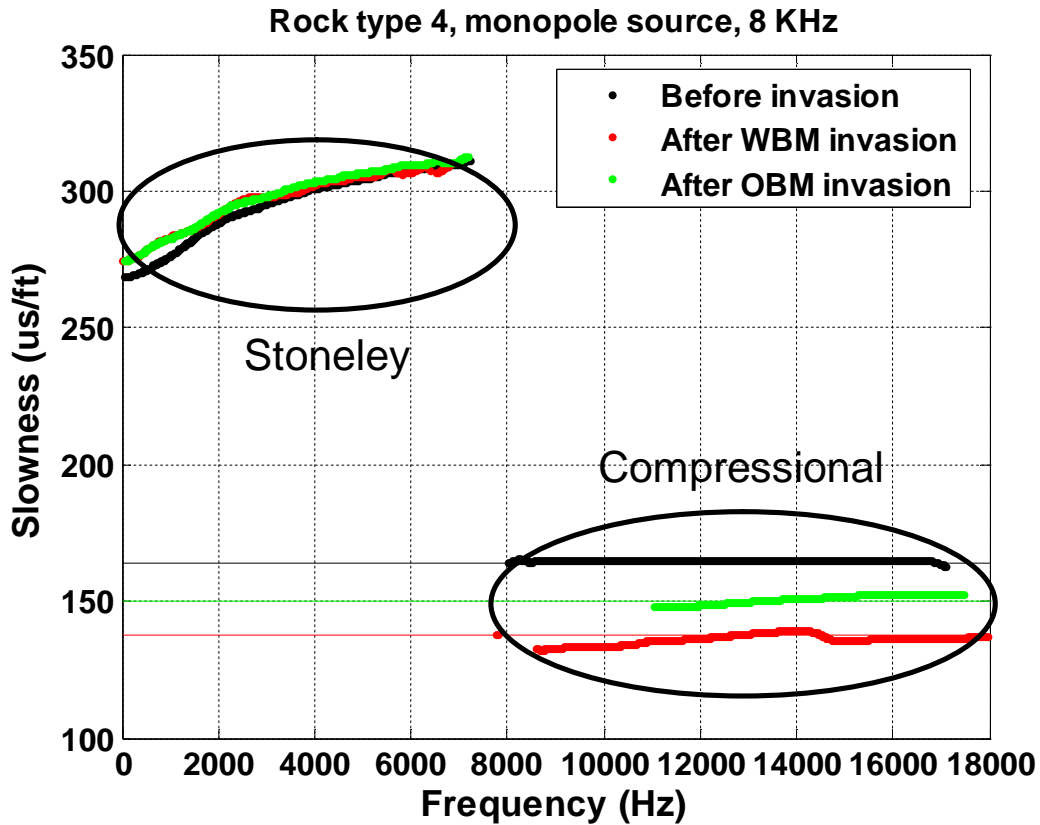


Figure 4.26: Frequency dispersion results for the fourth rock type with a monopole source at the first measurement location. Green, red, and black curves identify results for after OBM invasion, after WBM invasion, and before invasion, respectively. Stoneley and compressional modes are circled separately. Solid green, red, and black lines identify the formation compressional-wave slowness after OBM invasion, after WBM invasion, and before invasion, respectively.

Second measurement location

Figures 4.27 through 4.30 illustrate dipole frequency dispersion results for different rock types for the cases of before invasion, after WBM invasion, and after OBM invasion. Figure 4.27 shows simulation results for the first rock type. As noted before, due to the narrow range of fluid saturation and low porosity, I observe

negligible differences between dispersion curves for before and after invasion. For the remainder of the simulated cases, the separation between after-invasion and before-invasion dispersion curves increases with increasing frequency. However, OBM has a smaller effect on frequency dispersion curves due to the shorter radius of invasion. For the fourth rock type, Figure 4.30 shows a leaky-P mode, especially after OBM invasion.

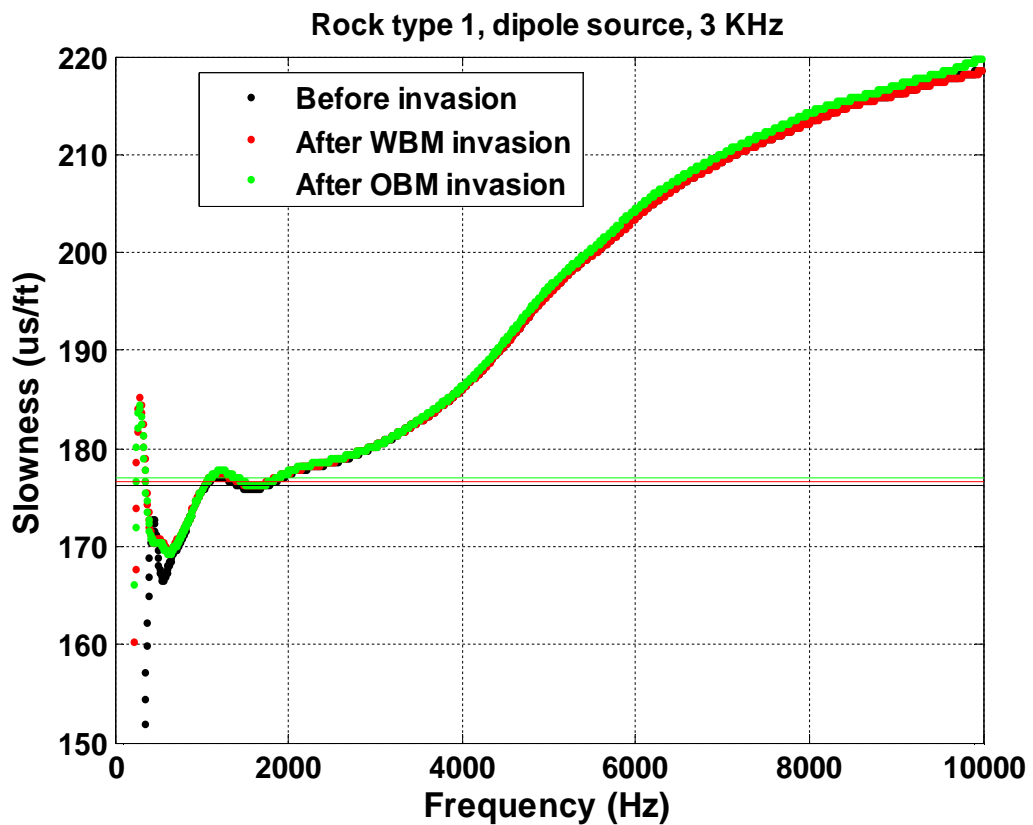


Figure 4.27: Frequency dispersion results for the first rock type with a dipole source at the second measurement location. Black, red, and green curves identify results for before invasion, after WBM invasion, and after OBM invasion, respectively. Black, red, and green lines identify the formation shear slowness at the location of the top receiver before invasion, after WBM invasion, and after OBM invasion, respectively.

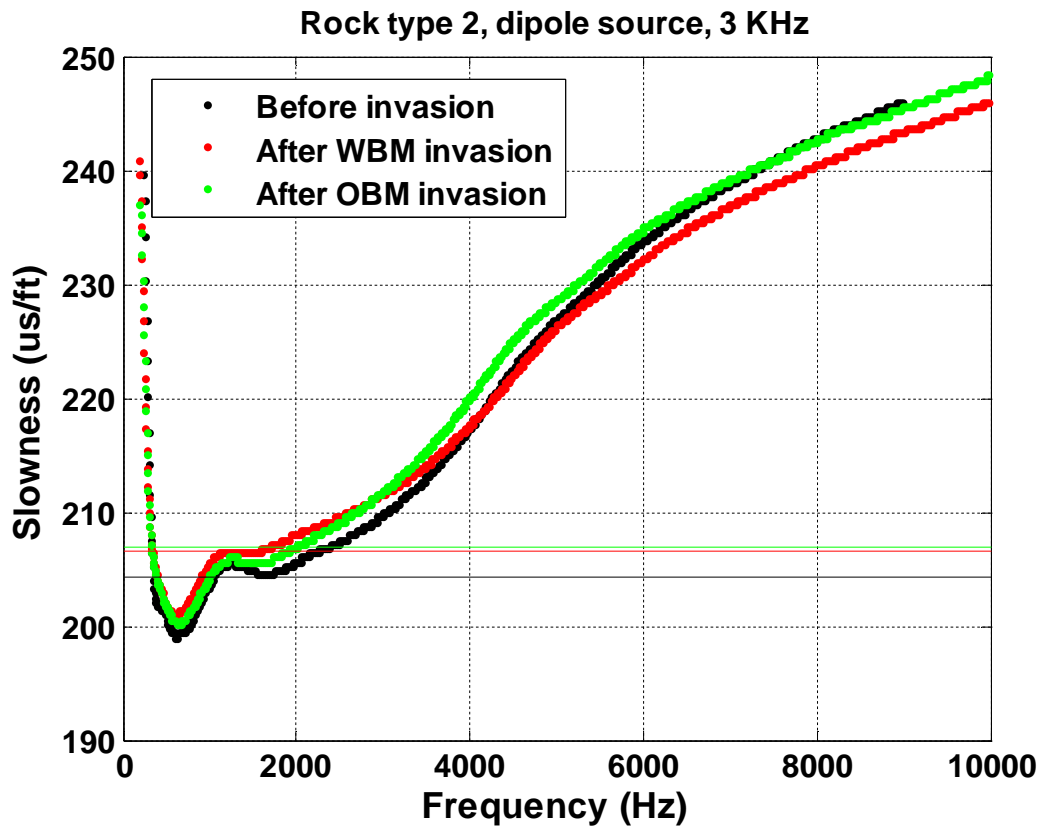


Figure 4.28: Frequency dispersion results for the second rock type with a dipole source at the second measurement location. Black, red, and green curves identify results for before invasion, after WBM invasion, and after OBM invasion, respectively. Black, red, and green lines identify the formation shear slowness at the location of the top receiver before invasion, after WBM invasion, and after OBM invasion, respectively.

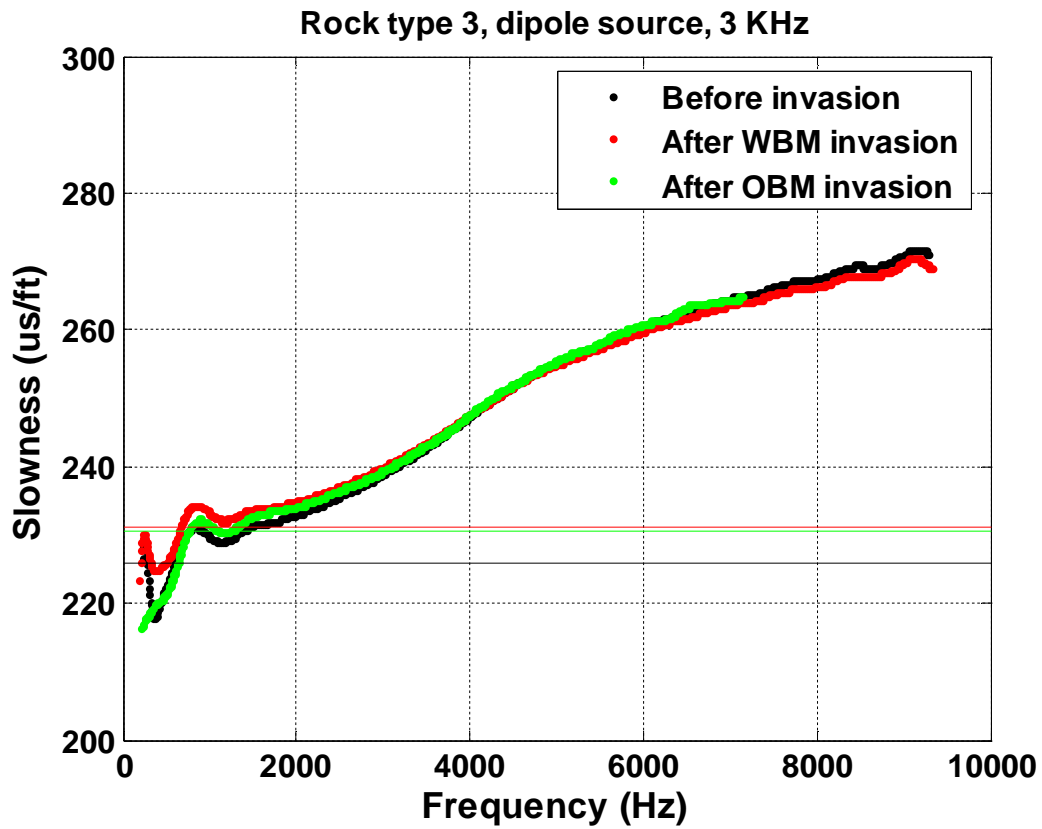


Figure 4.29: Frequency dispersion results for the third rock type with a dipole source at the second measurement location. Black, red, and green curves identify results for before invasion, after WBM invasion, and after OBM invasion, respectively. Black, red, and green lines identify the formation shear slowness at the location of the top receiver before invasion, after WBM invasion, and after OBM invasion, respectively.

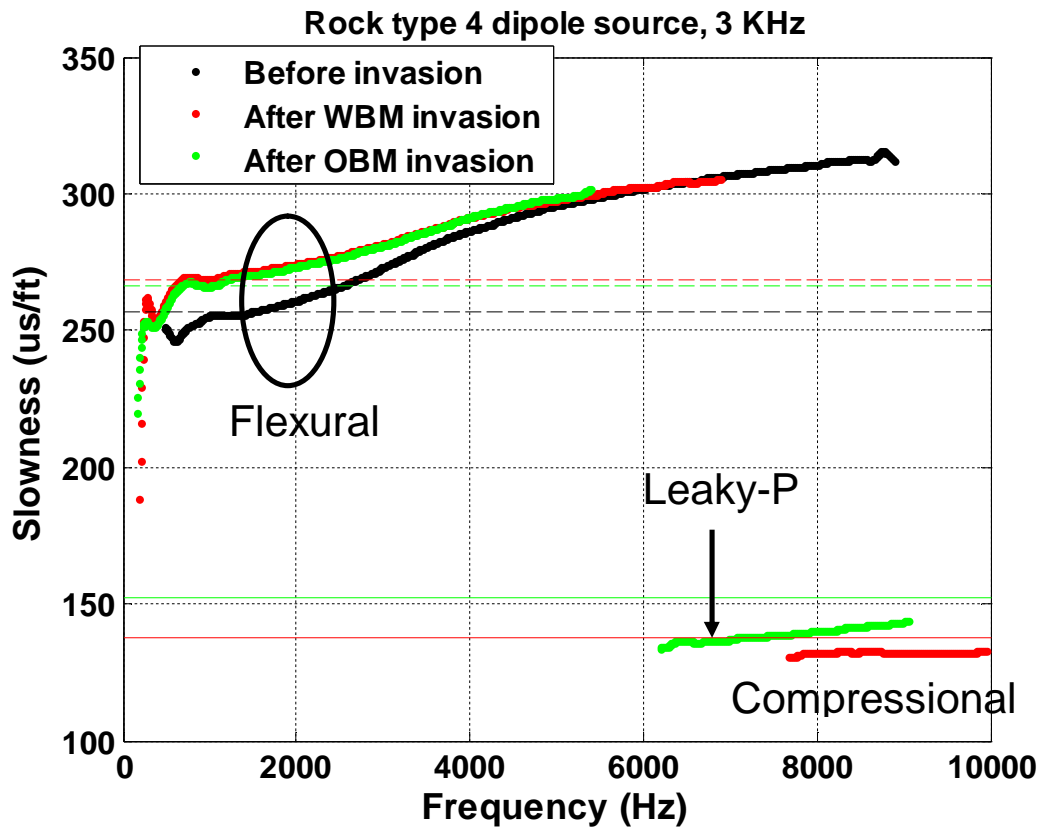


Figure 4.30: Frequency dispersion results for the fourth rock type with a dipole source at the second measurement location. Black, red, and green curves identify results for before invasion, after WBM invasion, and after OBM invasion, respectively. Dashed green, red, and black lines represent formation shear slowness at the location of the top receiver after OBM invasion, after WBM invasion, and before invasion, respectively. Solid red and green lines identify the formation compressional slowness at the location of the top receiver after WBM and OBM invasion, respectively.

Figures 4.31 through 4.34 illustrate modes of propagation at the second measurement location for the four assumed rock types, all with a monopole source. The figures show that the Stoneley wave exhibits relatively higher sensitivity to invasion at low frequencies than at high frequencies in all of the assumed rock types.

The figures also indicate that the Stoneley wave becomes less dispersive after invasion than before invasion. Black, green, and red horizontal lines identify the formation shear slowness at the borehole interface at the location of the top receiver before invasion, after OBM invasion, and after WBM invasion, respectively.

As indicated earlier, the first rock type is not sensitive to invasion, and I observe Stoneley and pseudo-Rayleigh modes in Figure 4.31. Figure 4.32 indicates that the compressional wave exhibits marginal sensitivity to invasion at the second measurement location for the second rock type. Figures 4.33 and 4.34 suggest that the compressional wave corresponding to before-invasion stage splits into two separate parts in the third and the fourth rock types. The first part, which takes place at a lower frequency range, exhibits higher slownesses and is therefore closer to the formation compressional slowness at the top receiver. The second part, which takes place at a higher frequency range, is very close to the formation compressional slowness in the water zone and becomes slightly dispersive. For the third rock type, the compressional wave after OBM invasion is closer to the first part. After invasion, no mode separation is observed because invasion distorts the capillary transition zone and causes the formation above the gas-water-contact to exhibit null vertical variations. However, Figure 4.34 suggests that in the fourth rock type, the dispersion curve after OBM invasion splits into two parts, and I observe the highest discrepancy between before-invasion and after-invasion dispersion curves. The reason for this behavior is the highest porosity (0.25) and the largest range of water saturation, from 21% to 85%, both of which result in the greatest volumetric fluid exchange. These

factors result in the highest relative change of fluid saturation originating from OBM and WBM invasion.

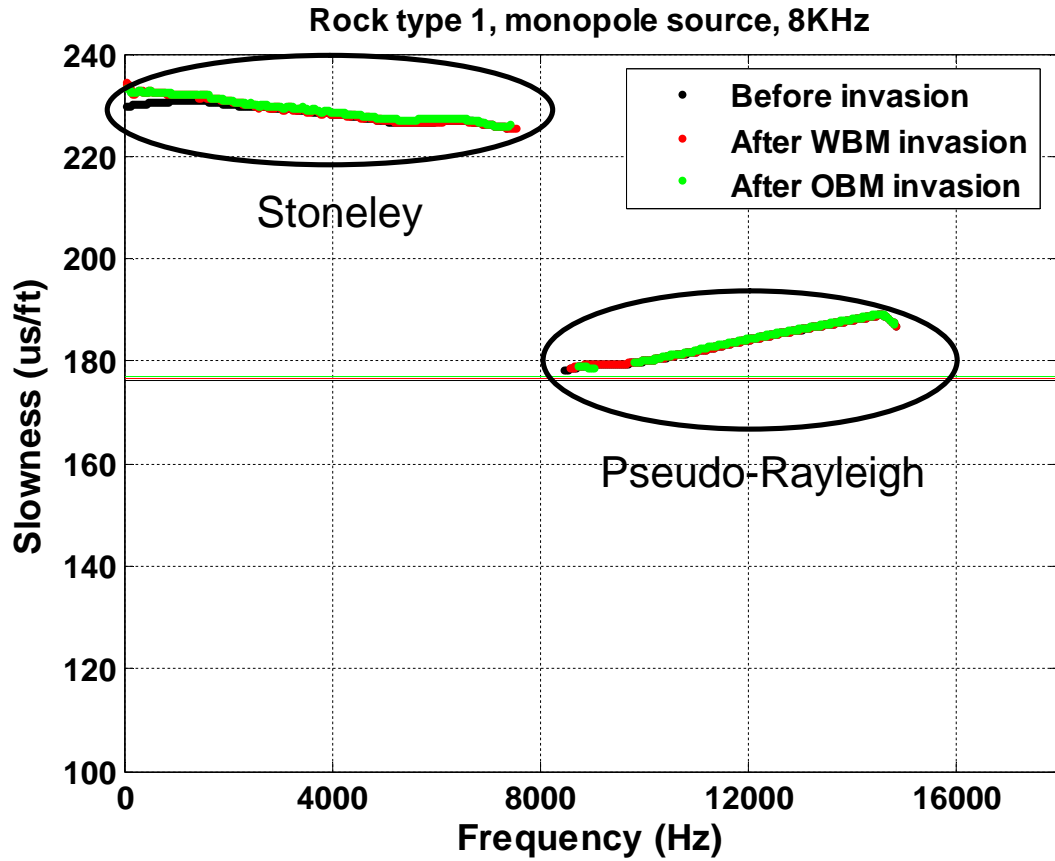


Figure 4.31: Frequency dispersion results for the first rock type with a monopole source at the second measurement location. Green, red, and black curves identify results for after OBM invasion, after WBM invasion, and before invasion, respectively. Stoneley and pseudo-Rayleigh modes are circled separately. Solid green, red, and black lines identify the formation shear-wave slowness after OBM invasion, after WBM invasion, and before invasion, respectively.

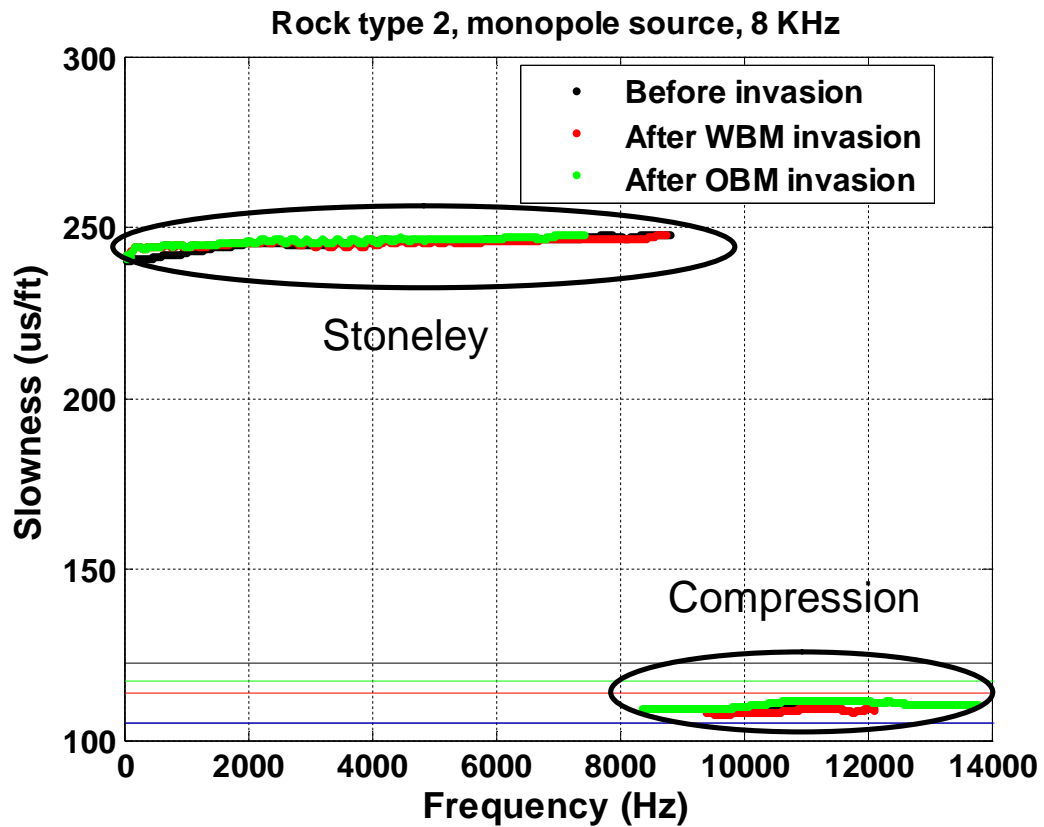


Figure 4.32: Frequency dispersion results for the second rock type with a monopole source at the second measurement location. Green, red, and black curves identify results for after OBM invasion, after WBM invasion, and before invasion, respectively. Stoneley and compressional modes are circled separately. Solid green, red, and black lines identify the formation compressional-wave slowness after OBM invasion, after WBM invasion, and before invasion, respectively. The blue line identifies the compressional slowness of the water zone.

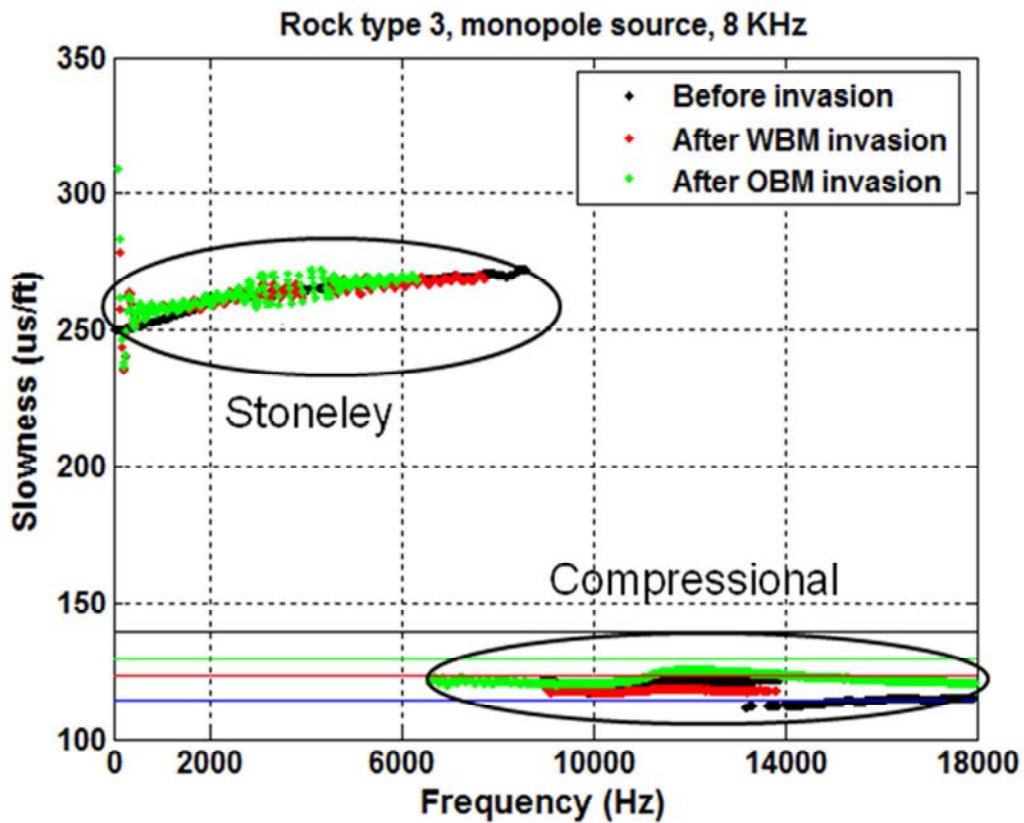


Figure 4.33: Frequency dispersion results for the third rock type with a monopole source at the second measurement location. Green, red, and black curves identify results for after OBM invasion, after WBM invasion, and before invasion, respectively. Stoneley and compressional modes are circled separately. Solid green, red, and black lines identify the formation compressional-wave slowness after OBM invasion, after WBM invasion, and before invasion, respectively. The blue line identifies the compressional slowness of the water zone.

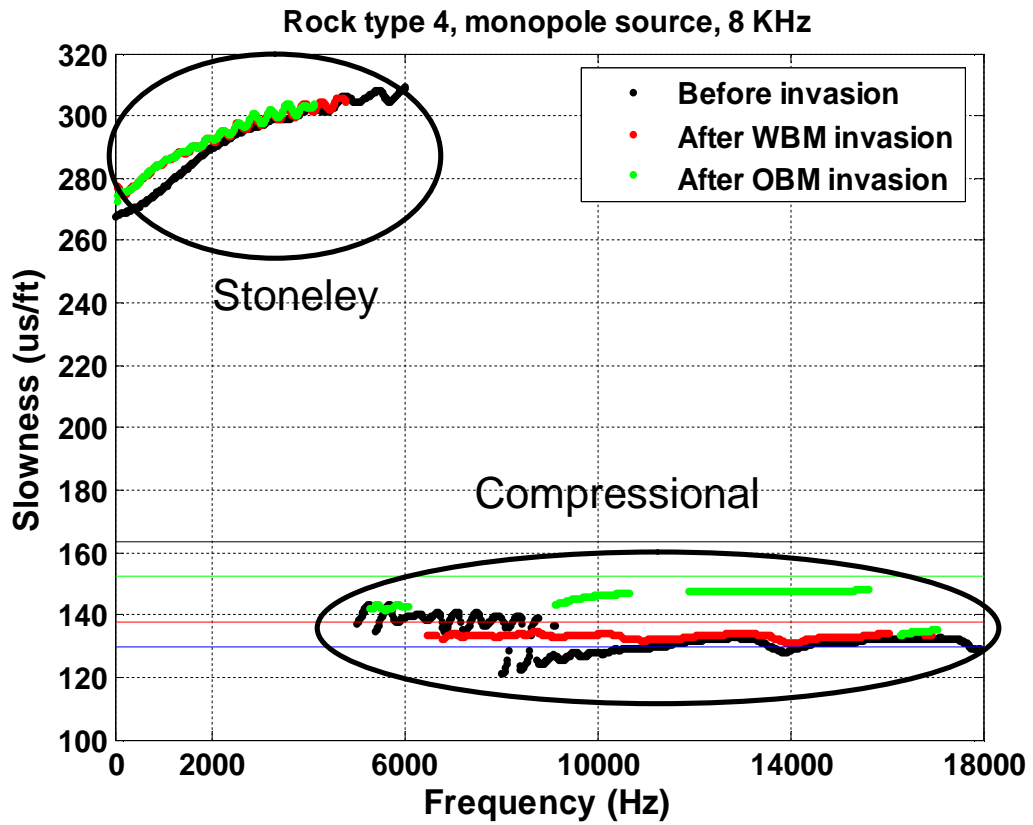


Figure 4.34: Frequency dispersion results for the fourth rock type with a monopole source at the second measurement location. Green, red, and black curves identify results for after OBM invasion, after WBM invasion, and before invasion, respectively. Stoneley and compressional modes are circled separately. Solid green, red, and black lines identify the formation compressional-wave slowness after OBM invasion, after WBM invasion, and before invasion, respectively. The blue line identifies the compressional slowness of the water zone.

CHAPTER 5

CONCLUSIONS

In this chapter, I discuss the effects of (a) mud-filtrate invasion, (b) variations of petrophysical properties of the rock, and (c) measurement location along the capillary transition zone on borehole sonic measurements. I also outline practical conclusions from the research.

5.1 EFFECT OF MUD-FILTRATE INVASION

Mud-filtrate invasion impacts sonic measurements for all rock types except for the case of the rock with minimum porosity (rock type 1). Sonic measurements acquired in low-porosity formations exhibit low sensitivity to mud-filtrate invasion. These formations are commonly known to have non-uniform pore-size distributions which result in high residual fluid saturations. Therefore, the volume of the fluid to be substituted is small in this type of rock. In other rock types, I observe marginal discrepancy in the flexural dispersion curves at low frequencies between both before and after invasion at the first measurement location, whereas the discrepancy increases as frequency increases. Tables 5.1 and 5.2 show the effect of WBM and OBM invasion on flexural waves at the first measurement location. The tables compare the separation between dispersion curves before and after invasion at two frequencies. For WBM invasion, the maximum difference between before and after invasion occurs at 8 KHz whereas the maximum difference for OBM invasion occurs around the central frequency

(3 KHz for the dipole source). Mud-filtrate invasion also affects the Stoneley wave. Tables 5.3 and 5.4 show the slowness range of the Stoneley wave over frequencies ranging from 10 Hz to 5 KHz after WBM and OBM invasion, respectively. The Stoneley wave becomes less dispersive after invasion in rock types 2, 3, and 4. However, the Stoneley wave becomes slightly more dispersive after invasion in the first rock type. In addition, the Stoneley wave exhibits less dispersivity after WBM invasion than after OBM invasion in rock types 2, 3, and 4. Mode splitting, which occurs at the second measurement location before invasion, vanishes after invasion. In the simulated cases, OBM has a shallower radius of invasion. Therefore, frequency dispersion results are less affected by OBM invasion than by WBM invasion.

Table 5.1: Effect of WBM invasion on the flexural wave at two different frequencies for the four assumed rock types.

| | Rock 1 | Rock 2 | Rock 3 | Rock 4 |
|---|---------------|---------------|---------------|---------------|
| Difference between before and after WBM invasion at 1.5 KHz ($\mu\text{s}/\text{ft}$) | 0.5 | 0.8 | 1.2 | 2.2 |
| Difference between before and after WBM invasion at 8 KHz ($\mu\text{s}/\text{ft}$) | 1.0 | 2.5 | 3.0 | 5.0 |

Table 5.2: Effect of OBM invasion on the flexural wave at two different frequencies for the four assumed rock types.

| | Rock 1 | Rock 2 | Rock 3 | Rock 4 |
|---|---------------|---------------|---------------|---------------|
| Difference between before and after OBM invasion at 1.5 KHz ($\mu\text{s}/\text{ft}$) | 0.4 | 0.5 | 1.2 | 2.0 |
| Difference between before and after OBM invasion at 8 KHz ($\mu\text{s}/\text{ft}$) | 0.8 | 2.0 | 3.0 | 4.5 |

Table 5.3: Effect of WBM and OBM invasion on the Stoneley-wave dispersion for the four assumed rock types.

| | Rock 1 | Rock 2 | Rock 3 | Rock 4 |
|---|---------------|---------------|---------------|---------------|
| Stoneley-wave slowness range before invasion ($\mu\text{s}/\text{ft}$) | 3.3 | 10 | 23.7 | 42.7 |
| Stoneley-wave slowness range after WBM invasion ($\mu\text{s}/\text{ft}$) | 6.3 | 4.3 | 15.7 | 36.0 |
| Stoneley-wave slowness range after OBM invasion ($\mu\text{s}/\text{ft}$) | 6.3 | 6.6 | 17.6 | 38.4 |

5.2 EFFECT OF PETROPHYSICAL PROPERTIES

Numerical simulations undertaken in this report suggest that variations of petrophysical properties of the rock affect borehole sonic measurements. The petrophysical properties include porosity, permeability, capillary pressure, and relative permeability. As the porosity of the rock increases, the Stoneley wave becomes more dispersive. Table 5.3 shows that the slowness of the Stoneley mode before invasion in the first rock type (minimum porosity) varies by 3.3 $\mu\text{s}/\text{ft}$, whereas it varies by 42.7 $\mu\text{s}/\text{ft}$ in the fourth rock type (maximum porosity).

As the porosity increases, the formation becomes softer, and consequently, the compressional mode appears in a wider range of frequencies. Table 5.4 shows the frequency range of the compressional mode for various rock types before invasion. For the first rock type, I observe no compressional mode in the frequency dispersion results. Instead, I observe the pseudo-Rayleigh mode, which asymptotes to the shear slowness of the formation with a monopole source. However, the compressional mode spans over the frequency range of 8 KHz to 17 KHz for the fourth rock type.

Table 5.4: Frequency range of the compressional wave before invasion for different rock types.

| | Rock 1 | Rock 2 | Rock 3 | Rock 4 |
|---|---------------|---------------|---------------|---------------|
| Compressional-wave frequency range before invasion (Hz) | ----- | 1460 | 8353 | 9070 |

5.3 EFFECT OF MEASUREMENT LOCATION

Except for the rock type with the lowest porosity (0.1), measurement location along the capillary transition zone affects borehole acoustic measurements. For flexural waves, the low-frequency asymptote is shifted after invasion at the second measurement location (where half of the receivers are inside the water zone and half of them are outside the water zone), whereas for measurements at the top segment of the capillary transition zone, flexural waves do not differ at low frequencies before and after invasion. Table 5.5 shows the shifts in the flexural-wave low-frequency asymptote for different rock types. The reason behind this effect is gravity segregation at the second measurement location. With increasing permeability, water has a higher tendency to segregate in the formation. Thus, at the second measurement location, the tool is mainly affected by mud filtrate and does not detect original formation fluids, even at low frequencies where we have a deeper radius of investigation. For the monopole source, I observe apparent mode splitting at the second measurement location. Frequency dispersion results show that the compressional wave splits into two separate modes for the third and the fourth rock types, one mode takes values close to the compressional

slowness of the completely water-saturated zone, and the other mode approximates the compressional slowness of the formation just above the gas-water contact.

Table 5.5: Shifts of flexural-wave low-frequency asymptote for the assumed rock types; the effect of measurement location on the flexural wave.

| | Rock 1 | Rock 2 | Rock 3 | Rock 4 |
|--|---------------|---------------|---------------|---------------|
| Low-frequency asymptote shift after WBM invasion ($\mu\text{s}/\text{ft}$) | 0.4 | 1.5 | 3.1 | 14.7 |
| Low-frequency asymptote shift after OBM invasion ($\mu\text{s}/\text{ft}$) | 0.4 | 1.5 | 1.8 | 13.2 |

This study has found that mud-filtrate invasion, petrophysical properties of the rock, and measurement location along the capillary transition zone can each have a drastic effect on borehole sonic measurements and should be considered in the interpretation of sonic logs, especially in complex systems that include both vertical and radial variations in fluid saturation.

NOMENCLATURE

| | |
|-------------|---|
| P_c | : Capillary pressure, [psi] |
| P_c^0 | : Coefficient for capillary pressure, [psi.md ^{1/2}] |
| ϕ | : Porosity, [fraction] |
| K | : Permeability, [md] |
| S_N | : Normalized wetting phase saturation, [fraction] |
| e_p | : Pore-size distribution exponent, [] |
| S_w | : Wetting phase saturation, [fraction] |
| S_{wr} | : Residual wetting phase saturation, [fraction] |
| S_{nwr} | : Residual non-wetting phase saturation, [fraction] |
| k_{rw} | : Wetting phase relative permeability, [fraction] |
| k_{rw}^0 | : Wetting phase relative permeability end point, [fraction] |
| e_w | : Empirical exponent for the wetting phase, [] |
| k_{mww} | : Non-wetting phase relative permeability, [fraction] |
| k_{mww}^0 | : Non-wetting phase relative permeability end point, [fraction] |
| e_{nw} | : Empirical exponent for the non-wetting phase, [] |
| $S_{w,irr}$ | : Irreducible water saturation, [fraction] |
| k_{mc} | : Mudcake permeability, [md] |
| k_{mc0} | : Mudcake reference permeability, [md] |

| | |
|--------------|--|
| P_{mc} | : Mudcake pressure differential, [psi/psi] |
| ν | : Compressibility exponent, [] |
| ϕ_{mc} | : Mudcake porosity, [fraction] |
| ϕ_{mc0} | : Mudcake reference porosity, [fraction] |
| δ | : Multiplier for the porosity exponent, [] |
| r_{mc} | : Mudcake thickness, [in] |
| dr_{mc} | : Differential mudcake thickness, [in] |
| f_s | : Mud solid fraction, [fraction] |
| μ_f | : Mud-filtrate viscosity, [cp] |
| K_{satP} | : Effective bulk modulus, [Pa] |
| μ | : Dry shear modulus, [Pa] |
| S | : Volumetric fraction of the saturated patch, [fraction] |
| K_0 | : Liquid-saturated rock bulk modulus, [Pa] |
| K_1 | : Gas-saturated rock bulk modulus, [Pa] |
| K_s | : Matrix bulk modulus, [Pa] |
| K_{dry} | : Dry rock bulk modulus, [Pa] |
| K_g | : Gas bulk modulus, [Pa] |
| K_l | : Liquid bulk modulus, [Pa] |
| K_{eff} | : Effective bulk modulus, [Pa] |
| μ_{sat} | : Saturated rock shear modulus, [Pa] |

| | |
|--------------|---|
| μ_{dry} | : Dry rock shear modulus, [Pa] |
| V_p | : P-wave velocity, [m/s] |
| ρ | : Density, [kg/m ³] |
| V_s | : S-wave velocity, [m/s] |
| ρ_s | : Matrix density, [kg/m ³] |
| ρ_w | : Water density, [kg/m ³] |
| S_g | : Gas saturation, [fraction] |
| ρ_g | : Gas density, [kg/m ³] |
| S_{oil} | : Oil saturation, [fraction] |
| ρ_{oil} | : Oil density, [kg/m ³] |
| S_p | : P-wave slowness, [μs/ft] |
| S_s | : S-wave slowness, [μs/ft] |

ACRONYMS

| | |
|-----|---------------------------|
| WBM | : Water-base mud |
| OBM | : Oil-base mud |
| CMG | : Computer Modeling Group |

REFERENCES

- [1] Abdollah Pour, R., 2008, Equation-of-state compositional, one-dimensional radial flow method to simulate invasion and fluid withdrawal in the presence of oil- or water-base muds: M.S. thesis, The University of Texas at Austin, pp. 75-77.
- [2] Berryman, J. G., 1999, Tutorial: Origin of Gassmann's equations: *Geophysics*, v. 64, no. 5, pp. 1627-1629.
- [3] Biot, M. A., 1956, Theory of propagation of elastic waves in a fluid-saturated porous solid I. Low-frequency range: *Journal of Acoustical Society of America*, v. 28, no. 3, pp. 168-178.
- [4] Chi, S., Torres-Verdín, C., Wu, J., and Alpak, F. O., 2006, Assessment of mud-filtrate invasion effects on borehole acoustic logs and radial profiling of formation elastic properties: *SPE Reservoir Evaluation and Engineering*, v. 9, no. 5, pp. 553-564.
- [5] Contreras, A., Torres-Verdin, C., and Fasnacht, T., 2007, Sensitivity analysis of data-related factors controlling AVA simultaneous inversion of partially stacked seismic amplitude data: Application to deepwater hydrocarbon reservoirs in the central Gulf of Mexico: *Geophysics*, v. 72, no. 1, pp. C19-C29.
- [6] Contreras, A., Torres-Verdín, C., Kvien, K., Chesters, W., and Fasnacht, T., 2005, Joint stochastic inversion of 3D pre-stack seismic data and well logs for high-resolution reservoir characterization and petrophysical modeling: application to deepwater hydrocarbon reservoirs in the central Gulf of Mexico: 56th Annual International Meeting, SEG, Expanded Abstracts, Houston, TX, November 6-11.
- [7] Domenico, S. N., 1976, Effect of brine-gas mixture on velocity in an unconsolidated sand reservoir: *Geophysics*, v. 41, no. 5, pp. 882-894.
- [8] Franco, J.L., Ortiz, M.A., De, G.D., Renlie, L. and Williams, S., 2006, Sonic investigations in and around the borehole: *Schlumberger Oilfield Review*, v. 18, no. 1, pp. 14-33.
- [9] Geertsma, J. and Smit, D. C., 1961, Some aspects of elastic wave propagation in fluid-saturated porous solids: *Geophysics*, v. 26, no. 2, pp. 169-181.
- [10] Hadorson, J. B.U., Johnson, D. L., Plona, T., Sinha, B., Valero, H. and Winkler, K., 2006, Borehole acoustic waves: *Schlumberger Oilfield Review*, v. 18, no. 1, pp. 34-43.
- [11] Kimball, C.V. and Marzetta, T.L., 1984, Semblance processing of borehole acoustic array data: *Geophysics*, v. 49, no. 3, pp. 274-281.

[12] Knight, R., Dvorkin, J. and Nur, A., 1998, Acoustic signatures of partial saturation: *Geophysics*, v. 63, no. 1, pp. 132-138.

[13] Ma, J. and Torres-Verdín, C., 2007, 3D numerical simulation of borehole sonic measurements acquired in dipping, anisotropic, and invaded formations: 5th Annual Formation Evaluation Consortium, Expanded abstracts, Austin, Texas, August 15-17.

[14] Malik, M., Salazar, J. M., Torres-Verdín, C., Wang, G. L., Lee, H. J., and Sepehrnoori, K., 2007, Influence of petrophysical and fluid properties on array-induction measurements acquired in the presence of oil-base mud-filtrate invasion: 48th Annual Logging Symposium, Society of Petrophysicists and Well Log Analysts (SPWLA), Expanded Abstracts, Austin, Texas, June 3-6.

[15] Mavko, G., Mukerji, T. and J. Dvorkin, 2003, *The rock physics handbook tools for seismic analysis in porous media*: Cambridge University Press.

[16] Odumosu, T., Torres-Verdín, C., Salazar, J. M., Ma, J., Boss, V., and Wang, G. L., 2009, Estimation of dry-rock elastic moduli based on the simulation of mud-filtrate invasion effects on borehole acoustic logs: in press, *SPE Reservoir Evaluation and Engineering*.

[17] Peyret, A., and Torres-Verdín, C., 2006, Assessment of shoulder-bed, invasion, and lamination effects on borehole sonic logs: a numerical sensitivity study: 47th Annual Logging Symposium, Society of Petrophysicists and Well Log Analysts (SPWLA), Expanded Abstracts, Veracruz, Mexico, June 4-7.

[18] Pistre, V., Kinoshita, T., Endo, T., Schilling, K., Pabon, J., Sinha, B., Plona, T., Ikegami, T. and Johnson, D., 2005, A modular wireline sonic tool for measurement of 3D (azimuthal, radial, and axial) formation acoustic properties: transaction presented at the 2005 SPWLA Annual Logging Symposium, New Orleans, Louisiana, 26-29 June.

[19] Salazar, J. M., Torres-Verdín, C., Alpak, F. O., Habashy, T. M., and Klein, J. D., 2006, Estimation of permeability from array induction measurements: applications to the petrophysical assessment of tight-gas sands. *Petrophysics*, v. 47, no. 6, Dec 2006; p.p. 527-544

[20] Smith, T.M., Sondergeld, C.S. and Rai, C.H., 2003, Gassmann fluid substitutions: a tutorial: *Geophysics*, v. 68, no. 2, pp. 430-440.

[21] Tang, X.M. and A. Cheng, 2004, *Quantitative borehole acoustic methods*: Elsevier.

[22] Wang, G. L., Torres-Verdín, C., and Odumosu, T., 2007, Combined inversion of borehole resistivity and sonic measurements to estimate water saturation, porosity, and dry-rock elastic moduli in the presence of invasion: 48th Annual Logging Symposium,

Society of Petrophysicists and Well Log Analysts (SPWLA), Expanded Abstracts, Austin, Texas, June 3-6.

[23] Wu, J., Torres-Verdín, C., Sepehrnoori, K., and Proett, M., 2005, The influence of water-base mud properties and petrophysical parameters on mudcake growth, filtrate invasion, and formation pressure: *Petrophysics*, v. 46, no. 1, 14-32.